

Aerodynamic Study of a Small, Ducted VTOL Aerial Vehicle

by

Kyrilian Dyer

S.B. Mechanical Engineering, MIT 2000

Submitted to the Department of Aeronautics and Astronautics in Partial Fulfillment of the
Requirements for the Degree of MASTER OF SCIENCE in

AERONAUTICS & ASTRONAUTICS

at the

MASSACHUSETTS INSTITUTE OF TECHNOLOGY

June 2002

© 2002 Kyrilian Dyer. All rights reserved.

The author hereby grants to MIT permission to reproduce and distribute publicly paper
and electronic copies of this thesis document in whole or in part.

Signature of Author: _____

Department of Aeronautics & Astronautics

May 2002

Certified by: _____

Sean George

Charles Stark Draper Laboratory

Thesis Supervisor

Certified by: _____

Professor John Deyst

Professor of Aeronautics & Astronautics

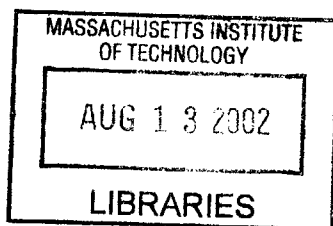
Thesis Advisor

Accepted by: _____

Wallace E. Vander Velde

Professor of Aeronautics and Astronautics

Chair, Committee on Graduate Students



AERO

[THIS PAGE INTENTIONALLY LEFT BLANK]

Aerodynamic Study of a Small, Ducted VTOL Aerial Vehicle

by

Kyrilian G. Dyer

Submitted to the Department of Aeronautics and Astronautics on May 10, 2002 in partial fulfillment of the requirements for the Degree of Master of Science in Aeronautics and Astronautics.

Abstract

The Perching Unmanned Aerial Vehicle (PUAV) is a 9-inch diameter ducted vertical takeoff and landing reconnaissance vehicle with the capability of fast-forward cruise flight. Currently in the development stage, the program is envisaged to yield a man-portable craft that a foot soldier can use to provide over-the-hill observation. Several prototypes have been constructed and tested, with mixed results. Concerns regarding duct aerodynamics led to the proposal for further aerodynamic study to investigate effects of inlet lip radius and surface area, diffuser area ratio, blade tip clearance and rotor position on thrust, power and efficiency. This report covers the theory of rotorcraft and ducted propeller aerodynamics, and outlines the tests performed and results obtained. It also presents specifications of the test vehicle and methods that can be used in future ducted aircraft studies.

Large angle diffusers tested showed reduced thrust and efficiency and increased power compared to smaller diffusers, contrary to theory. Reverse flow within the core appears to disrupt uniform exit flow and yields a conically divergent turbulent wake. Results of this study will be used in the redesign of a duct core fairing, which will act to control the airflow and reduce the tendency for reverse flow at the center where blade thrust is absent. Future studies will also consider twisted, cambered and tapered rotor blades in an effort to better address spanwise thrust distribution and optimized airflow.

The test apparatus and methods developed for this report, in addition to results of initial testing, will be instrumental to further development of small ducted UAVs. Findings and methods are not limited to exact duplicates of PUAV-like aircraft, but can be used in a wide range of applications including lift and thrust-producing ducts.

Technical Supervisor: Mr. Sean George
Title: Charles Stark Draper Laboratory

Thesis Advisor: Professor John Deyst
Title: Professor, Aeronautics and Astronautics

Acknowledgments

June, 2002

This thesis was prepared at The Charles Stark Draper Laboratory, Inc., under Internal Company Sponsored Research Project 3019, Navigating Under the Canopy.

Publication of this thesis does not constitute approval by Draper of the findings or conclusions contained herein. It is published for the exchange and stimulation of ideas.



(Author's signature)

I would like to thank all those who have made this fun little project move forward. I am grateful to Sean George for devoting his time and wisdom to this project. Thanks to Jamie Anderson for giving me direction and to John Plump and Neil Gupta for conceiving the project and giving it life. I have enjoyed the friendship and enthusiasm of Neil and Paul Eremenko. Thanks also to Tim Barrows and Professor John Deyst for their input and wisdom. Without the help of Kailas Narendran and Dave Weagle, I wouldn't have had the hardware to go forward. I've enjoyed sharing a relaxed and friendly office, thanks to Dave, Kara, Carissa, Jeb and Matt. Of course, thanks to all my friends for their support and understanding. Finally, thank you Mom and Dad, for your quiet encouragement and gentle guidance.

Table of Contents

Chapter 1: Introduction.....	9
Chapter 2: Background and History	13
2.1 Design Requirements	13
2.2 Survey of Similar Aircraft.....	15
2.2.1 History of Vertical Takeoff Aircraft	15
2.2.2 Current Vertical Takeoff UAVs.....	16
2.3 PUAUV Development Evolution.....	20
2.3.1 Preliminary Design	22
2.3.2 Alpha Prototype Design	23
2.3.3 Beta Prototype Design	27
Chapter 3: Theoretical Performance	31
3.1 Rotorcraft Aerodynamics	31
3.1.1 Momentum Theory	31
3.1.2 Blade Element Theory	39
3.1.3 Coaxial Momentum Theory	44
3.1.4 Ducted Rotor Performance.....	46
3.2 Other Inlet and Diffuser Effects	49
3.2.1 Inlet Thrust Augmentation	50
3.2.2 Inlet Losses	54
3.2.3 Duct and Diffuser Losses.....	57
3.3 PUAUV Numerical Model.....	57
Chapter 4: Experimental Test Apparatus.....	61
4.1 Drive Train	61
4.1.1 Driveline	61
4.1.2 Test Motor.....	67
4.2 Duct Construction	69
4.2.1 Inlets.....	71
4.2.2 Exit Diffusers	73
4.3 Data Acquisition.....	75
4.3.1 Hardware	75
4.3.2 Data Acquisition Software	78

Chapter 5: Data Collection and Analysis	81
5.1 Test Matrix Design.....	81
5.2 Calibration.....	83
5.2.1 Motor Calibration.....	83
5.2.2 Servo Calibration	86
5.2.3 Differential Collective.....	87
5.3 Experimental Results.....	90
5.3.1 Inlet Size	90
5.3.2 Diffuser Angle.....	92
5.3.3 Number of Rotors.....	95
5.3.4 Blade Tip clearance.....	97
5.3.5 Ground Effect.....	98
5.3.6 Wake Survey	99
5.4 Results Analysis and Model Comparison	105
5.4.1 Inlet Size	105
5.4.2 Diffusion Ratio.....	111
Chapter 6: Conclusion	117
References	119
Appendix A: Motor Specifications	121

List of Figures

Figure 1.1 The PUAV Alpha II prototype.	10
Figure 1.2 Takeoff (a) and landing (b) of the PUAV.	10
Figure 2.1 MAV deployment from “parent” vehicle system (Gupta [4])......	14
Figure 2.2 Sikorsky Cypher.	17
Figure 2.3 Allied Aerospace Industries iSTAR (LADF) (a) without and (b) with wings.	19
Figure 2.4 Preliminary PUAV design architecture (from Gupta [4]).	22
Figure 2.5 Alpha I prototype.....	24
Figure 2.6 Alpha I prototype thrust test apparatus (from Gupta [4])......	25
Figure 2.7 Alpha II prototype, with redesigned forebody.....	26
Figure 2.8 Alpha II thrust test apparatus.....	27
Figure 2.9 Beta prototype.	28

Figure 3.1 Helicopter rotor control volume.	32
Figure 3.2 Theoretical PUAU figure of merit for different diffusion ratios.	38
Figure 3.3 Inflow and force components of a blade element. From above (a) and spanwise (b).	40
Figure 3.4 Ducted rotor with diffuser exit.	47
Figure 3.5 Streamlines (a), and pressure distribution (b) over the inlet.	50
Figure 3.6 Inlet surface area geometry.	52
Figure 3.7 Vena contracta.	55
Figure 3.8 Thrust losses due to sharp inlet curvature.	56
Figure 3.9 Computational Flowchart.	59
Figure 4.1 Schematic diagram of PUAU hover test vehicle drive train.	62
Figure 4.2 PUAU hover test vehicle drive train.	63
Figure 4.3 NHP Tail rotor blade sectional lift and drag coefficient.	64
Figure 4.4 Rotor collective control diagram.	66
Figure 4.5 RPM vs. torque available and required.	68
Figure 4.6 Duct/drive train interface.	71
Figure 4.7 Section diagrams of four test inlets.	73
Figure 4.8 Diagram of three test diffusers.	74
Figure 4.9 Construction of a diffuser.	75
Figure 4.10 PUAU hover thrust test apparatus.	76
Figure 4.11 Mechanical (a), and electrical (b) test apparatus layout.	77
Figure 5.1 Motor test stand and Prony brake.	84
Figure 5.2 Servo calibration curves.	87
Figure 5.3 Differential Collective calibration test results.	89
Figure 5.4 Thrust as a function of blade angle for three inlet sizes (medium diffuser, $\sigma_{duct} = 1.37$)	90
Figure 5.5 Power as a function of blade angle for three inlet sizes (medium diffuser, $\sigma_{duct} = 1.37$)	91
Figure 5.6 Power coefficient divided by thrust coefficient as a function of thrust coefficient for three inlet sizes (medium diffuser, $\sigma_{duct} = 1.37$).	92
Figure 5.7 Thrust as a function of blade angle for three diffusers (large inlet, $r_i = 25.4\text{mm}$).	93
Figure 5.8 Power as a function of blade angle for three diffusers (large inlet, $r_i = 25.4\text{mm}$).	93
Figure 5.9 Power coefficient divided by thrust coefficient as a function of thrust coefficient for three diffusers (large inlet, $r_i = 25.4\text{mm}$).	94
Figure 5.10 Thrust coefficient as a function of blade angle for each individual rotor and both rotors (large inlet, medium diffuser).	96

Figure 5.11 Power coefficient as a function of blade angle for each individual rotor and both rotors (large inlet, medium diffuser).....	97
Figure 5.12 Power coefficient as a function of thrust coefficient for a 0.5 and 1 mm blade tip gap (large inlet, medium diffuser).....	98
Figure 5.13 C_P/C_T as a function of height.....	99
Figure 5.14 Wake flow for (a) small diffuser ($\sigma_{duct} = 1.0$), (b) medium diffuser ($\sigma_{duct} = 1.37$), and (c) large diffuser ($\sigma_{duct} = 1.65$) with single rotor at 3000 RPM.	100
Figure 5.15 Wake survey comparison of single rotor with cone-shaped fairing and dual rotor without a fairing.	101
Figure 5.16 Thrust coefficient as a function of rotor RPM with and without a cone-shaped fairing (single rotor, 35° fixed).	102
Figure 5.17 Power coefficient as a function of thrust coefficient with and without a cone-shaped fairing (single rotor, 35° fixed).....	103
Figure 5.18 Swirl angle for single (upstream) and dual rotor condition.....	104
Figure 5.19 Thrust coefficient, C_T as a function of blade angle, θ for three inlet sizes (2400 RPM).	106
Figure 5.20 Power coefficient, C_P as a function of blade angle, θ for three inlet sizes (2400 RPM).	107
Figure 5.21 Thrust coefficient, C_T as a function of inlet size, r_i (2400 RPM).	108
Figure 5.22 C_P/C_T as a function of thrust coefficient, C_T for three inlet sizes (2400 RPM).	109
Figure 5.23 Thrust coefficient, C_T as a function of blade angle, θ for flanged and unflanged medium inlets (25 mm flange, 1800 RPM).	110
Figure 5.24 Thrust coefficient, C_T as a function of blade angle, θ for three diffuser ratios (2400 RPM).	111
Figure 5.25 Thrust coefficient, C_T as a function of diffusion ratio (2400 RPM).	112
Figure 5.26 Power coefficient, C_P as a function of blade angle, θ for three diffuser ratios (2400 RPM).	113
Figure 5.27 C_P/C_T as a function of thrust coefficient, C_T for three diffuser ratios (2400 RPM).	114
Figure 5.28 C_P/C_T as a function of diffusion ratio at 2400 RPM.	114

List of Tables

Table 2.1 UAV aircraft type comparison.....	20
Table 4.1 Diffuser dimensions (see Figure 4.8).....	74
Table 5.1 Test matrix.....	82
Table 5.2 Motor and driveline data.....	86
Table 5.3 Differential collective calibration test.....	88
Table A-1: Inertial Motors Specifications.	121

Chapter 1: Introduction

Many civil and military uses exist for a man-portable aerial reconnaissance vehicle capable of vertical takeoff, high-speed horizontal flight, hover and vertical landing. The Perching Unmanned Aerial Vehicle (PUAV), developed at the Charles Stark Draper Laboratory was designed to meet these requirements while remaining small and light enough to be carried in a backpack for close tactical surveillance support.

A ducted propeller design was chosen to allow a very small footprint while minimizing the danger to users of the aircraft. It was believed that traditional ducted aircraft designs are lacking in their ability to transition to high-speed forward flight. This is usually accomplished by the aircraft slowly pitching forward such that the initially vertical axis approaches horizontal in the forward direction of flight. Aircraft stall and loss of control authority has been a historical problem with this type of transition. A unique double flight mode was conceived for the PUAV in which the vehicle would climb vertically to altitude, and then pull out of a dive in the opposite flow direction (see Figure 1.2 (a)). Landing would be accomplished by reversing the direction of thrust and rotating the vehicle toward the ground (see Figure 1.2 (b)). In this manner, both take-off and landing would use gravity to control vehicle speed, while minimizing the angle of attack of the vehicle and reducing the opportunity for stalled flight. The bi-directional flow required

for such flight necessitated careful aerodynamic design of the duct, in addition to the need for the rotor system to reverse the direction of thrust on command.

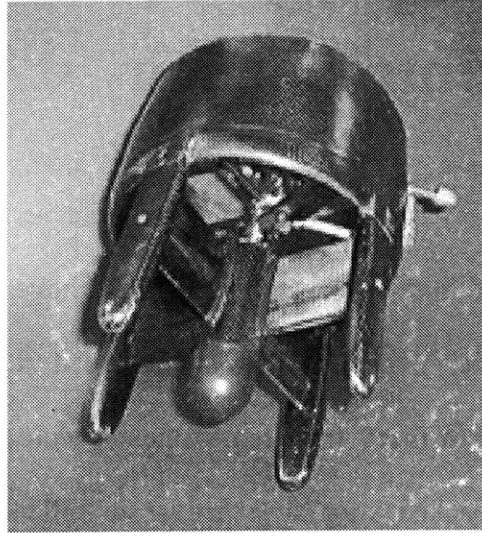


Figure 1.1 The PUAV Alpha II prototype.

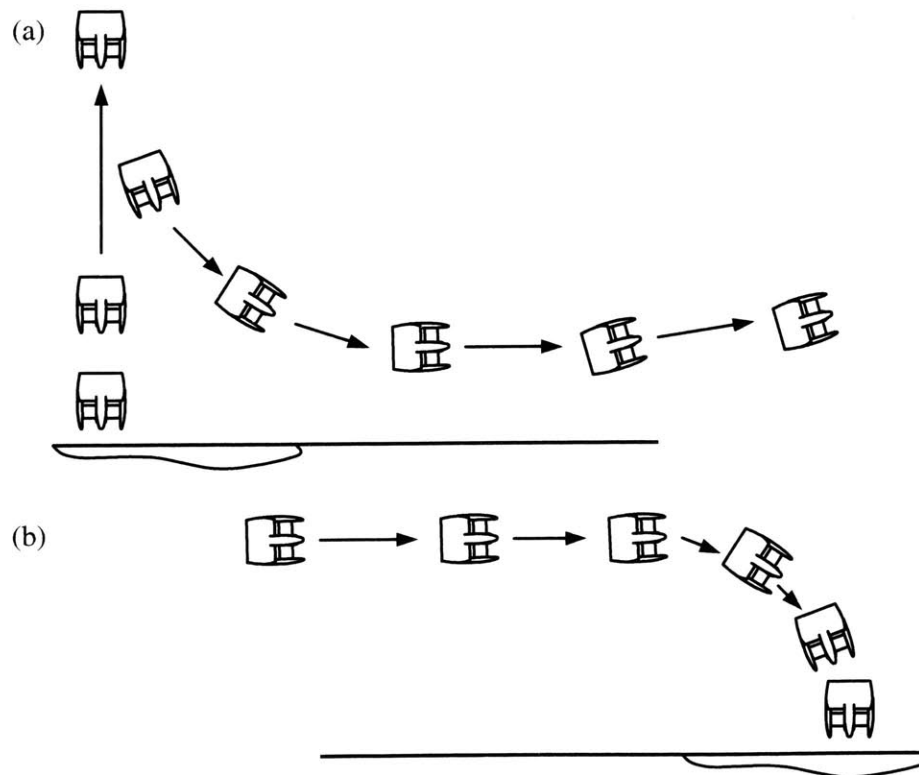


Figure 1.2 Takeoff (a) and landing (b) of the PUAV.

The PUAUV was designed in a short time span with minimal expense. The brief timeframe limited the depth of aerodynamic design possible. Following construction of a prototype, initial tests showed that performance was worse than expected, believed due in part to disturbed airflow over the duct. In the hover mode, air entered the duct past a small radius inlet lip, which acted as the annular airfoil trailing edge in forward flight. The leading edge of the annular airfoil then acted as the hover duct exit. Powered tests while observing wool tufts disturbed by the turbulent airflow were inconclusive in determination of separation, but it was believed that thrust was being lost to stall at the inlet, disturbed flow entering the rotor disk, and further separation at the radiused exit. A review of the design was proposed, which would create a numerical aerodynamic model of the duct and rotors to be used in a redesigned vehicle. Aerodynamic testing would then be performed to verify the model before implementation.

The primary focus of the work presented herein is to model the airflow of a small ducted aircraft and substantiate the numerical model with experimental results. Chapter 2 highlights the history and current state of vertical takeoff UAVs, and then describes the background of the PUAUV project. The third chapter covers the theory behind helicopter and ducted vehicle flight, with specific coverage of diffused and contrarotating coaxial ducted aerodynamics. The test vehicle constructed for these tests, described in Chapter 4, allows the introduction of several inlet mouths and exit diffusers and can be run for indefinite lengths of time using a tethered electric motor. The test article is not limited to the bi-directional architecture of the PUAUV, but is based on a similar sized vehicle.

The PUAUV project has been successful in producing useful design lessons, as well as yielding hover test results that can be used in the redesign of the PUAUV airframe. The results and test methods may be extended to other ducted thrust and lift producing applications at the Draper Laboratory as well, including forward velocity wind tunnel tests.

The significant results of this program are listed below:

- ***Ducted propeller test vehicle***
 - *Engine driven drive train for 1 or 2 rotors*
 - *Electric motor driven drive train for 1 or 2 rotors*
 - *Servo driven variable pitch mechanism for 1 or 2 rotors*
 - *Reconfigurable duct inlets*
 - *Reconfigurable diffuser section*
- ***Data collection apparatus***
 - *LabView based data acquisition*
 - *Integration of load cell, RPM, current and voltage sensors, and servo position*
 - *Development of pitot-tube based wake surveys*
- ***Ducted rotor hover test data***
 - *Range of tested variables (duct geometry, collective, RPM, # of rotors)*
- ***Numerical ducted rotor model***
 - *Matlab based simulation tool*
 - *Validation tests performed on test data*

Chapter 2: Background and History

2.1 Design Requirements

The evolution of battle has brought about a widespread use of strategic and medium to large scale tactical surveillance platforms, ranging from space-born satellite assets and large, high-altitude reconnaissance airplanes like the RQ-4A Global Hawk, to smaller fixed wing tactical vehicles such as the RQ-1A Predator. At the beginning of the twenty-first century the utilization of Vertical Takeoff and Landing (VTOL) Unmanned Aerial Vehicles (UAVs) and Micro Aerial Vehicles (MAVs) is still quite immature.

Although there exist many manned and unmanned theatre-wide surveillance platforms and medium range tactical support aircraft, there is a need to provide real-time close support surveillance capability to the foot soldier, who must fight in an increasingly complex battlefield. Such a vehicle could peer through windows, around corners, and over hills to provide the soldier with an enhanced level of situational awareness, with much reduced risk of injury or death. Visual sensors could provide information on terrain outlay, hostile troop and civilian movements, as well as hidden weapons that may not be detectable from longer range or directly above, and therefore beyond the capability of most long-range surveillance platforms.

To be effective, such a vehicle would have to be small and maneuverable, while remaining simple to use and easy to carry. Its small size would reduce detection, as well as make it feasible for backpack carriage or deployment from another larger, longer-range “parent” aircraft (see Figure 2.1). Size and maneuverability, including the ability to hover, would also provide it with the unique ability to fly through forested areas and between buildings.

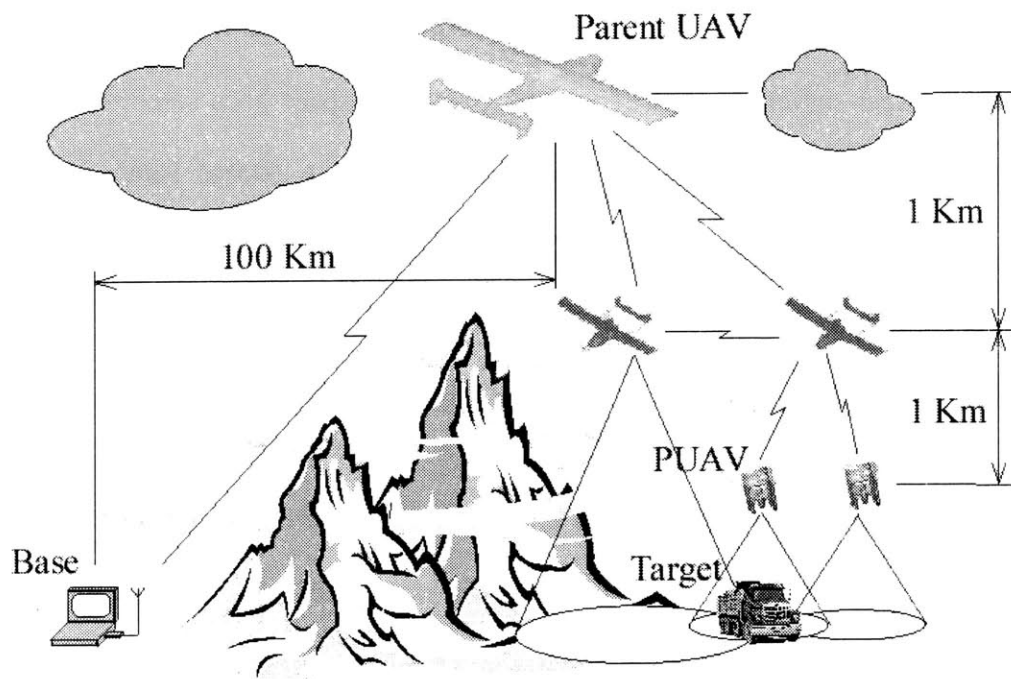


Figure 2.1 MAV deployment from “parent” vehicle system (Gupta [4]).

Based on perceived interest of the US Defense Department, the Charles Stark Draper Laboratory set the following requirements at the onset of this program:

- *No larger than 10 inches (maximum linear dimension)*
- *Video downlink capable*
- *VTOL flight capable*
- *Capable of 20-minute flight duration*
- *Capable of hovering in winds of at least 5 mph*
- *Capable of transitioning to high speed (40+ mph) forward flight*

The Perching UAV (PUAV) was designed to fulfill most of these requirements. Its dimensional constraints were partially waived for a first iteration, with the intention that future designs evolve into a smaller aircraft. The diameter fell within the constraints but the height exceeded the limits by several inches.

2.2 Survey of Similar Aircraft

2.2.1 History of Vertical Takeoff Aircraft

As with helicopters, the melding of vertical takeoff and high speed forward flight capabilities in unmanned vehicles has been the bane of UAV designers. The history of small vertical takeoff aerial vehicles is broad and varied, and filled with many failed attempts at an economical, high performance vehicle.

The origins of unmanned aerial vehicles harken back to the late nineteenth century, when Douglas Archibald used a kite to carry aloft a camera with which to take reconnaissance photographs. During the Great War, Charles Kettering developed a biplane aerial torpedo that contained a rudimentary control system, making it the first guided cruise

missile. Many other designs have followed, mostly driven by the need for military reconnaissance, munitions delivery and targeting.

On the fourteenth of September 1939, Igor Sikorsky brought the helicopter into being with the first flight of his VS-300. Powered by a Franklin 75hp engine driving a three-bladed rotor, this open-frame, single seat helicopter was soon developed into the VS-316A. The VS-316A, with military designation XR-4 and YR-4A, had an enclosed two-place cabin, a slightly larger rotor, and was powered by a more powerful 175hp engine. Four years after the flight of his first helicopter, Sikorsky's VS-316A went into production. Today helicopters are used in myriad manned and unmanned operations that would otherwise be difficult or impossible.

The first vertical takeoff and landing (VTOL) UAV to become operational was the Gyrodyne QH-50 DASH (Drone Anti-Submarine Helicopter), introduced by the Navy in 1963. These UAVs provided standoff capabilities to ships by delivering torpedoes to targets far from the fleet. Since that time many VTOL UAVs, mostly helicopters, have been put to use around the world in civilian and military operations.

2.2.2 Current Vertical Takeoff UAVs

The military use of vertical takeoff UAVs has been most noticeable in the maritime arena, where small ship decks preclude the normal operation of airplanes. While the US Navy operates fixed-wing aircraft like the RQ-2A Pioneer from the decks of ships, the rocket assisted launch and net-capture recovery of such vehicles is difficult and dangerous.

After disappointment in the results of the Tactical UAV (TUAV) competition, a fixed-wing UAV program that sought to focus Army, Navy and Marine UAV needs, the Navy and Marine Corps decided to develop their own VTOL UAV program. The early 1990s saw several programs, including the joint US-Canada Maritime VTOL UAV System (MAVUS), the domestic Tilt-Rotor UAV System (TRUS), and the Vertical Launch And Recovery (VLAR) program. In 1997 the VTOL Demonstrator program was initiated to determine the state of maritime VTOL UAV capability. The Bell Eagle Eye tilt rotor, SAIC Vigilante helicopter, and Bombardier (formerly Canadair) CL-327 Guardian contrarotating coaxial rotor helicopter competed while several other platforms including the Sikorsky Cypher (Figure 2.2), failed to receive bids.

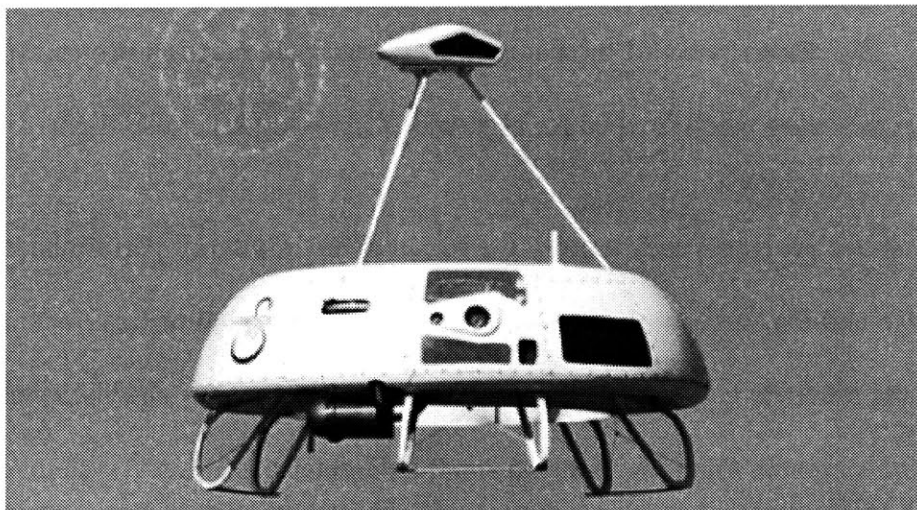


Figure 2.2 Sikorsky Cypher.

In 1999 the Navy issued a request for proposals (RFP) for the Vertical Takeoff Tactical UAV (VTUAV). The competition required that the vehicle cruise at 135 knots to a range of at least 110 nautical miles (nm), have an endurance of at least 3 hours, and carry a minimum 200 lb payload. Many of the VTOL Demonstrator entrants submitted proposals, including SAIC, Bombardier, Bell, Sikorsky with its Mariner, a modified

version of Cypher with wings, and Northrop Grumman with the Model 379 Fire Scout. The Fire Scout, a modified version of the Schweizer 333 four-place manned turbine helicopter, won the competition. It has since received go-ahead for Low-Rate Initial Production (LRIP).

The Defense Advanced Research Projects Agency (DARPA) currently has two development and flight demonstration contracts under the Advanced Air Vehicle (AAV) program. One, the Frontier Systems A160 Hummingbird seeks to achieve high (48 hour) endurance and long (2000 nm) range through the use of a variable speed rotor system, allowing optimal cruise efficiency. The Boeing Dragonfly Canard Rotor/Wing (CRW) stop rotor aircraft also hopes to achieve airplane-like range and vertical takeoff capability. The design is based on a stoppable warm-cycle reaction-driven rotor system that can act as a wing when stopped for high-speed (350-400 kt) cruise flight.

While the above programs seek to raise the bar in terms of aircraft performance, they are far too large and expensive to be used for over-the-hill personal tactical reconnaissance. Although the Sikorsky Cypher may fulfill some requirements, it is still incompatible with most *packable* combat missions. Several small helicopter-based UAV systems have been developed around the world including the Austrian Schiebel Camcopter, the French Survey-Copter and Techno Sud Vigilant, and the US Aerocam. Many of these designs are used for filming and other civilian tasks, and have not been designed for the rigors of field combat use.

Ducted VTOL platforms have also made some headway. The standing piloted Hummingbird VTOL observation platform has been converted to the unmanned Hornet

by the Israeli company AD&D. Powered by four 22 horsepower engines turning two contrarotating 3-bladed rotors within a 2.2 m duct, it can carry a payload of 115 kg. Smaller vehicles include the aforementioned Cypher, which has a thick donut-shaped duct with external dimensions similar to the Hornet. Its payload and gross weight are approximately half as great as the Hornet, however.

Much smaller ducted VTOL aircraft are the Moller AROD and Aerobot, and the iSTAR under development at the San Diego-based Flight Systems Division of Allied Aerospace Industries, Inc. The development of this vehicle is currently being funded under the DARPA Organic Air Vehicle (OAV) program. These designs all utilize ducted fixed propellers and movable control stators in the rotor wake.

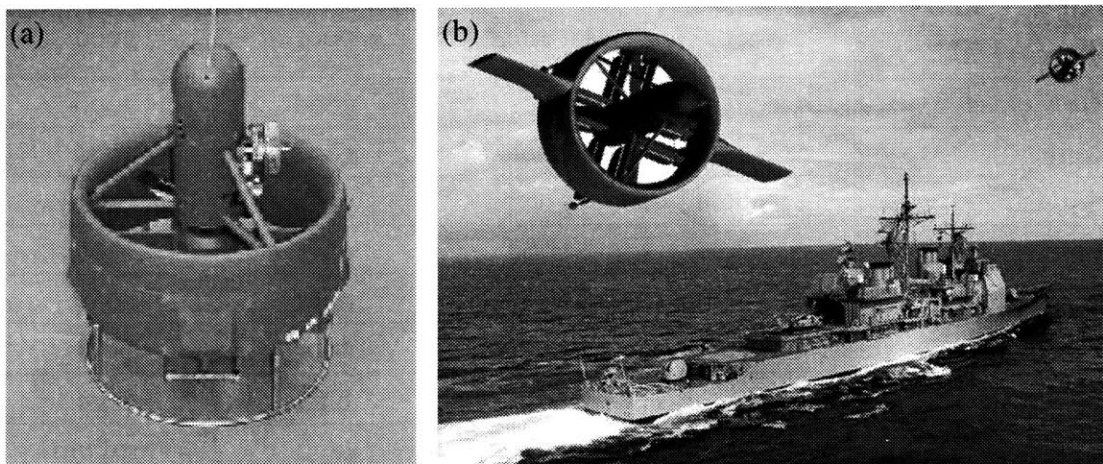


Figure 2.3 Allied Aerospace Industries iSTAR (LADF) (a) without and (b) with wings.

It is clear from the number of recently funded programs in these areas, that substantial development will be required before a fieldable system is built. The PUAUV project has sought to examine some of the basic questions involved with small VTOL operation and performance in hopes of highlighting some important design concepts. The vehicle

design differs from other concepts in its use of variable pitch contrarotating rotors. This project was focused on examining the performance benefits of this type of system over simpler and lighter, yet less efficient fixed pitch single rotor systems.

2.3 PUAU Development Evolution

Many variables must be considered in the design of a UAV with such broad flight envelope requirements as the PUAU. Table 2.1 illustrates the relative benefits of each aircraft platform.

Table 2.1 UAV aircraft type comparison.

	Airplane	Helicopter	Tilt rotor	Ducted UAV
<i>Hover flight</i>	poor	excellent	good	good
<i>Slow flight</i>	poor	excellent	good	good
<i>Low speed Maneuverability</i>	poor	excellent	poor	good
<i>High speed</i>	excellent	poor	good	good
<i>Range</i>	excellent	poor	good	good
<i>Payload</i>	excellent	good	poor	poor
<i>Ease of use</i>	excellent	good	poor	good
<i>Durability</i>	excellent	poor	poor	good
<i>Noise</i>	good	poor	poor	poor
<i>Cost</i>	low	medium	high	high
<i>Complexity</i>	low	medium	high	medium
<i>Maturity</i>	high	high	low	low

When the ability to hover, and takeoff and land in a confined area exists, and when high speed is unimportant, the helicopter proves superior. It can carry a reasonable payload, is not unreasonably complex or difficult to control, and the technology is quite mature. When high speed is needed and the hover abilities of a helicopter are not necessary, an airplane excels. Airplanes are generally unable to maneuver well at slow speeds,

however. This is especially true with small airplanes such as Micro Aerial Vehicles (MAVs) with wingspans of less than 15 cm, as their wing loading is often high, requiring higher velocities and therefore large turning radii. For most requirements however, either an airplane or a helicopter can provide the necessary flight profile.

If the need for hover and high-speed flight are combined, a hybrid design must be used. The tilt rotor combines the rotors of a helicopter and the wings of an airplane to provide both airplane speed and helicopter hover capability. Due to complexity and the small size of the wings and rotors, neither mode performs as well as a comparable airplane or helicopter, respectively, though. Ducted vehicles like the iSTAR and PUAUV also use a combination of a rotor and wing, though in this case the wing is shaped as a ring surrounding the rotors, enhancing thrust and providing lift during cruise flight. Some ducted vehicles do not rotate to transition to forward flight, simply flying edgewise like a helicopter. The Sikorsky Cypher flies in this manner, with its winged sister aircraft, the Cypher II and Mariner designed to yield enhanced cruise performance.

Although other designs, including stoppable rotor helicopters, like the Boeing Dragonfly that transition to airplane flight when airborne, are under development, the four aircraft types listed in Table 2.1 cover the gamut of aircraft types currently available for reconnaissance missions. Due to the requirement for small size, hover flight, fast forward cruise, and good maneuverability, a ducted VTOL UAV design was chosen for the PUAUV.

2.3.1 Preliminary Design

The initial design of the PUAUV sought to conform to the requirements set forth by the Draper Laboratory, including the ability to hover and cruise at high speed, and be no larger than 10 linear inches in any dimension. To remain simple, the vehicle conceived was to be lifted aloft and propelled in forward flight by a single variable pitch rotor mounted within an annular *ring* wing duct. This duct would serve as a lift device in horizontal flight and improve thrust performance of the rotor in hover flight, and would serve to protect the user from injury and the rotor from landing and handling damage.

Due to high power density requirements wrought by the size restrictions and performance requirements, a small internal combustion (IC) engine was chosen to power the vehicle, rather than a battery supplied electric motor. Because only a single rotor would be used, stator vanes would counteract the torque applied by the rotor to maintain position. Canard-like fins would provide lift and attitude control (see Figure 2.4).

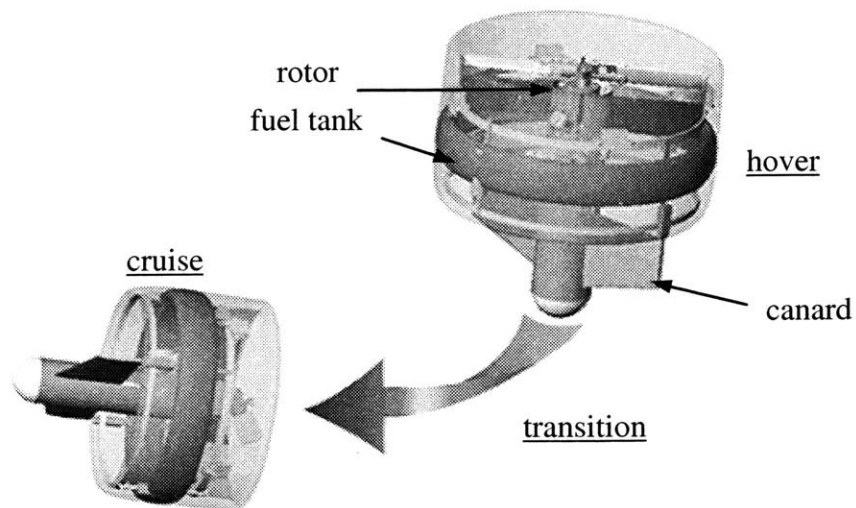


Figure 2.4 Preliminary PUAUV design architecture (from Gupta [4]).

Analysis of the control authority supplied by the canards indicated that they would provide insufficient pitch control. A redesign was thus begun that brought the canards further forward, where they could act about a greater moment arm. This became the Alpha prototype.

2.3.2 Alpha Prototype Design

Due to shortcomings in the initial design, a revised architecture was developed. Because too much stability reliance was being put on the anti-torque stator vanes, a coaxial design was conceived. This would allow the two rotors to turn in opposite directions, canceling the torques produced by each. By varying the collective blade pitch angles differentially between the rotors, a yaw torque in hover or roll torque in forward flight could be accomplished, reducing the load on control vanes and fins.

The need for high control authority brought the canard fins further away from the duct. For cruise flight this created the adverse affect of putting the aerodynamic center forward of the center of mass, creating instability in pitch. To alleviate pitch instability, the mass was moved further forward by extending the center fore body and installing four cylindrical pods that could act as mount points for the canards, accommodate the canard control mechanisms, and house the batteries required for the radio control receiver and servos. The stilt-like pods could also serve as landing gear for a hover landing.

Research references indicated an optimal rotor spacing of approximately 10 percent of the rotor diameter. Packaging constraints made placement of the engine critical and difficult. To fit the rotors and engine in the duct section left almost no room for the

gearbox that would have to reverse the direction of one of the rotors. With sufficient volume within the duct annulus to do so, a gearbox was placed in the duct. One drive shaft ran outward from the center-mounted engine to the gearbox, and another shaft ran between the rotors to a bifurcating gearbox that fed the rotors in opposite directions from one another. The external gearbox location also made engine starting easier.

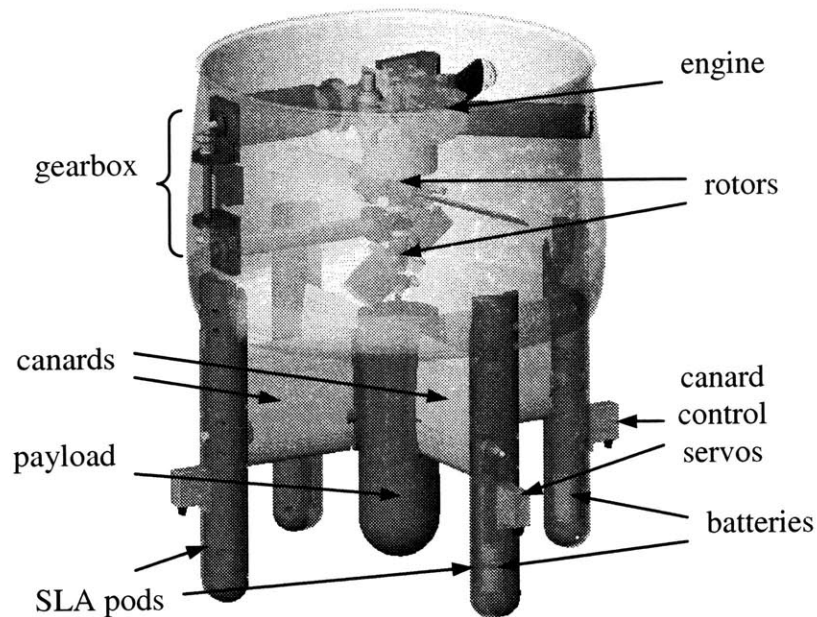


Figure 2.5 Alpha I prototype.

Due to testing difficulties of the IC engine, a tethered electric motor was substituted for initial tests. The vehicle was hung in its hover orientation from an overhead pulley arrangement as depicted in Figure 2.6. A line ran through a pair of pulleys where it was attached to a large weight, with a mass greater than the vehicle mass. This mass was placed on a tared scale, so that when the vehicle was not producing thrust the scale displayed a weight of zero. As thrust increased, the apparent weight increased, indicating the thrust of the vehicle. This test was only valid for thrust less than the vehicle weight.

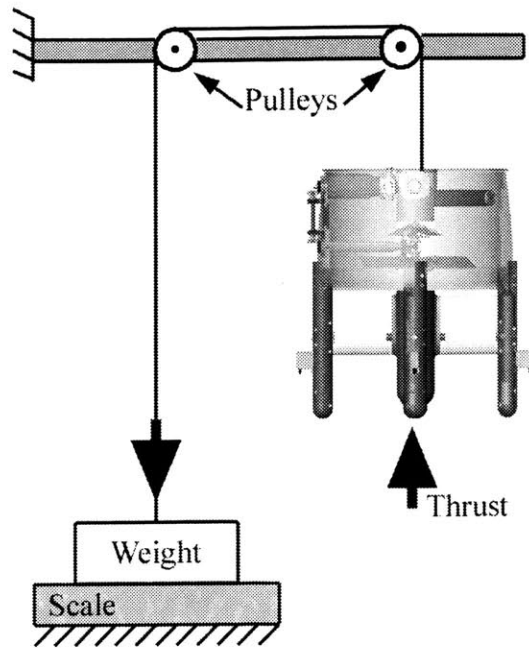


Figure 2.6 Alpha I prototype thrust test apparatus (from Gupta [4]).

The tests proved that the electric motor provided insufficient torque to drive the rotors at a high blade angle and at high speed. It was also clear that the weight of the vehicle was too great. Because the fore body components, including the main body and four pods, were made using the stereo lithographic apparatus (SLA) process, which creates a part out of heavy and brittle epoxy resin, they were chosen as the best components from which to pare weight.

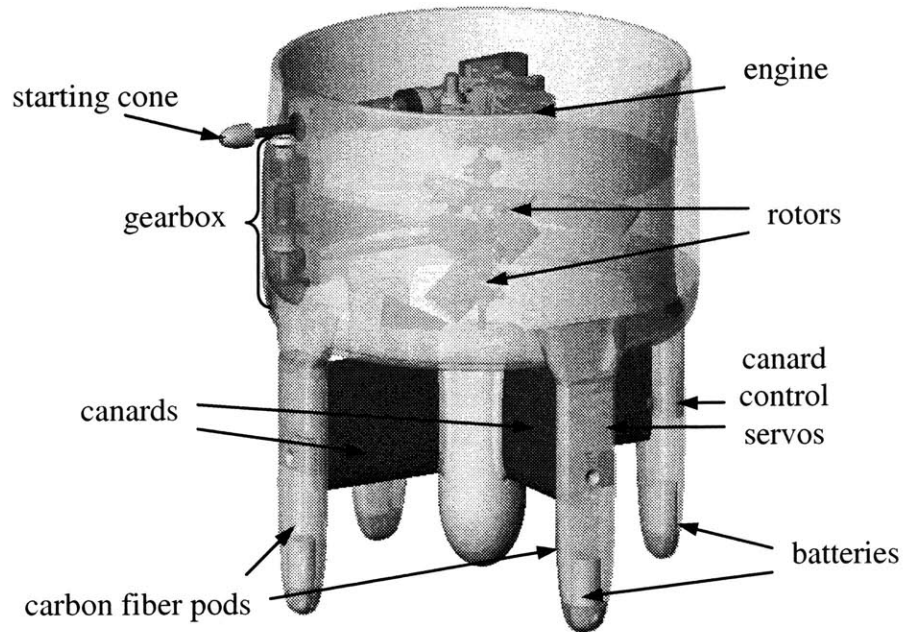


Figure 2.7 Alpha II prototype, with redesigned forebody.

The redesign, illustrated in Figure 2.7, incorporated the same general dimensions, though the shape of the pods and the construction of all the components were changed. The canard control servos were placed within the streamlined carbon fiber epoxy composite pods, reducing air drag and the chance of damage. The main body and canards were also made of carbon fiber composite. The weight of the entire structure was reduced from approximately 500 grams, about 40 percent of the overall vehicle weight, to less than 350 grams.

Once the fore body redesign was complete and the engine was reinstalled, tests were run. The thrust test apparatus comprised of a cantilevered beam mounted to a bearing, allowing free motion about the vertical axis. The vehicle was mounted to the end of the beam and a line and pulley system arranged to a tared weight atop a precision scale

provided a measurement of thrust (see Figure 2.8). Testing proved difficult, though largely to the recalcitrant engine.

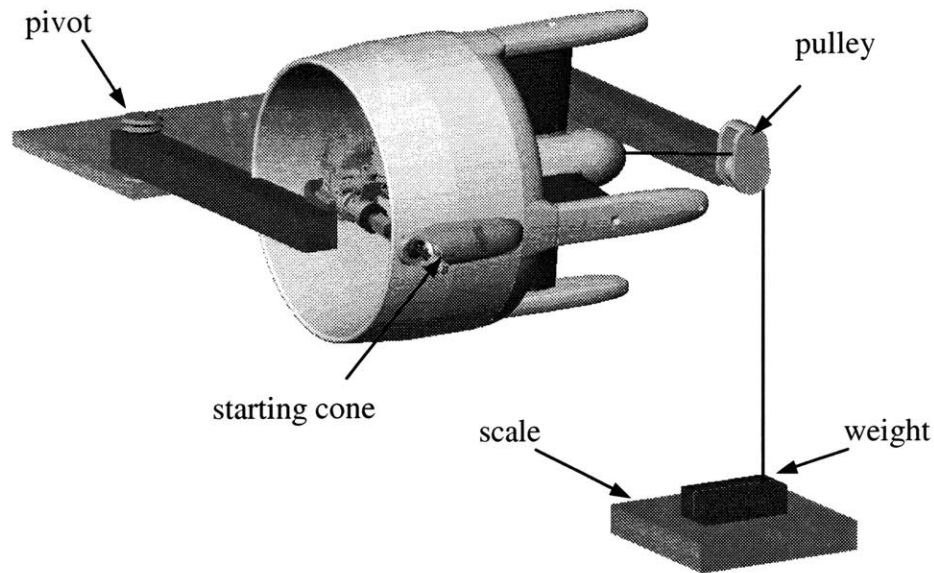


Figure 2.8 Alpha II thrust test apparatus.

2.3.3 Beta Prototype Design

Alpha II prototype thrust testing with the IC engine resulted in many failed components, as the torque produced by the engine overstressed the gear train components. The single cylinder 0.25 and 0.32 cubic inch displacement engines used for testing create very high periodic torques that vary in magnitude and direction through rotation. As the crankshaft turns, the drive train and flywheel must provide the torque to pull the piston through top dead center. Shortly thereafter the engine fires and drives the flywheel drive train with tremendous torque, reversing the drive train load. Brass gears were deformed and steel keyways were sheared due to these periodic loads. This effect was most predominant during starting and shutdown, when the relative speeds of the gear train and engine were disparate.

To alleviate some of the stresses incurred during shutdown, a one-way clutch was installed on the outer gearbox. This allowed the rotors to freewheel when the engine came to a brisk halt, eliminating stress that had previously sheared gear teeth and keyways. The small IC engines used for testing ran equally well in either direction however, and would often start backwards because no load was applied in the reverse direction of rotation.

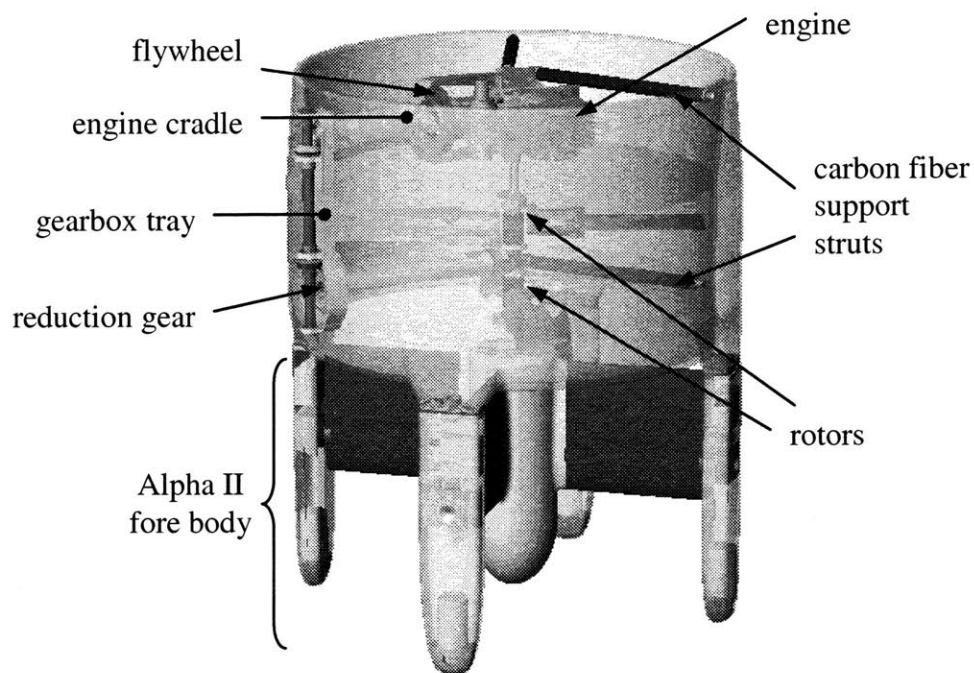


Figure 2.9 Beta prototype.

The redesigned gear train of the Beta prototype sought to address the starting and strength concerns. The parts count for the new design (Figure 2.9) was drastically reduced, and steel gears were substituted for brass gears. It became evident in testing that the engine was torque limited, and because sufficient thrust was believed possible at speeds of 6000-8000 RPM, half that of the engine's maximum power speed, a gear reduction was

deemed necessary. A gear reduction was designed into the outer gearbox tray, allowing engine to rotor gear ratios of 1:1 or 2:1.

The Beta prototype retained all other structural components of the Alpha II prototype. Unlike the previous designs, the Beta drive train did not include an extension of the engine shaft protruding from the duct. Starting was to be accomplished through the use of a rubber puck-like disk pushed against the small flywheel of the drive train. This method proved unfeasible. The standard OS .32 SX-H engine was replaced with a .32 SX-HX, identical to the .32 SX-H except in its pull-start mechanism attached to the rear of the crankcase. Although it added weight, the pull-start mechanism would be beneficial for field operations, negating the need for an external electric power source to supply an electric starter.

Engine starting, even with the revised pull start, still proved nearly impossible due to the drive train drag and low inertia. A decision was made to abandon the use of small IC engines in place of a much more robust motor. While the motor size and weight was incapable of flight, testing could easily be accomplished for all relevant geometries and conditions.

The evolution of the decision has resulted in a robust test vehicle, suitable for effectively characterizing the thrust performance and power load of the ducted rotor system. The use of a large electric motor provides a power source sufficient for testing the performance envelope of the design. Engine selection for the final flight vehicle can be completed after requirements have been set, based on knowledge gained from tests with the electric motor.

[THIS PAGE INTENTIONALLY LEFT BLANK]

Chapter 3: Theoretical Performance

3.1 *Rotorcraft Aerodynamics*

The performance of a rotor or propeller can be calculated using several methods, each with differing accuracy. Momentum theory treats the rotor as an actuator disk, which can maintain a pressure differential between the top and bottom surfaces. More accurate models treat the disk as multiple concentric rings, but the fundamental theory remains unchanged. Blade element theory treats the rotor blades as wing sections and computes the local lift and drag produced by a section of each blade as a function of the local induced velocity and blade orientation.

Although the momentum and blade element theories presented herein have been developed from Johnson [6] and Leishman [10], they are both commonly used and accepted. Both models are complicated by the convoluted flow around two contrarotating coaxial rotors surrounded by a duct, as is the case with the PUAUV.

3.1.1 Momentum Theory

A propeller or rotor produces thrust by accelerating a mass of fluid. The rotors of a helicopter in hover draw still air from above and propel it downward, yielding a vertical upward thrust. An airplane propeller draws in air traveling at a relative velocity equal to

the airplane speed through the air, and accelerates it rearward to produce thrust. The PUAUV shall perform both tasks, although only the hover regime will be discussed in this report.

Momentum theory allows the calculation of thrust and power by way of three conservation equations. Mass must be conserved within the system, usually defined by a control volume enveloping the rotor and upstream and downstream wake.

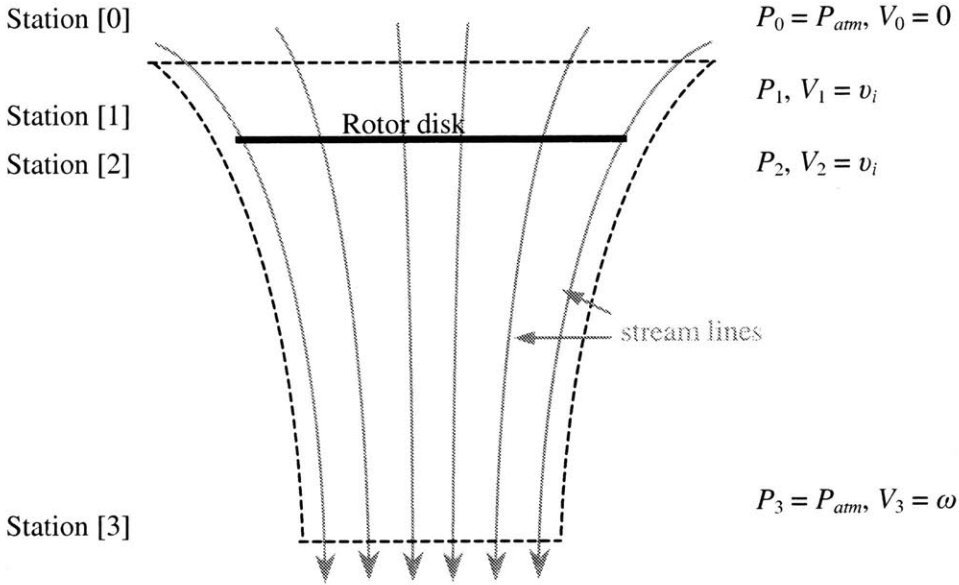


Figure 3.1 Helicopter rotor control volume.

Variable subscripts denote the station, or location across the control volume, of interest. Conservation of mass states that the mass flux through the system, with surface S , air density ρ and velocity vector \vec{V} , must be zero

$$\oiint_S \rho \vec{V} \cdot d\vec{S} = 0. \tag{3-1}$$

Conservation of momentum allows the calculation of thrust from the summation of momentum flux through the same control volume

$$T = \oint_S p d\bar{S} + \oint_S (\rho \vec{v} \cdot d\bar{S}) \vec{v} , \quad (3-2)$$

where p is pressure.

Based on the conservation of energy for the system, the work needed to produce thrust is found to be

$$W = \oint_S \frac{1}{2} \rho (\vec{v} \cdot d\bar{S}) |\vec{v}|^2 . \quad (3-3)$$

Note that this work manifests itself as the change in kinetic energy that accompanies the production of thrust. Power, P , is work per unit of time, or the time rate of change of Equation (3-3).

Equation (3-1) means that the mass of air flowing into the control volume of Figure 3.1 at Station 0 is equal to the mass flowing out at Station 3 and also the same as the mass flow through the rotor at Stations 1 and 2,

$$\dot{m} = \iint_S \rho \vec{v} \cdot d\bar{S} = \iint_S \rho \vec{v} \cdot d\bar{S} = \iint_S \rho \vec{v} \cdot d\bar{S} \quad (3-4) \text{ (a)}$$

$$\dot{m} = \rho A_1 v_i = \rho A_3 \omega \quad (3-4) \text{ (b)}$$

where v_i is the inflow velocity, or induced velocity at the rotor and ω is the downstream velocity (see Figure 3.1).

Recalling that thrust is the rate of momentum flux through the system, Equation (3-2) becomes

$$\vec{F} = T = \iint_S \rho (\vec{v} \cdot d\bar{S}) \vec{v} - \iint_S \rho (\vec{v} \cdot d\bar{S}) \vec{v} . \quad (3-5)$$

The pressure term is not included because both the inlet and exit ends of the control volume are at an equal atmospheric pressure.

Because the velocity far upstream is zero, Equation (3-5) becomes simply

$$T = \iint \rho (\vec{V} \cdot d\vec{S}) \vec{V} = \dot{m} \omega. \quad (3-6)$$

The power required to produce this thrust is defined by using Equation (3-3) as

$$P_i = \iint \frac{1}{2} \rho (\vec{V} \cdot d\vec{S}) \vec{V}^2 - \iint \frac{1}{2} \rho (\vec{V} \cdot d\vec{S}) \vec{V}^2. \quad (3-7)$$

The power required in hover, or work done by the rotor per unit of time, is

$$P_i = T v_i. \quad (3-8)$$

The velocity upstream is zero; therefore the second term of Equation (3-7) is dropped.

This leads to the equality

$$T v_i = \frac{1}{2} \dot{m} \omega^2 = \frac{1}{2} (\rho A v_i) \omega^2, \quad (3-9)$$

which, when combined with Equation (3-6) yields

$$v_i = \frac{1}{2} \omega. \quad (3-10)$$

From Equation (3-4) (b) we see that the wake area A_3 is half the rotor disk area A .

Combining this result with Equation (3-8) leads to

$$T = \dot{m} \omega = 2 \rho A v_i^2. \quad (3-11)$$

Rearranging,

$$v_i = \sqrt{\frac{T}{2 \rho A}}. \quad (3-12)$$

We can now solve for the induced power P_i , as a function of thrust T .

$$P_i = T v_i = T \sqrt{\frac{T}{2 \rho A}} = \frac{T^{3/2}}{\sqrt{2 \rho A}} \quad (3-13)$$

Note that the power is a function of $1/\sqrt{2A}$. Neglecting friction losses as well as weight and structural problems, an infinitely large rotor would yield the minimum induced power. The viscous drag of such a large rotor actually reduces the optimal size, and operational, weight and cost constraints further reduce the ‘best’ rotor size for a helicopter.

The disk loading, DL of a helicopter is the ratio of the total thrust to rotor disk area

$$DL = T/A = 2\rho v_i^2, \quad (3-14)$$

while the power loading, PL defines the amount of thrust for a given power

$$PL = \frac{T}{P} = \sqrt{\frac{2\rho A}{T}} = \sqrt{\frac{2\rho}{DL}} = v_i^{-1}. \quad (3-15)$$

Its reciprocal $1/PL$ is equal to the induced velocity, and is often referred to as the rotor efficiency parameter. Note that Equation (3-15) accounts only for induced power P_i . Blade friction and other losses increase the power consumption.

Profile drag, D , multiplied by the local blade velocity and radius can be integrated along the blade for all N_b blades to yield profile power.

$$P_o = N_b \Omega \int_0^R (Dy) dy \quad (3-16)$$

The radial position along the blade is denoted by y , while the tip radius is R .

The drag is defined by

$$D(y) = \frac{1}{2} \rho V_{local}^2 cC_d = \frac{1}{2} \rho (\Omega y)^2 cC_d. \quad (3-17)$$

For the simplified case of constant C_d independent of Reynold's number Re and Mach number M , the profile power becomes

$$P_o = \frac{1}{8} \rho N_b \Omega^3 c C_{d_o} R^4. \quad (3-18)$$

While Equations (3-14) and (3-15) provide a way of comparing general vehicle parameters, non-dimensionalization allows direct comparison of many more specific parameters.

The thrust and power coefficients are defined in terms of thrust and power, disk area A , and rotor tip speed

$$C_T = \frac{T}{\rho A V_{tip}^2} = \frac{T}{\rho A (\Omega R)^2}, \quad (3-19)$$

$$\text{and } C_{P_i} = \frac{P_i}{\rho A V_{tip}^3} = \frac{P_i}{\rho A (\Omega R)^3}, \quad (3-20)$$

where the rotor tip speed is calculated by multiplying the rotor frequency Ω , by the rotor radius R .

Using the profile power from Equation (3-18) and using the non-dimensionalization shown above, we find the profile power coefficient to be

$$C_{P_o} = \frac{1}{8} \left(\frac{\rho N_b \Omega^3 c C_{d_o} R^4}{\rho A \Omega^3 R^3} \right) = \frac{1}{8} \left(\frac{N_b c R}{A} \right) C_{d_o} \quad (3-21) \text{ (a)}$$

$$= \frac{\sigma_{rotor} C_{d_o}}{8}, \quad (3-21) \text{ (b)}$$

where the rotor solidity

$$\sigma_{rotor} = \frac{A_{blades}}{A_{disk}} = \frac{N_b c R}{A} = \frac{N_b c R}{\pi R^2} = \frac{N_b c}{\pi R} \quad (3-22)$$

is the ratio of total blade area to disk area.

The induced velocity can be non-dimensionalized in terms of Ω and R as well.

$$v_i = \lambda_i \Omega R \quad (3-23)$$

Rearranging yields

$$\lambda_i = \frac{v_i}{\Omega R} = \frac{1}{\Omega R} \sqrt{\frac{T}{2\rho A}} = \sqrt{\frac{T}{2\rho A(\Omega R)^2}} = \sqrt{\frac{C_T}{2}}, \quad (3-24)$$

where λ_i is the induced inflow ratio.

Using a modified version of Equation (3-15) and Equation (3-24) leads to the power coefficient as a function of thrust coefficient

$$C_{P_i} = C_T \lambda_i = \frac{C_T^{3/2}}{\sqrt{2}}. \quad (3-25)$$

In reality, the induced power is slightly higher than theory predicts due to non-ideal effects. In the above equations we have assumed that the inflow is uniform, tip losses and wake swirl do not exist, and there are an infinite number of blades. Experimental results for helicopters show that a linear induced power correction factor, κ , reasonably accounts for these losses. A typical value of κ for a helicopter is 1.15.

$$C_{P_i} = \kappa \frac{C_T^{3/2}}{\sqrt{2}} \quad (3-26)$$

Efficiency of a rotor is difficult to quantify because many parameters are involved and variables that may improve the performance of one design may not be suitable for others. To gain a rough estimate of efficiency, the figure of merit is the quotient of ideal power and actual power.

$$FM = \frac{P_{ideal}}{P_{actual}} = \frac{C_T^{3/2}/\sqrt{2}}{C_{P_{actual}}} = \frac{1}{\sqrt{2}} \frac{C_T^{3/2}}{C_{P_{actual}}} \quad (3-27)$$

If one substitutes the induced plus the profile power for P_{actual} , the following theoretical result is found

$$FM = \frac{\left(C_T^{1/2} / \sqrt{2} \right)}{\kappa \left(C_T^{1/2} / \sqrt{2} \right) + \left(\sigma_{rotor} C_{d_o} / 8 \right)}. \quad (3-28)$$

The numerator denotes the ideal power while the denominator contains induced power and profile power terms from Equations (3-26) and (3-21) (b) respectively. Note that as the thrust coefficient increases FM tends towards $1/\kappa$. For this reason, the figure of merit is only applicable for direct comparison between two rotors of equal C_T .

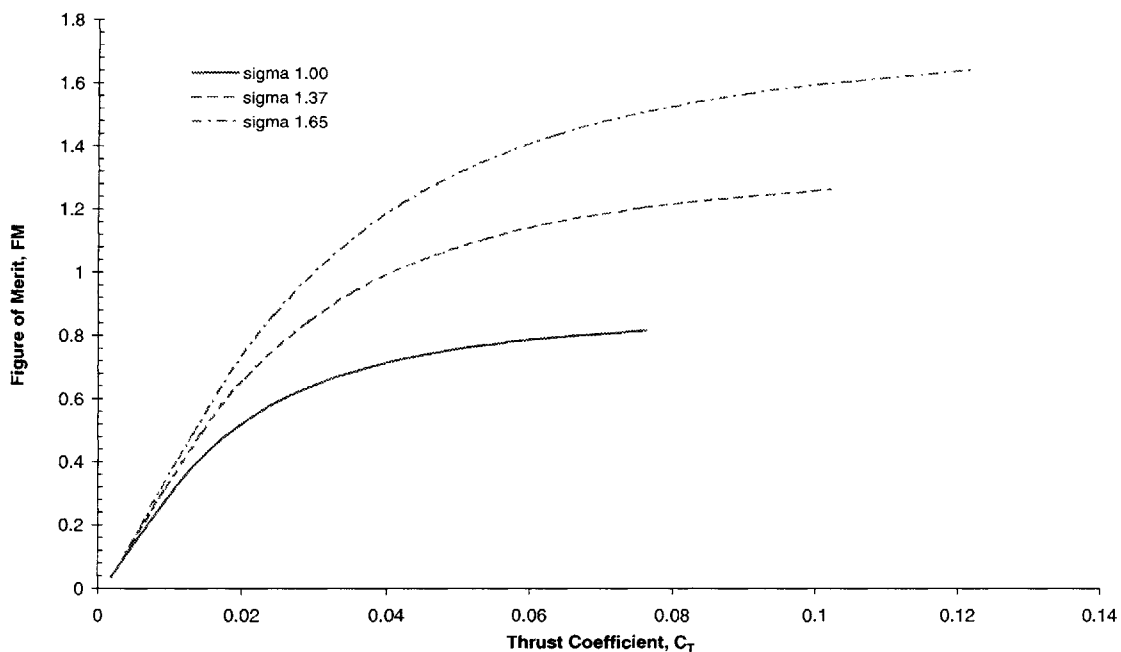


Figure 3.2 Theoretical PUA V figure of merit for different diffusion ratios.

Typically, a figure of merit in the range 0.7 to 0.8 represents good helicopter performance.

3.1.2 Blade Element Theory

The blade element theory (BET) considers a rotor as the finite sum of two-dimensional airfoils. The rotor aerodynamic forces may be calculated radially along the blade and the lift and drag integrated to yield vertical thrust and shaft torque required to turn the rotor. A single blade is considered to represent the behavior of all blades and performance calculations may be accomplished through a simple multiplication by the number of blades. Closed-form solutions can be calculated for certain conditions such as uniform inflow with a simply twisted blade, while iterative solutions are needed for more complex configurations.

Blade element theory allows the calculation of forces, moments and fluid velocities on the blade and in the wake, which cannot be done with momentum theory. This distinctive capability is important as a base from which most other rotorcraft analysis is performed. Specific blade profiles can be analyzed using BET, as well as the influence of the wake on thrust performance. Noise and vibration prediction is also possible with the information that comes from such a model.

To calculate the forces acting on the blade, the blade is broken into finite radial segments of width dy , as denoted in Figure 3.3 (a). Each segment is defined by its radial position, y . Vector velocity and force components are then calculated for each segment, where Figure 3.3 (b) illustrates the forces and velocities acting in the plane perpendicular to the rotor axis of rotation.

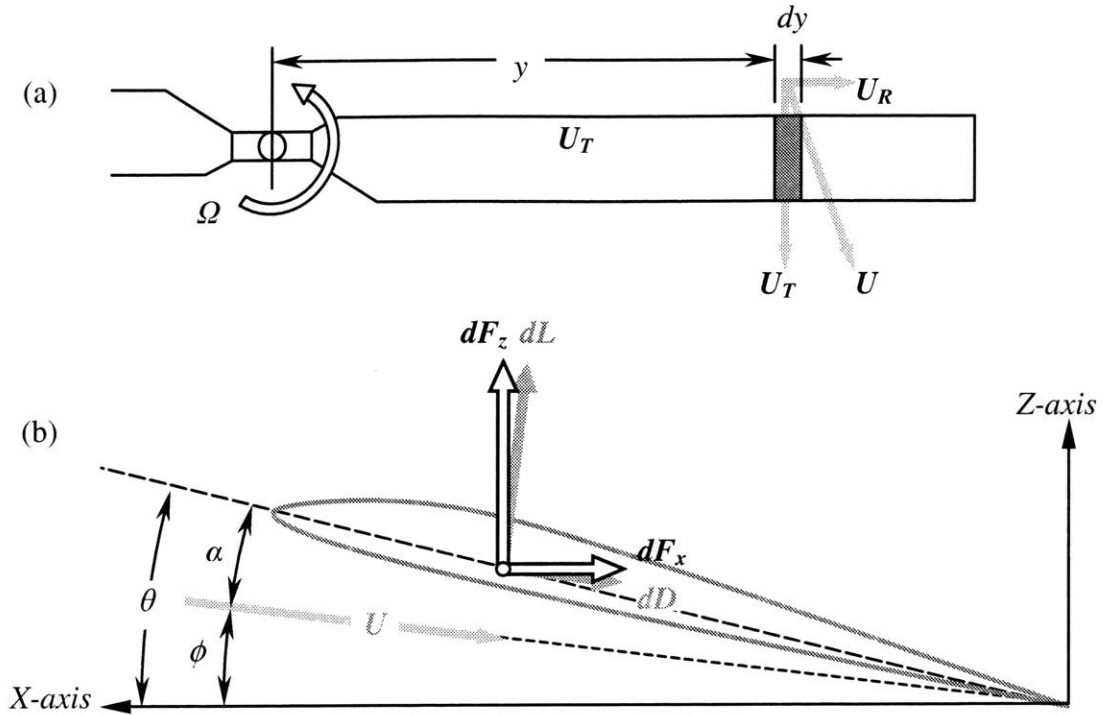


Figure 3.3 Inflow and force components of a blade element. From above (a) and spanwise (b).

The local lift and drag are calculated as functions of the velocity magnitude, local lift and drag coefficients, and chord.

$$dL = \frac{1}{2} \rho U^2 c C_l dy \quad (3-29)$$

$$dD = \frac{1}{2} \rho U^2 c C_d dy \quad (3-30)$$

The force components are referenced to the local velocity vector at the location of the specific blade element. The relative velocity is a function of the blade rotational motion and the downward induced velocity through the disk. As shown in Figure 3.3 (a), there is a radial component of velocity, U_R that is manifested in forward flight. However, the lift is a function of only the chordwise flow. The total velocity is then the sum

$$U = \sqrt{U_T^2 + U_P^2 + U_R^2} \cong \sqrt{U_T^2 + U_P^2} . \quad (3-31)$$

We consider only airflow perpendicular to the blade axis, represented by the rightmost part of (3-31) for simple blade element theory analysis. The general inflow angle from the induced flow is then

$$\phi = \tan^{-1}\left(\frac{U_P}{U_T}\right). \quad (3-32)$$

For a helicopter rotor the induced angle is generally small, so a small angle assumption is valid.

$$\phi \approx U_P/U_T \quad (3-33)$$

The angle of attack, as illustrated in Figure 3.3 is then the difference between the blade angle θ and inflow angle ϕ .

$$\alpha = \theta - \phi \quad (3-34)$$

$$\alpha \cong \theta - \frac{U_P}{U_T} \text{ for } \phi \ll 1 \quad (3-35)$$

The lift and drag coefficients of the blade element are functions of angle of attack, α , and are also dependent upon Reynolds number, Re , and Mach number, M , although the latter two effects are sometimes neglected. The lift coefficient is typically modeled as a linear function of α , with a slope C_{l_α} of 2π . Drag coefficient is modeled as a quadratic function of α . According to Johnson [6], a typical drag coefficient for helicopter blades is

$$C_d = 0.0087 - 0.0216\alpha + 0.400\alpha^2. \quad (3-36)$$

Although local blade forces in the blade axis or inflow axis are occasionally useful, one generally cares more about the total forces on the rotor hub and helicopter. First, we will calculate the forces in the rotor hub axis. This yields the vertical thrust force F_z , acting

on the blade and hub parallel to the rotor shaft axis, and the radial drag force F_x , acting normal to the blade axis and rotor shaft axis.

$$dF_z = dL \cos \phi - dD \sin \phi \quad (3-37)$$

$$dF_x = dL \sin \phi + dD \cos \phi \quad (3-38)$$

The vertical thrust increment is then the sum of the local vertical force dF_z for all N_b blades. The incremental torque is found similarly, except the x-axis is of concern and the force is multiplied by the moment arm y of the location. Power is torque multiplied by radial velocity, Ω .

$$dT = N_b dF_z \cong N_b dL = \frac{1}{2} N_b \rho U^2 c C_l dy \quad (3-39)$$

$$dQ = N_b dF_x y \cong N_b (\phi dL + dD) y \quad (3-40)$$

$$\begin{aligned} dP &= dQ \cdot \Omega = N_b dF_x y \Omega \cong N_b (\phi dL + dD) y \Omega \\ &\cong \frac{1}{2} N_b \rho U^2 c (\phi C_l + C_d) \Omega y dy \end{aligned} \quad (3-41)$$

The last term in each of the above equations is valid for small angles where $\sin \phi \approx \phi$ and $\cos \phi \approx 1$. The thrust, torque and power are the integral sums of the above equations over the radius, R of the blades.

$$T = \int_0^R dT = \int_0^R \rho N_b dL = \frac{1}{2} \rho N_b \int_0^R U^2 c C_l dy \quad (3-42)$$

$$P = \frac{1}{2} \rho N_b \int_0^R U^2 c (\phi C_l + C_d) \Omega y dy \quad (3-43)$$

The incremental thrust, torque and power can also be used to find their equivalent coefficients.

$$dC_T = \frac{N_b dL}{\rho A (\Omega R)^2} = \frac{N_b (\frac{1}{2} U^2 c C_l dy)}{\rho (\pi R^2) (\Omega R)^2} = \frac{1}{2} C_l \left(\frac{N_b c}{\pi R} \right) \left(\frac{y}{R} \right)^2 d \left(\frac{y}{R} \right) \quad (3-44)$$

$$dC_Q = \frac{N_b (\phi dL + dD) y}{\rho A (\Omega R)^2 R} \quad (3-45)$$

$$dC_p = \frac{N_b (\phi dL + dD) y \Omega}{\rho A (\Omega R)^3} \quad (3-46)$$

In the non-dimensional form, the rotor radius becomes $r = y/R$ and $U/\Omega R = \Omega y/\Omega R = y/R = r$.

Recalling that the rotor solidity $\sigma_{rotor} = (N_b c)/(\pi R)$, we can simplify Equation (3-44) to

$$dC_T = \frac{1}{2} \sigma_{rotor} C_l r^2 dr \quad (3-47)$$

The torque and power coefficients follow similarly and are equal.

$$\begin{aligned} dC_Q \equiv dC_P &= \frac{N_b \left(\frac{1}{2} U_T^2 c (\phi C_l + C_d) dy \right) \Omega y}{\rho \pi \Omega^2 R^3} \\ &= \frac{1}{2} \sigma_{rotor} (\phi C_l + C_d) r^3 dr \end{aligned} \quad (3-48)$$

The induced inflow ratio, $\lambda_i = v_i/\Omega R$, comes from Equation (3-24).

$$\lambda_i = \frac{v_i}{\Omega R} = \frac{v_i}{\Omega y} \left(\frac{\Omega y}{\Omega R} \right) = \frac{U_P}{U_T} \left(\frac{y}{R} \right) = \phi r \quad (3-49)$$

Because $\phi = \lambda_i/r$, the power coefficients becomes

$$dC_p = \frac{1}{2} \sigma_{rotor} (\lambda_i C_l r^2 + C_d r^3) dr. \quad (3-50)$$

Also, for the linear lift curve case where $C_l = \alpha \cdot C_{l\alpha}$ and recalling that

$\alpha = \theta - \phi = \theta - \lambda_i/r$, the thrust coefficient follows as

$$dC_T = \frac{\sigma_{rotor} C_{l\alpha}}{2} (\theta r^2 - \lambda_i r) dr. \quad (3-51)$$

Integrating Equations (3-47) and (3-50) yields the thrust and power coefficient.

$$C_T = \frac{1}{2} \sigma_{rotor} \int_0^1 C_l r^2 dr \quad (3-52)$$

$$C_p = \frac{1}{2} \sigma_{rotor} \int_0^1 (\lambda_i C_l r^2 + C_d r^3) dr \quad (3-53)$$

Blade element theory and momentum theory can be combined to provide the inflow profile $\lambda_i(r)$. The thrust can be found based on momentum theory, where the incremental area $dA = 2\pi y dy$ is an annulus of width dy at a discretized radius y .

$$dT = 2\rho v_i^2 dA = 4\pi\rho v_i^2 y dy \quad (3-54)$$

In coefficient form this becomes

$$dC_T = 4\lambda_i^2 r dr, \quad (3-55)$$

while the induced power coefficient is

$$dC_{P_i} = 4\lambda_i^3 r dr. \quad (3-56)$$

Equating results from the BET (Equations (3-50) and (3-56)) gives

$$dC_T = 4\lambda_i^2 r dr = \frac{\sigma_{rotor} C_{l_\alpha}}{2} (\theta r^2 - \lambda_i r) dr. \quad (3-57)$$

Solving Equation (3-57) results in the quadratic equation for the inflow profile as a function of r

$$\lambda_i(r) = \frac{\sigma_{rotor} C_{l_\alpha}}{16} \left[\sqrt{1 + \frac{32}{\sigma_{rotor} C_{l_\alpha}} \theta r} - 1 \right], \quad (3-58)$$

where σ_{rotor} , θ , and C_{l_α} can all be functions of r . This combined theory is called blade element momentum theory (BEMT). The induced velocity and thrust can also be computed iteratively, which is often the only option when complex blade geometries and lift and drag coefficients are considered.

3.1.3 Coaxial Momentum Theory

As a first approximation to the case of two coaxial rotors within a duct, we will consider the case of unducted contrarotating coaxial rotors as they are used on many Russian

Kamov Design Bureau helicopters. The two rotors are considered to be closely spaced, so that the wake of the upper rotor has not contracted when it passes through the second rotor. This means that the area of each rotor is equal ($A_{rotor1} = A_{rotor2} = A$). Based on continuity (Equation (3-4) (b)) the induced velocity through each rotor must be equal. If the area and induced velocity are equal we can reasonably assume that the thrust is equally distributed between the two rotors. The total thrust is then $2T$, where T is the individual thrust from each rotor.

$$(v_i)_{coaxial} = \sqrt{\frac{2T}{2\rho A}} = \sqrt{\frac{T}{\rho A}} \quad (3-59)$$

Substituting into Equation (3-13) we find that the total induced power between the two rotors is

$$(P_i)_{coaxial} \Big|_{ideal} = 2T(v_i)_{coaxial} = 2T \sqrt{\frac{T}{\rho A}} = \frac{2T^{3/2}}{\sqrt{\rho A}} = \frac{(2T)^{3/2}}{\sqrt{2\rho A}}, \quad (3-60)$$

$$\text{and } (P_i)_{coaxial} \Big|_{actual} = \kappa \kappa_{int} (P_i)_{coaxial} \Big|_{ideal} = \frac{\kappa_{int} \kappa (2T)^{3/2}}{\sqrt{2\rho A}}, \quad (3-61)$$

where Equation (3-61) includes correction factors to account for non-ideal losses.

Due to the halved effective disk area of a coaxial rotor compared to two non-overlapping rotors of the same size, the interference induced losses amount to an increase in induced power of $\kappa_{int} = \sqrt{2} = 1.41$. Tests of actual aircraft show that interference actually yields values of κ_{int} that are closer to 1.16 for coaxial helicopters. The difference is due in part to vertical rotor separation. Helicopters with coaxial rotors tend to have large rotor separation, causing the second rotor to be only partially in the nearly fully developed wake of the first. In theory, if the second rotor is within the fully developed wake of the

first, such as far downstream, the theoretical interference factor is 1.28. In this case only half the rotor is in the wake of the first rotor, while the outer half of the rotor area is in free air. For the ducted rotor case, one may assume that there is negligible contraction, causing the rotors to behave as though they were closely spaced.

Another effect of contrarotation is reduction of swirl in the wake. The regular induced power correction coefficient κ generally accounts for the energy lost in the rotor wake and will be reduced if swirl is diminished. It is possible that the seemingly small experimentally determined interference coefficient κ_{int} , of 1.16 mentioned above, was calculated with the assumption of a regular induced power correction factor κ , of 1.15, rather than a smaller κ that accounts for swirl. The total correction $\kappa\kappa_{int}$ may have therefore been incorrectly distributed between κ and κ_{int} .

The profile power is theoretically unchanged from the single rotor case, but the total rotor solidity for a pair of equal rotors is twice that of the single rotor. This has the effect of doubling the profile power losses,

$$(P_o)_{coaxial} = \rho A (\Omega R)^3 \left(\frac{2\sigma_{rotor} C_{d_o}}{8} \right), \quad (3-62)$$

where σ_{rotor} is the solidity of a single rotor.

3.1.4 Ducted Rotor Performance

This section has thus far covered the momentum theory model of two closely separated rotors of equal dimension and shared thrust. While the duct provides the benefit of

reduced or eliminated tip vortices, thus reducing κ , its primary purpose is the boost in efficiency that comes with diffusion, or spreading of the induced flow from the rotor disk.

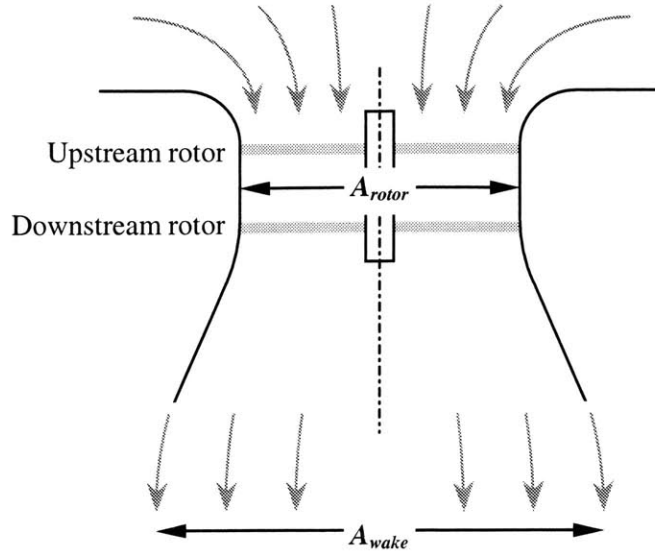


Figure 3.4 Ducted rotor with diffuser exit.

Incorporating a diffuser at the exit of a ducted rotor allows the effective wake area to be changed while maintaining a fixed rotor disk area. From Equations (3-8) and (3-11), we know that the power is dependent upon the induced velocity passing through the rotor disk, v_i , while the thrust is a function of the total change in momentum, and thus dependent upon the far wake velocity ω and area A_{wake} . The diffuser allows these parameters to be altered to better suit performance and efficiency objectives.

$$A_{rotor} = A \quad (3-63)$$

$$A_{wake} = \sigma_{duct} A \quad (3-64)$$

where σ_{duct} , is the duct diffusion ratio.

Therefore, we can rewrite Equation (3-4) (b) as

$$\dot{m} = \rho A v_i = \rho A_{wake} \omega = \sigma_{duct} \rho A \omega. \quad (3-65)$$

This means that

$$\omega = \frac{v_i}{\sigma_{duct}}. \quad (3-66)$$

Note that σ_{duct} is not based on the ratio of rotor disk area to duct exit area, but rather to the area of the far wake. For an unducted rotor, $\sigma_{duct} = 0.5$.

Considering again that thrust is the time rate of momentum flux through the system, the total thrust is

$$T_{total} = T_{rotor} + T_{duct} = \dot{m}\omega. \quad (3-67)$$

Using the constitutive equation, this becomes

$$T_{total} = \rho \frac{A}{\sigma_{duct}} v_i^2. \quad (3-68)$$

The induced velocity is then

$$v_i = \sqrt{\frac{\sigma_{duct} T_{total}}{\rho A}}. \quad (3-69)$$

Applying the Bernoulli equation at the inlet

$$p_o = p_1 + \frac{1}{2} \rho v_i^2 = p_{am} \quad (3-70)$$

and the exit

$$p_2 + \frac{1}{2} \rho v_i^2 = p_3 + \frac{1}{2} \rho \omega^2 = p_{am} + \frac{1}{2} \rho \omega^2 \quad (3-71)$$

allows the computation of the rotor thrust, T_{rotor} .

$$T_{rotor} = A(\Delta p) = A(p_2 - p_1) \quad (3-72)$$

Solving for p_1 and p_2 and substituting the results into Equation (3-72) yields

$$T_{rotor} = \frac{1}{2} \rho A \omega^2. \quad (3-73)$$

The contribution to thrust can best be seen by its ratio to total thrust

$$\frac{T_{rotor}}{T_{total}} = \frac{\frac{1}{2} \rho A \omega^2}{\rho A v_i \omega} = \frac{\omega}{2v_i} = \frac{1}{2\sigma_{duct}} \quad (3-74)$$

Although thrust is produced by both the duct and the rotors, induced and blade profile power are absorbed only from the rotors. Thus

$$\begin{aligned} (P_i)_{rotor} &= T_{rotor} v_i = \left(\frac{T_{total}}{2\sigma_{duct}} \right) \sqrt{\frac{\sigma_{duct} T_{total}}{\rho A}} \\ &= \frac{T_{total}^{3/2}}{\sqrt{4\sigma_{duct} \rho A}}. \end{aligned} \quad (3-75)$$

Dividing Equation (3-75) by the induced power for an unducted rotor becomes

$$\frac{(P_i)_{ducted}}{(P_i)_{unducted}} = \frac{\frac{T_{total}^{3/2}}{\sqrt{4\sigma_{duct} \rho A}}}{\frac{T_{total}^{3/2}}{\sqrt{2\rho A}}} = \frac{1}{\sqrt{2\sigma_{duct}}}. \quad (3-76)$$

Equation (3-76) illustrates the effect of duct diffusion on efficiency. The above theoretical equations do not account for blade profile drag losses or skin friction drag on the duct. It should also be noted that obtaining large duct diffusion is difficult, as the adverse pressure gradient of a diffuser yields significant losses and the final wake area is often less than expected. This will be covered in Section 3.2.3.

3.2 Other Inlet and Diffuser Effects

The inlet, duct, and diffuser constrain the inlet and exit airflow. The pressure and shear stresses imparted on the vehicle surfaces by the air cause drag and can also provide thrust. Skin friction drag is generally less important for higher Reynolds numbers than pressure drag at the diffuser and inside the inlet lip, caused by flow separation and an

adverse pressure gradient. If a sharp inlet is installed, the air has difficulty maneuvering around a sharp corner and can separate, thus causing losses. A conical diffuser creates an inherent adverse pressure gradient, which leads to losses as well.

3.2.1 Inlet Thrust Augmentation

Like a wing, airflow over the inlet surface causes the inlet to experience lift. Through the Bernoulli equation, one can follow a streamline entering the rotors to calculate the pressure along the profile as a function of the velocity. A simplistic model is based on semi-concentric sphere caps that are normal to the inlet and flange surfaces where they meet (Figure 3.5). The surface area, S , of each sphere cap defines the velocity ratio between the surface area S , and the duct or rotor area, A , for each streamline. The velocity on a given sphere cap is thus the induced velocity at that streamline where it enters the rotor multiplied by the ratio of rotor disk area to sphere cap surface area.

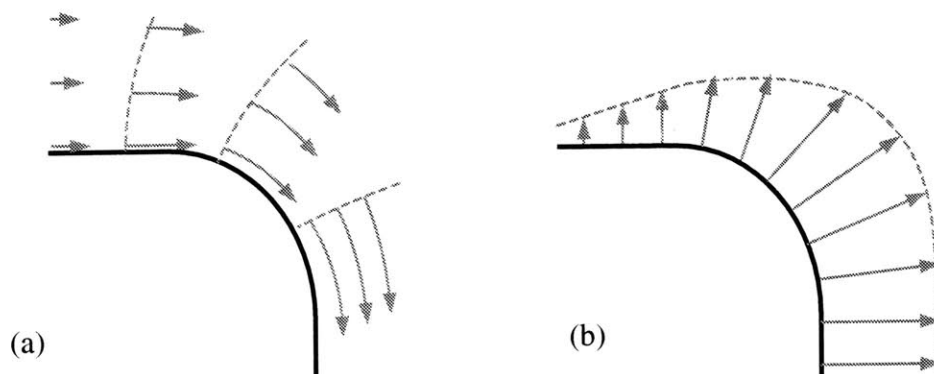


Figure 3.5 Streamlines (a), and pressure distribution (b) over the inlet.

Figure 3.5 (a) and Figure 3.6 illustrate the velocity assumption. The sphere cap surface is solely a function of the radius, r , with the constraint that it is always perpendicular to the inlet or duct surface and is spherical in shape. The surface area will be denoted S .

The axial thrust produced by this lift is simply the product integral of pressure and area in the axial direction. Note that all forces acting radially cancel through symmetry.

$$T_{inlet} = \int_0^{(2\pi)(r_d+r_i+f)} \int_{(r=r_d)} (\Delta p)(\hat{i} \cdot \underline{n}) dr d\theta \quad (3-77)$$

The dot product of the duct axis vector \hat{i} and the local surface normal \underline{n} translates the pressure and area into of the duct axis.

From Bernoulli,

$$p_{am} + 0 = p_{inlet} + \frac{1}{2} \rho V_{inlet}^2 \quad (3-78)$$

$$\Delta p = p_{am} - p_{inlet} = \frac{1}{2} \rho V_{inlet}^2 \quad (3-79)$$

Assuming that the velocity profile through the surface S is everywhere proportional to the velocity at the duct of surface area A , continuity can be used to yield the velocity at the surface as a function of r and v_i .

$$\begin{aligned} \dot{m} &= \rho A v_i = \rho S V_{inlet} \\ V_{inlet} &= v_i \frac{A}{S} = v_i \frac{\pi r_d^2}{S} \end{aligned} \quad (3-80)$$

For the limit where $r = r_d$, the duct radius, the surface area S becomes the duct area A and $V_{inlet} = v_i$. When $r > (r_d + r_i)$, where r_i is the inlet lip radius, the surface area S becomes that of a hemisphere, with surface area $S = 2\pi r^2$.

A sphere cap is the surface obtained when the portion of a sphere above a certain plane is considered. The surface area of a sphere cap is $S = 2\pi r h$, where r is the radius of the circle created by the intersection of the sphere and the plane, and h is the distance between the center of the circle and the top of the sphere. In this case, r is the same radial dimension used in the integral of Equation (3-77).

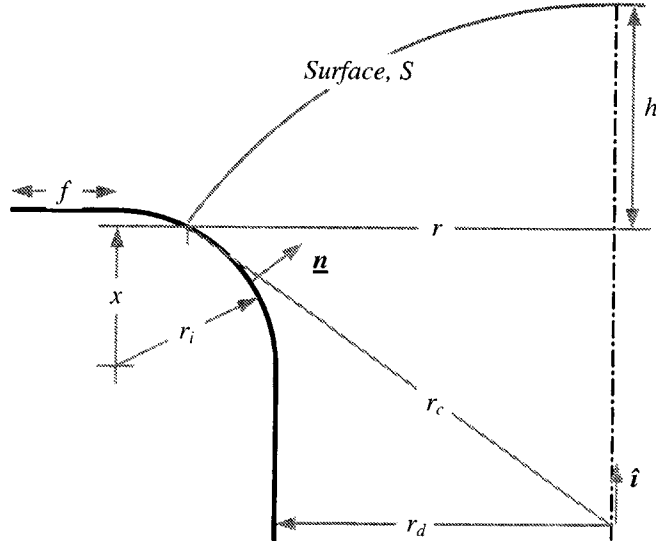


Figure 3.6 Inlet surface area geometry.

Using the geometry of Figure 3.6, the surface area S can be solved as a function of radial position r , duct radius r_d , and inlet lip radius of curvature r_i . The radius of the sphere defining S is r_c which can be found from

$$r_c = \frac{r^2 + h^2}{2h}. \quad (3-81)$$

One can solve for the sphere radius (or in the two-dimensional case displayed, the circle radius), from the duct geometry as

$$r_c = \frac{rr_i}{\sqrt{r_i^2 - (r_i + r_d - r)^2}} = \frac{rr_i}{\sqrt{(r - r_d)(2r_i + r_d - r)}}. \quad (3-82)$$

Similarly, a scalar pressure magnitude correction based on the forward component of the surface normal vector

$$m = \underline{n} \cdot \hat{i} = \frac{r}{r_c} = \frac{\sqrt{(r - r_d)(2r_i + r_d - r)}}{r_i} \quad (3-83)$$

is equivalent to the dot product of the surface normal vector and the duct axis vector.

Using Equations (3-86) and (3-82), the surface area S for the condition $r_d < r < r_d + r_i$ is

$$S_{lip} = \frac{2\pi(r - r_d)r_i r^2}{r_i^2 - (r_i + r_d - r)^2} = \frac{2\pi r^2 r_i}{(2r_i + r_d - r)}. \quad (3-84)$$

If a flange is attached to the periphery of the inlet, a greater surface area can be used to augment thrust through lift. The flange will be considered to have a radial dimension from the inlet radius of length f . For the flanged case, recall that the surface S , which defines the velocity profile, is that of a hemisphere.

$$S_{flange} = 2\pi r^2 \quad (3-85)$$

The total inlet thrust is then the sum of two integrals of thrust in the axial direction. From Equations (3-80), (3-84) and (3-85), the total thrust can be calculated.

$$T_{inlet} = \int_0^{(2\pi)(r_d+r_i+f)} \int_{(r=r_d)} (\Delta P_{inlet} m) dr d\theta = T_{lip} + T_{flange} \quad (3-86)$$

First, based on the surface S perpendicular to the lip surface, the thrust for $r_d < r < r_d + r_i$

$$T_{lip} = \frac{1}{4} \rho \pi v_i^2 \int_{r=r_d}^{r_d+r_i} \left(\frac{r_d^4 (2r_i + r_d - r)^2 \sqrt{(r - r_d)(2r_i + r_d - r)}}{r^3 r_i^3} \right) dr \quad (3-87)$$

The flange thrust based on the hemisphere of radius r for $r > r_d + r_i$

$$T_{flange} = 2\pi \int_{r=r_d+r_i}^{r_d+r+r_i+f_i} \frac{1}{2} \rho v_i^2 \left(\frac{\pi r_d^2}{2\pi r^2} \right)^2 dr \quad (3-88)$$

$$T_{flange} = \frac{1}{4} \rho \pi v_i^2 \int_{r=r_d+r_i}^{r_d+r+r_i+f_i} \left(\frac{r_d^4}{r^3} \right) dr$$

Combining Equations (3-87) and (3-88) results in a total thrust of

$$T_{inlet} = \frac{1}{4} \rho \pi r_d^4 v_i^2 \left\{ \int_{r=r_d}^{r_d+r_i} \left(\frac{1}{r^3} \right) dr + \int_{r=r_d+r_i}^{r_d+r+r_i+f_i} \left(\frac{\sqrt{(r - r_d)(2r_i + r_d - r)^5}}{r^3 r_i^3} \right) dr \right\} \quad (3-89)$$

The above equations are based on several broad assumptions that have been defined before their formulation. However, the choice of v_i is not predefined and has a strong impact on the thrust result. A conservative method would have the inlet surface velocity distribution defined as a function of the average disk induced velocity, while a less conservative approach would define the surface velocity in terms of the high rotor tip induced velocity nearest the duct wall. The choice of v_i is especially significant for an untwisted ducted rotor in which the induced velocity is high at the blade tips.

Experimental surface pressure distribution plots for a ducted fan, presented by Black, Wainauski, and Rohrbach [3], appear to validate the general theory of inlet suction lift, and indicate that the above model is overly conservative, even in the case where tip induced velocity is used.

3.2.2 Inlet Losses

The previous section examined the benefits of a large inlet mouth. In considering the design of an inlet duct, it should be noted that size and weight constraints often prohibit a large inlet lip radius of curvature, however. The effect of inlet thrust augmentation decays with radius as the velocity reduces, while the skin friction drag increases. Thus, there is a point at which the thrust lost to drag equals the thrust gained by augmentation. Operational and external dimension constraints will usually limit the size more than drag considerations.

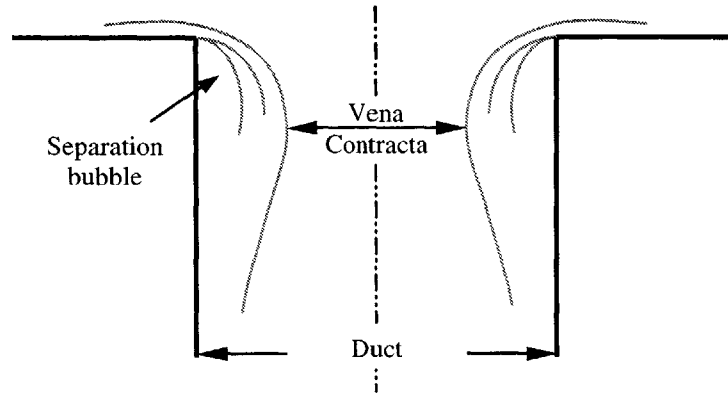


Figure 3.7 Vena contracta.

When the flow separates from the inlet surface, the effective area is decreased, causing the velocity at the throat of the duct to increase. Although not much energy is dissipated in the acceleration of a fluid, the deceleration that must occur as the flow once again conforms to the duct saps energy in the form of a head loss. The head loss can be solved as a pressure loss

$$\Delta p = K_L \left(\frac{\rho v^2}{2} \right) \quad (3-90)$$

where K_L is the loss coefficient. Vena contracta losses are difficult to model. Thus, loss coefficients are found experimentally as a function of r_{inlet}/D_{duct} . In the case of a tube inlet, the loss coefficient (K_L) ranges from near zero for a large radius, to 0.5 in the case of a sharp inlet lip.

Substituting the induced velocity from Equation (3-12) and solving for the lost thrust T_L , it is possible to obtain the thrust lost as a function of total thrust.

$$T_L = \Delta p A = K_L \left(\frac{\rho v_i^2}{2} \right) A \quad (3-91)$$

$$\frac{T_L}{T} = \frac{K_L}{4} \quad (3-92)$$

For a sharp-lipped inlet the thrust lost due to separation and the vena contracta will be approximately 12.5 percent of the total thrust.

Several studies have investigated the effects of inlet lip radius on performance of a ducted propulsor such as the UAV. Taylor [17], found that the thrust efficiency is not greatly affected for inlets with a lip radius to duct diameter ratio great than 0.6. His results and those based on the theory developed from Munson et al [13] are both presented in Figure 3.8 below. Taylor's results indicate a much more drastic drop in performance as the lip radius is brought near zero. This increase in losses due to inlet geometry is probably due to severe lip separation, and the turbulent airflow that is created by the sharp inlet as the flow enters the rotor disk.

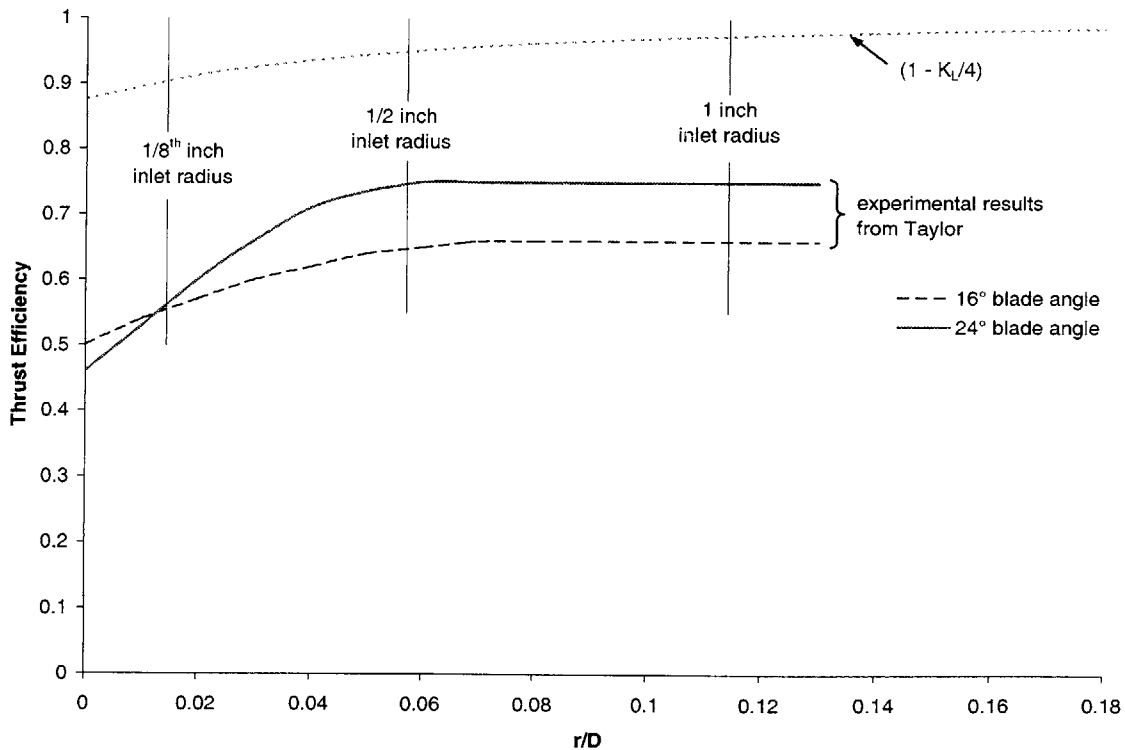


Figure 3.8 Thrust losses due to sharp inlet curvature.

3.2.3 Duct and Diffuser Losses

The duct and diffuser are segments of a tube with internal flow and its attendant losses. Because of its short length, the straight duct portion of the PUAUV only exhibits small skin friction losses. However, the adverse pressure gradient of the diffuser causes more substantial performance losses.

Like the inlet losses, diffuser losses can be accounted for by using Equations (3-90) and (3-91). However, the area and velocity are not simply the induced velocity and duct area, respectively. In the case of a diffuser, the pressure drop occurs over the entire length where the velocity decreases and area increases. Integration must be used to yield the total drop. The result is similar.

$$\frac{T_L}{T} = \frac{K_L}{4\sigma_{duct}^2} \quad (3-93)$$

Though a longer, more gradual diffuser will reduce separation, the skin friction will reduce the efficiency. An optimal diffusion angle for a given ratio will thus exist. As in the case of the inlet, experimental results must be used due to the complex nature of decelerating fluids.

3.3 *PUAUV Numerical Model*

Because we are considering the ducted contrarotating coaxial rotor, three effects must be considered that aren't significant to helicopters. First, the duct diffuser changes the wake flow, increasing the induced flow at the rotor but adding to the overall thrust of the vehicle. Second, the tip vortices that dilute the performance of a helicopter are constrained by the duct, diminishing the need to account for tip effects. Finally, the swirl

of the first rotor is not fully wasted in the wake. Instead, it increases the angle of attack and velocity of the second rotor. Another point to consider is one of computational simplification. Because of its large rotor diameter and low disk loading, the inflow angle on a helicopter rotor is low and the trigonometric functions of the inflow angle can be approximated by their small angle equivalents. The PUAUV and other small, high-disk loading aircraft maintain large blade angles and inflow ratios, which are usually beyond the scope of small angle simplification.

The PUAUV numerical model used to compare with experimental results is a dimensional blade element momentum theory model graphically illustrated in Figure 3.9, which includes duct diffusion. The lift coefficient used in the model is a linear function of α , with slope 2π , while the drag coefficient is a quadratic function of α and Re in the form $C_d = (1.25 + 2.76\alpha + 44.8\alpha^2)Re^{-0.346}$, which is based on the tested NHP tail rotor blade. The blade grip will be considered as a cylinder with $C_d = 9Re^{-0.5}$ due to the low Reynolds number. Duct and inlet losses will not be calculated in the numerical model, but should be considered qualitatively when comparing predicted results to experimental results.

The induced and profile drag of the first rotor induces a swirl in the wake that the second rotor encounters as a higher tangential velocity, U_T . This reduces the inflow angle slightly, thus improving performance of the second rotor and recouping some of the power that would be otherwise lost in a single rotor vehicle where the swirl would be dissipated in the wake. The final swirl behind the second rotor is expected to be small, and will therefore not be included in the numerical model.

The flowchart illustrated below in Figure 3.9 outlines the process by which the Matlab-based computational model calculates the performance of the PUAUV. The model is first initialized with a set of input conditions and an expected induced velocity. The latter can be chosen randomly, and only serves to reduce the time to converge on a solution.

First, the total relative blade velocity, Reynolds number and angles are calculated based on the rotational speed and induced velocity. The lift and drag coefficients can then be found, which are used to find the local lift and drag component for each blade segment. The local thrust values are then used to find the induced velocity for that segment. The process iterates until the total thrust, the sum of all incremental thrust components, converges to a steady value. The final induced velocity can then be used to find the inlet thrust, which is added to the duct thrust to arrive at the total vehicle thrust.

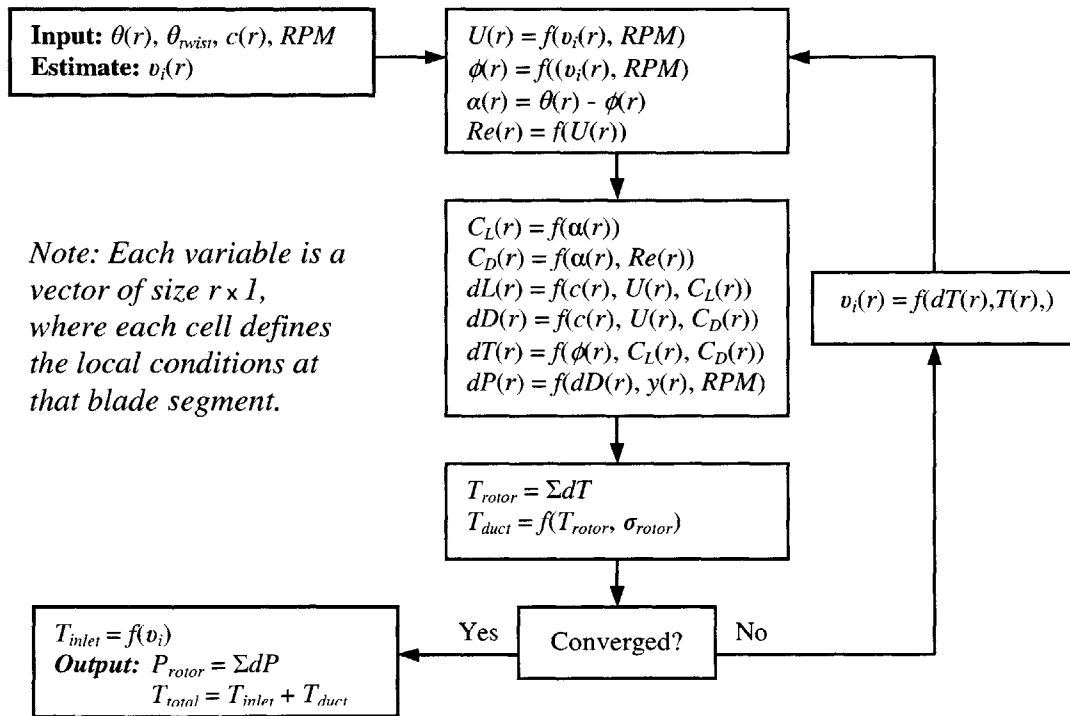


Figure 3.9 Computational Flowchart.

[THIS PAGE INTENTIONALLY LEFT BLANK]

Chapter 4: Experimental Test Apparatus

4.1 Drive Train

The drive train of the test article accomplishes the same tasks as that on the flight vehicle. In both cases, the rotating drive train components provide the mechanical work to drive the rotor blades, while the stationary components center the rotors within the duct. Due to complications of a small internal combustion (IC) engine and the freedom of nearly unlimited energy from an external power supply, an electric motor was substituted for testing. The motor and power supply permit precise speed control while maintaining a clean, low vibration environment unattainable with an IC engine.

4.1.1 Driveline

The driveline is the mechanical intermediary between the power source and the aerodynamic blade components. It includes shafts, gears, bearings, guides and the stationary components required to support all moving components. In the case of the PUAV hover test article, the driveline acts to direct motor torque to the two rotor hubs through six bearings and two gears as illustrated below.

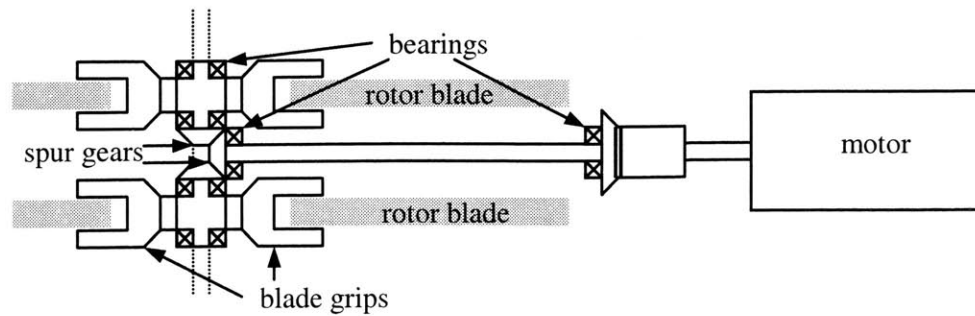


Figure 4.1 Schematic diagram of PUAUV hover test vehicle drive train.

The hover test article driveline was constructed out of machined aluminum and steel components from the PUAUV Beta Prototype. In an effort to reduce aerodynamic blockage and drag, the lower profile lower spar of the Beta Prototype driveline was substituted for the engine cradle, which normally contains the IC engine, flywheel and one-way clutch. Although actual use in a flight vehicle will require that an engine be mounted within the middle of the duct, aerodynamic testing would have been complicated by such components. Future vehicles may entail fairings that would reduce drag, but the design of such fairings would require further study and inclusion in these tests would obscure the pure thrust results.

Low speed torque capabilities of the motor obviated the need for any reduction gearing usually necessary for the high-revving IC engine. The large motor size also hindered any internal mounting options that would have in any case added aerodynamic drag. The motor was therefore mounted transverse to the duct in line with the secondary drive shaft. Screwed to the end of the motor shaft is an aluminum machined coupling, with two lugs comprised of small screw heads affixed to its peripheral face. The lugs match holes in the large reduction spur gear mounted to the outer end of the secondary drive shaft. This

attachment method allows for slight off-axis mounting and takes the form of a universal joint, in addition to allowing some movement axial to the shafts.

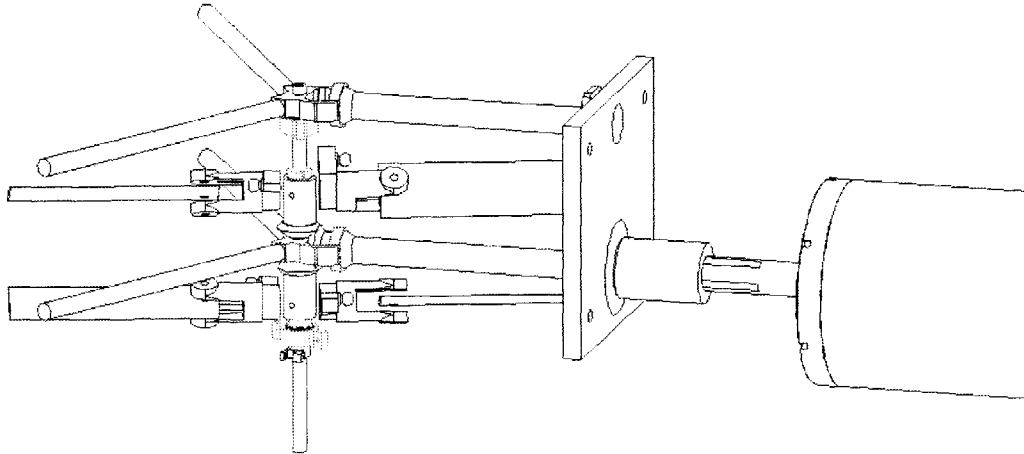


Figure 4.2 PUAV hover test vehicle drive train.

As in the case of the flight vehicle, the hover test article driveline center shaft is held by two pairs of carbon fiber struts mounted axially from the spar end caps 120 degrees from the secondary drive shaft and spars. The struts were screwed to the duct and stabilized by epoxy. This axisymmetric stiffening restricts bending strain of the spars and keeps the center shaft exactly centered within the duct so that blade tip clearance remains constant and blade-to-duct contact is curtailed.

Due to the ultimate need to reverse flow direction in the final flight vehicle, a symmetric, zero-twist rotor blade profile was chosen for initial testing. Although blade twist and camber would yield improved thrust and reduced power required in one direction, performance would be unsuitable in the reverse direction. Negative twist, in which the root is at a higher local blade angle than the tip, tends to equalize the angle of attack and thus improve performance. Reversing the flow direction for the same blade yields an

effective positive twist, in which the root has a lower blade angle than the tip. This could cause the tip to stall while a small or negative root angle of attack would give reduced or reversed thrust. An untwisted symmetric blade affords equal performance in either direction, a compromise that must be made with the need to reverse the direction of flow for the vehicle.

Carbon fiber foam core 29-mm chord NHP tail rotor blades were used for initial tests. These symmetric blades have a thickness to chord ratio of 17%. Rotor solidity, σ_{rotor} is 0.33.

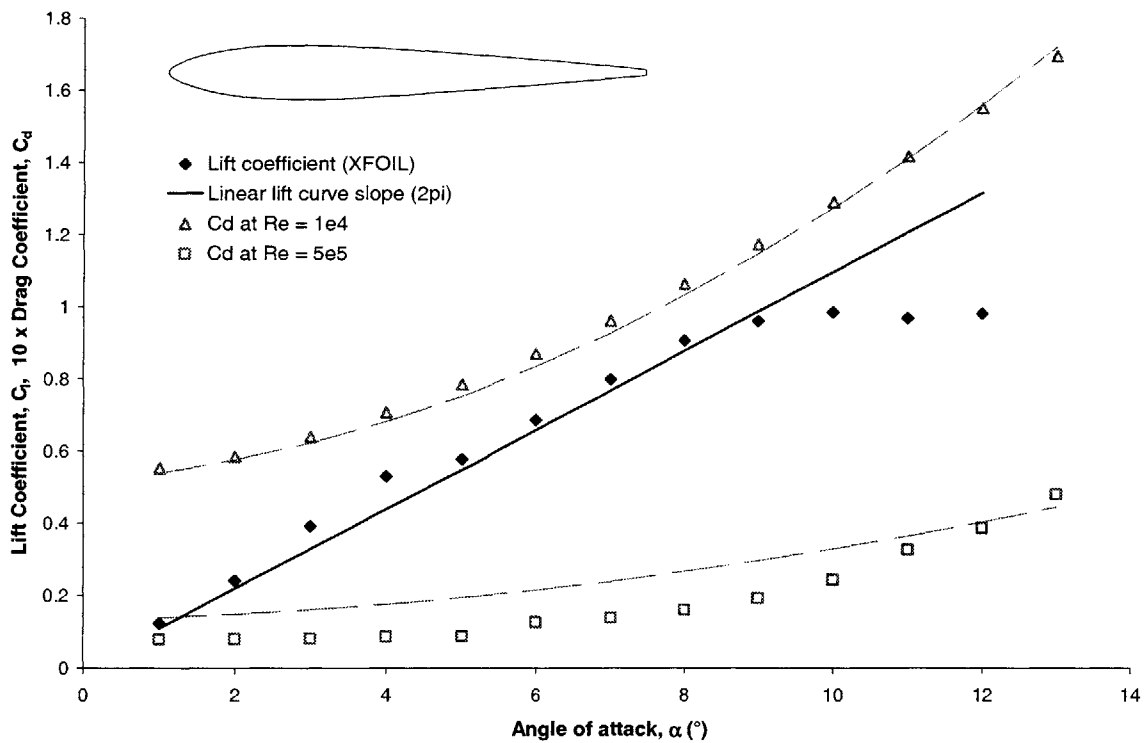


Figure 4.3 NHP Tail rotor blade sectional lift and drag coefficient.

A linear lift curve with slope $C_{l_\alpha} = 2\pi$ was used to approximate the airfoil lift coefficient. A higher fidelity model incorporating the airfoil stall characteristics could be used in future versions if unreasonable angles of attack are seen.

The drag coefficient for an airfoil is often defined by a second degree Taylor series such as $C_d = 0.0087 - 0.0216\alpha + 0.400\alpha^2$, with negligible compressibility or Reynolds number effects for the case of a hovering helicopter rotor. Reynolds number affects the small blades of the PUAUV and like-sized vehicles, however. The Blasius flat plate skin friction drag approximation considers the effects of Reynolds number on a flat surface. The skin friction drag coefficient for a flat plate with laminar flow is

$$C_f = \frac{1.328}{\sqrt{\text{Re}}}, \quad (4-1)$$

and for turbulent flow is

$$C_f = \frac{0.074}{\text{Re}^{1/5}}. \quad (4-2)$$

For Reynolds numbers in the range of 10^5 at which the PUAUV rotor is running at the 75% span, the skin friction drag coefficient is nearly the same for the laminar and turbulent case. For the flat pitch case one could simply add the Reynolds number dependent skin friction drag coefficient to the helicopter rotor C_d . However, this curve does not reasonably fit the output data from XFOIL. A Reynolds number-dependent drag coefficient was devised in the form

$$C_d = (a + b\alpha + c\alpha^2) \frac{1}{\text{Re}^d}. \quad (4-3)$$

The best fit using the data from XFOIL was found with coefficients $a = 1.25$, $b = 2.76$, $c = 44.8$ and $d = 0.346$. This equation fit is presented in Figure 4.3 by the dashed curves.

The blades are held by nylon tail rotor blade grips driven by Futaba S3102 high torque micro servos. FMA S90 micro servos used in previous tests provided inadequate torque capability. Centripetal loads on the blades were found to flatten them at high speed, and swash plate and pushrod friction combined to require more torque than was available. Without the need for small size, light weight, or high speed, the 51.4 oz-in S3102 servos were mounted within an aluminum machined fixture fastened to the inlet end of the center shaft for testing. One pushrod connects each servo to its respective swashplate and rotor system. The swashplate transfers the actuation from the non-rotating frame of the servos, to the rotating frame of the rotors and blades. The inlet rotor can be reached directly, but the second rotor pushrod slides within the center shaft (see Figure 4.4).

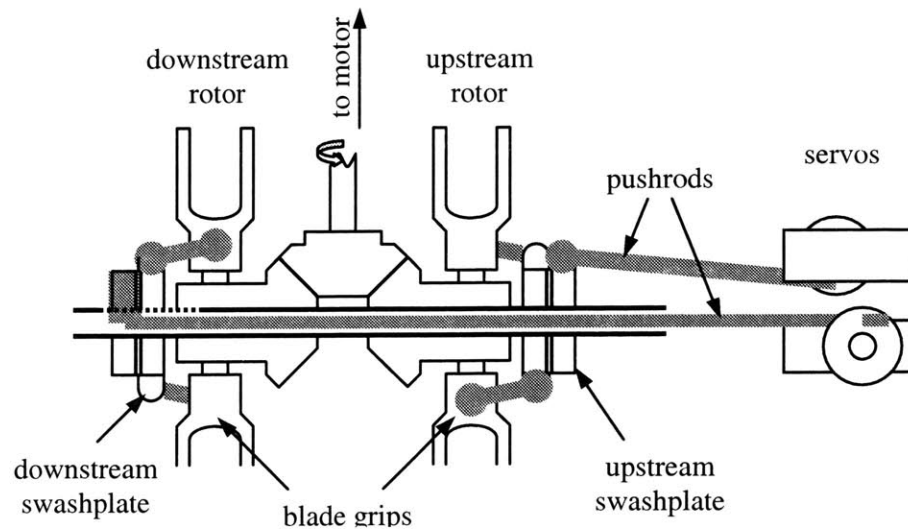


Figure 4.4 Rotor collective control diagram.

4.1.2 Test Motor

Previous vehicle tests were accomplished using the O.S. .32 SX-H helicopter engine and .25 FX airplane engine. Controlled indoor tests required cumbersome exhaust handling, and the noise, fuel spatter and vibration of the engine made testing difficult. Throttle control was also problematic, and torque measurement during thrust production would have required a complex strain gauge and commutator apparatus. Available engines were also limited to a narrow speed and torque envelope. For these reasons, an electric motor was chosen as superior for initial testing, with flight engine sizing to follow test data analysis.

Vehicle tests of the preliminary prototype were accomplished using an Aveox 1409/4Y 4-wind brushless electric motor. This rather small motor was capable of high speeds, but was limited in its ability to output the power and low-end torque needed for a broad test envelope. The motor was designed for use in model airplanes where cooling air would provide heat dissipation. Early hover tests with the Aveox motor caused the motor temperature to become alarmingly high. Continuous operation would therefore be restricted to much lower loads than were required for a reasonable test matrix.

A custom Inertial Motors Corp. servomotor was obtained, with the capacity for high torque output, yet limited to lower speeds than the Aveox motor (see Appendix A). The heat dissipation capacity of the IMC motor without external cooling allows practically indefinite use at moderate to high torque loads. Figure 4.5 graphically illustrates the expected torque required and that available from the Aveox 1409/4Y and Inertial Motors Corp. DC Motor. The Aveox 1409 motor data presented in the graph are based on a 50

percent load limit. This was chosen as a practical maximum in consideration of the weak heat dissipation capabilities of the motor and the poor airflow expected in the test vehicle.

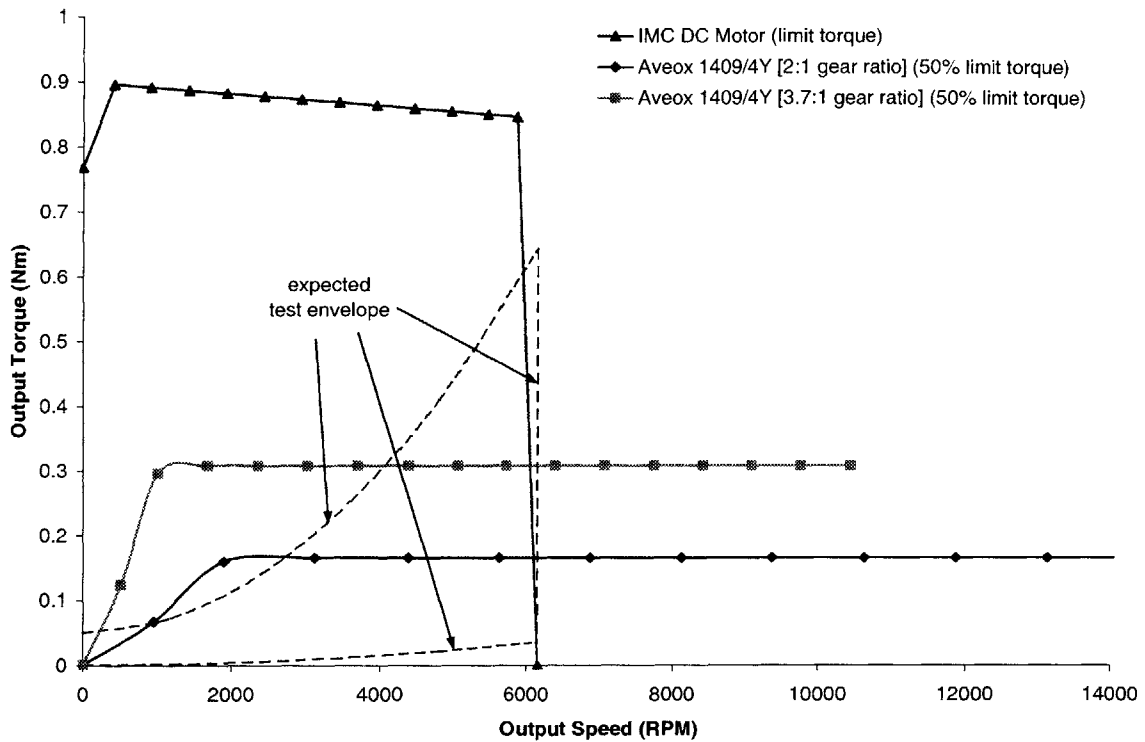


Figure 4.5 RPM vs. torque available and required.

According to analytic power estimates, the torque available from the IMC motor is greater than that absorbed by the vehicle for all proposed tests (dotted curve of Figure 4.5). The IMC motor allows a wide testing envelope, the results of which will be used in sizing a flight vehicle power source. A higher speed would have been desirable, but the practical limit of 6000 RPM is satisfactory.

The IMC motor contains an optical position encoder that provides high fidelity motor speed information. The 500-pulse/revolution square wave output signal can be viewed on an oscilloscope, which in turn provides frequency in kilohertz.

$$f_{kHz} \left(\frac{1000 \text{ pulses}}{\text{sec}} \right) \times \left(\frac{1 \text{ rev}}{500 \text{ pulses}} \right) \times \left(\frac{60 \text{ sec}}{1 \text{ min}} \right) = \left(\frac{\text{rev}}{\text{min}} \right) = \text{RPM} \quad (4-4)$$

The torque and power provided by the motor can be calculated using rotational speed, input voltage, and current data. This negates any need for an external torque sensing capability and also serves to crosscheck speed measurements provided by the optical encoder.

The speed of the motor can be found in terms of the current I , voltage V , motor armature resistance R_a , and speed constant K_v .

$$\text{RPM} = \left(\frac{V - (I \cdot R_a)}{K_v} \right) \quad (4-5)$$

Note that the armature resistance causes a voltage drop when current is applied.

The output torque can be found with input voltage, current and motor RPM.

$$\tau_{out} = (I - i_{NL})K_\tau - K_d \cdot \text{RPM} \quad (4-6)$$

In this case, the no-load current, i_{NL} , reduces the available current, the balance of which is then multiplied by the torque constant K_τ . The second term refers to speed dependent viscous damping of the motor, where K_d is the viscous damping torque constant. The motor constants noted above can be obtained from the manufacturer. Calibration curves were generated for the motor to validate these specifications, which are presented in Section 5.2.1.

4.2 Duct Construction

The duct itself yields much of the performance gain of the expected ducted vehicle layout. As covered in Section 3.1.2, air recirculation at the blade tips leads to loss of

thrust and efficiency. This is especially important in a high disk loaded vehicle such as the PUAUV or any other small VTOL aerial vehicle with a high thrust coefficient. The purpose of a duct is the reduction of tip vortices. To accomplish this, the tip gap must be very small, on the order of 0.5% gap size to diameter. In the case of the PUAUV, 0.5 mm was a reasonable goal, a gap to diameter ratio of 0.22%. The inner surface of the duct must also be smooth, as surface roughness leads to skin friction drag and waviness can produce flow separation.

Beyond its aerodynamic function, the duct contains and retains most of the vehicle components. Although the motor and driveline are mechanically fastened with screws, bending strain of the secondary drive spars due to vibration of the rotors allow the rotors to contact the duct. Axially placed carbon fiber struts impart stiffness in this dimension, and provide a rigid link between the central driveline components and the duct. The driveline was also stabilized by a 0.25-inch thick aluminum plate bonded within a cavity extruded into the outer face of the duct. The plate was sandwiched between the duct and the motor mount to act as a motor mount interface, with metal-to-metal contact on both faces.

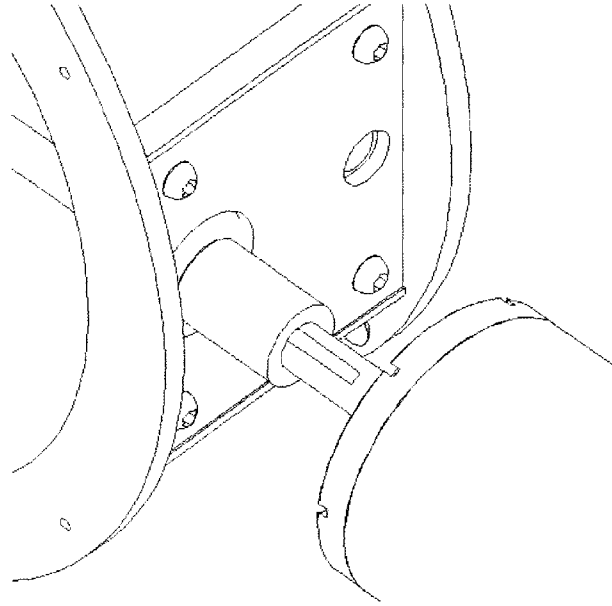


Figure 4.6 Duct/drive train interface.

The duct is composed of three sections; the inner structural housing, the exit diffuser, and the inlet. The inner section is made of ABS plastic using the Fusion Deposition Modeling (FDM) prototyping method. The inner diameter is a constant 220 mm (8.7 inches) and the length is 102 mm (4 inches). Twenty-five millimeter (1-inch) wide flanges adorn each end, with holes to allow mounting of various inlets and diffusers. This flexible design also allows the straightforward incorporation of new inlets, diffusers and constant diameter lengthening plugs for future investigations.

4.2.1 Inlets

Smooth rounded inlets allow air to enter a duct with minimal separation. At the extreme, a sharp-lipped inlet causes the air to separate into a vena contracta, while an excessively large radius inlet suffers from skin friction drag.

Like the inner duct section, the test inlets are made of ABS using FDM. Their complex curvatures are well suited to the method. Three sizes were chosen for testing, of which one was further modified to examine the effects of inlet surface area on thrust augmentation. This latter *flanged* inlet was constructed by attaching a thin ring-shaped sheet of G-10 composite to the interface. It was bonded to the face of the ABS inlet with minimal surface variation, which could have caused turbulence or separation losses.

The smallest inlet tested, theoretically expected to yield the poorest performance (see Figure 3.8), has a lip radius of approximately 4 mm (0.125 in.). The ratio of lip radius to inlet diameter is 0.014. This was the hover inlet radius on all previous flight vehicle prototypes. The second inlet has a lip radius of curvature of 13 mm (0.5 in), yielding a ratio of 0.057. A flanged test inlet has the same 13 mm lip radius, but has bonded to its face a 25 mm (1 inch) wide flange (see Figure 4.7). Tests comparing operation with and without the flange verified expectations that a small amount of thrust is produced by high velocity inflow air passing over the flange, creating low pressure on its face.

The largest test inlet has a 25.4 mm (1 inch) radius of curvature, yielding a rather large lip radius to inlet diameter ratio of 0.114. This was the baseline inlet with which the various diffusers were tested. It is believed that this large radius is least affected by separation, and will thus result in the most pure diffuser effects results.

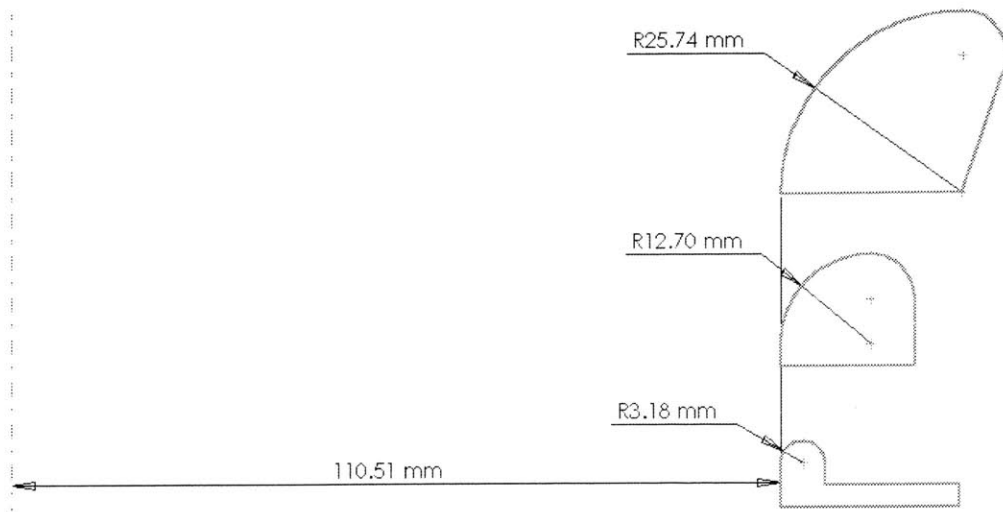


Figure 4.7 Section diagrams of four test inlets.

4.2.2 Exit Diffusers

The purpose of a diffuser is to reduce the exit velocity, which should yield improved thrust efficiency at a slight cost to thrust for a given collective pitch setting. Section 3.1.3 analyzes the theoretical performance gain for a given diffusion, σ_{duct} . However, obtaining a large diffusion is difficult. Reverse flow, diffuser flow separation, blade wake turbulence and skin friction drag can all undermine the theoretical gains.

Three diffuser angles have been chosen to examine the actual diffusion and performance for a given diffuser arrangement. The dimensional diffusion parameter, σ_d is the ratio of diffuser exit area to inlet area. It should be noted that the actual flow diffusion ratio is not necessarily equal to the physical diffuser exit area to inlet area ratio, σ_d , and in most cases is far less.

Table 4.1 Diffuser dimensions (see Figure 4.8).

	Inlet Radius (mm / in)	Exit Radius (mm / in)	Length (mm / in)	R_{curve} (mm / in)	σ_d
Small	220 / 8.7	223 / 8.75	190 / 7.5	-	1.03
Medium	220 / 8.7	260 / 10.25	190 / 7.5	120 / 4.7	1.40
Large	220 / 8.7	297 / 11.7	190 / 7.5	100 / 4.0	1.82

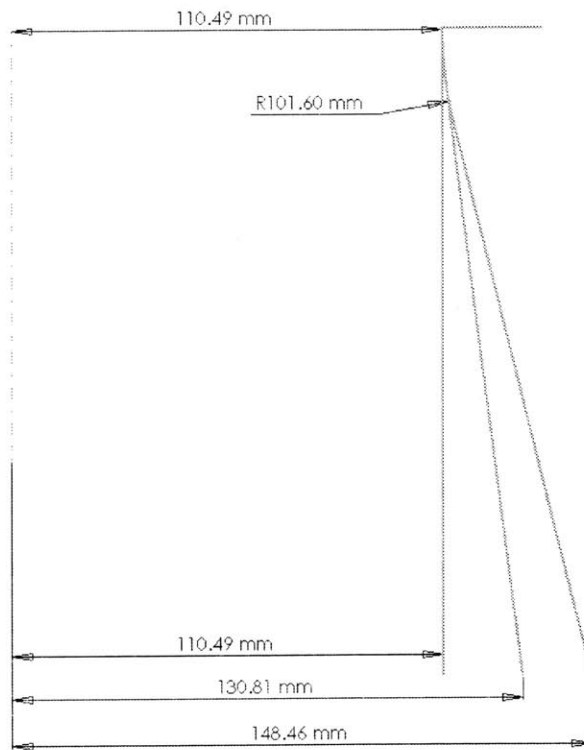


Figure 4.8 Diagram of three test diffusers.

Blue polystyrene foam board was used to construct the diffusers. Each diffuser was built from three portions of 4½-inch thick foam board, joined with epoxy to form a three sided, open top, open bottom box. Composite G-10 sheets were then cut into circular disks with dimensions corresponding to the desired internal and external diameter of each diffuser. One pair of templates was then attached to the foam box so that they were centered along an axis normal to the top and bottom face. An aluminum and plastic bow holding a Nichrome hot wire was then used to cut excess foam using the templates as guides. A divergent hollow cylinder was the end product of this process.

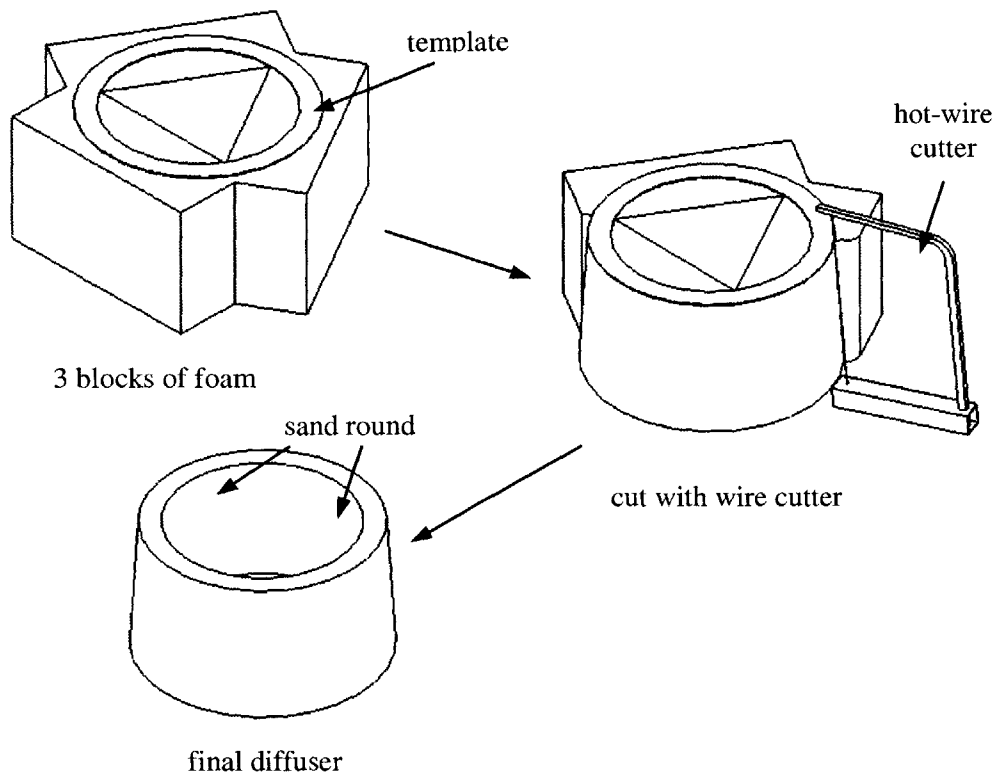


Figure 4.9 Construction of a diffuser.

Hand sanding with a cylindrical sanding block was used to remove the excess foam at the inlet end, so that the transition from the constant diameter duct to the divergent diffuser is gradual. Sanding and filling with plaster hobby filler followed to arrive at a smooth inner surface. Each of the three duct diffusers was created in this manner.

4.3 Data Acquisition

4.3.1 Hardware

The load cell used for this test series is a 3-axis JR3 20E12 force and moment sensor. It was attached to a floor-mounted pedestal for testing. The test vehicle was mounted to the sensor via a mounting bracket such that the duct and the motor axes were normal to the floor. The test vehicle center of mass was located approximately over the center of the

50 mm (2 inch) diameter, 32 mm (1.25 inch) tall puck-shaped sensor. The duct was mounted so that duct thrust is sensed in the positive x-axis direction of the sensor, and due to the off-axis mounting of the duct the moment about the vertical z-axis can be cross checked to verify vehicle thrust (see Figure 4.10 below).

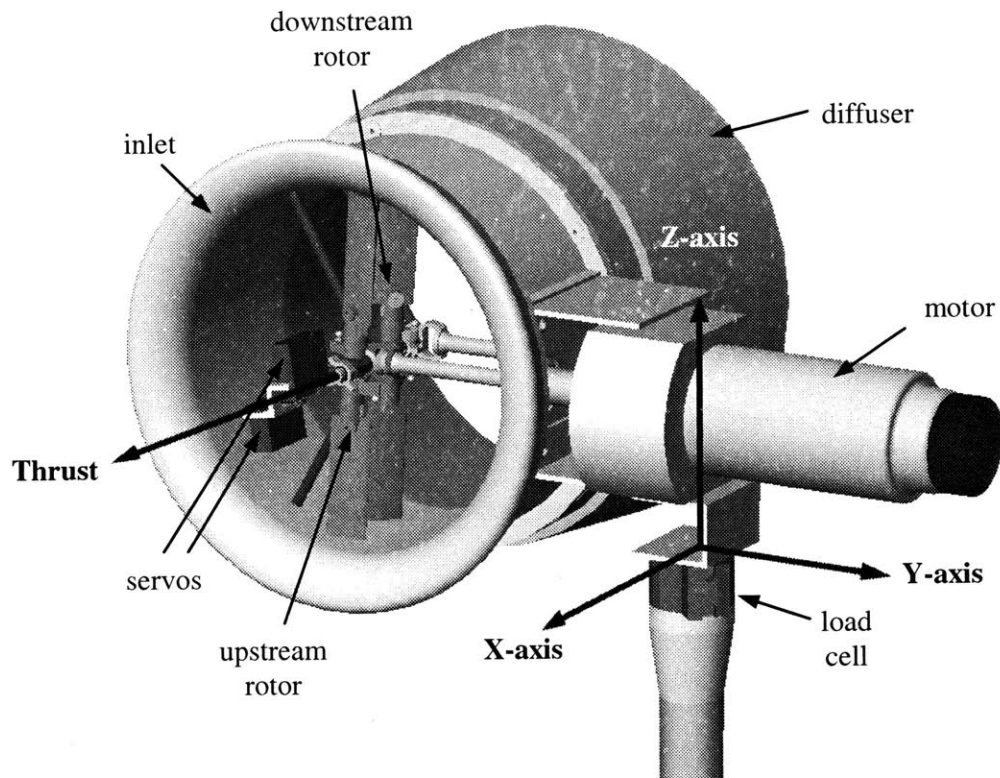


Figure 4.10 PUAV hover thrust test apparatus..

The load cell can be adjusted to a full scale rating of either 3 or 15 lbs. With a test vehicle gross weight of approximately 12 lbs, the higher scale 15 lb setting is necessary. Data were taken via a National Instruments DAQCard-6062E analog-to-digital (A/D) card connected to a laptop computer. The software used for these tests is covered in the next section.

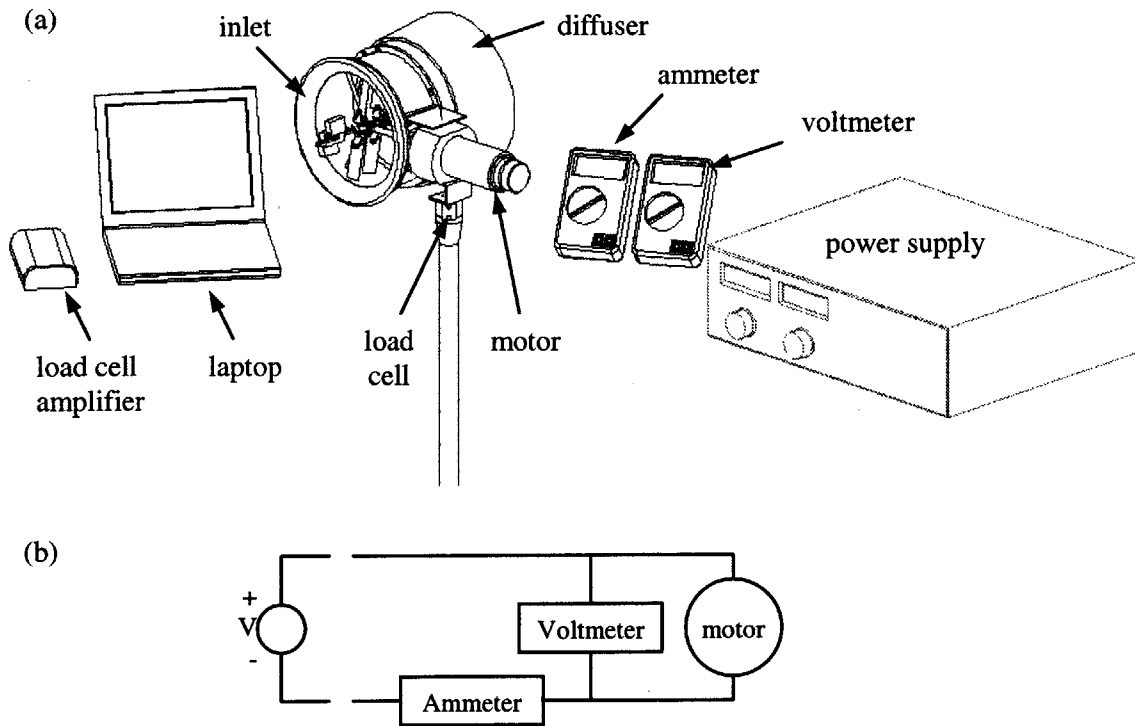


Figure 4.11 Mechanical (a), and electrical (b) test apparatus layout.

The motor is rated to a maximum speed of 7730 RPM but can only reach approximately 6000 RPM at the maximum power supply voltage of 60 V. Electrical power was provided by a BK Precision High Current DC regulated power supply. Voltage was measured across the power leads close to the motor to reduce the effects of wire losses, and current was measured between the power supply and the motor (see Figure 4.11 (b)). Motor speed was measured via a 5 V supplied optical encoder that is part of the motor. The output was fed to an oscilloscope that displays the frequency.

Wake surveys provide insight into the induced flow and thrust performance of the duct and diffuser. To measure the air velocity, a pitot/static probe and pressure gauge were used to measure the total head and local pressure.

The wake velocity can be calculated using Bernoulli's equation,

$$\begin{aligned} H &= p_{wake} + \frac{1}{2} \rho_{air} V_{wake}^2 = p_{atm} \\ &= p_{wake} + q. \end{aligned} \quad (4-7)$$

Here we see that total head, H of the finite velocity wake is equal to the static atmospheric pressure. Subtracting the local wake velocity, we find the dynamic pressure

$$q = \frac{1}{2} \rho_{air} V_{wake}^2 = p_{atm} - p_{wake}. \quad (4-8)$$

The Magnahelic 0.5" H₂O pressure gauge used for testing actually displays h_{meas} , the water column height. Archimedes principle equates water column height and dynamic pressure.

$$\rho_{water} g h_{meas} = \frac{1}{2} \rho_{air} V_{wake}^2 = p_{atm} - p_{wake} \quad (4-9) \text{ (a)}$$

$$h_{meas} = \frac{1}{2g} \frac{\rho_{air}}{\rho_{water}} V_{wake}^2 \quad (4-9) \text{ (b)}$$

Rearranging Equation (4-9) yields the velocity in the rotor wake.

$$V_{wake} = \sqrt{\left(2 \frac{\rho_{water}}{\rho_{air}} g h_{meas} \right)} \quad (4-10)$$

4.3.2 Data Acquisition Software

The motor speed, voltage and current data were entered manually into the computer and recorded. The JR3 20E12 load cell was connected to the DAQCard A/D card, where a National Instruments LabVIEW virtual instrument (VI) processed and displayed the data. A test point was taken by selecting an icon in the VI, at which point a preset number of samples were taken and their plot printed to the screen for inspection. The average value over the sample for user-defined parameters can also be displayed to the screen.

During PUAUV tests, the VI was set to take 3000 samples for each point, at 700 samples per second. A data file was produced for each test point, which gave the time sequence, while a second short log file was made for a given sequence of points. The log file contained averaged data for each user-defined channel, and was the source of information for analysis.

In the case of PUAUV duct testing, each test run would entail data gathering for a given duct configuration. For example, the 0.5-inch radius inlet paired with the medium angle diffuser could be run at a number of speeds and collective settings. Such a test run may output a log file containing 100 lines of data from all the combinations of five collective settings for each of two rotors at four speeds. Changing the inlet would involve running another 100 points at the same test settings.

[THIS PAGE INTENTIONALLY LEFT BLANK]

Chapter 5: Data Collection and Analysis

5.1 Test Matrix Design

A blind test matrix encompassing all possible combinations would have been time consuming and unnecessary. After exploring the approximate effects of different parameters, a condensed test matrix was devised. When comparing input and output pairings no radical behavior was noted. There did not appear to be significant performance coupling between the variables tested, therefore testing complete permutations of all variables in all combinations was not warranted.

Initial tests of differential collective, inlet effects and diffuser effects were limited to 4800 RPM. This limitation was enacted due to concerns that a damaged test vehicle could not be quickly repaired or replaced. It was also believed that the overall behavior of the inlet, duct, diffuser and drive train could be ascertained at the slower speed. Once sufficient data were gathered, the envelope was expanded to include the 6000-RPM maximum speed test points.

Variables Tested

- *Inlet radius – small, medium, large*
- *Inlet area – normal, flanged*
- *Diffuser Ratio – small, medium, large*
- *Collective Angle (single and both rotors) – (0-35°)*
- *RPM – (0-6000 RPM)*
- *Individual Rotors – upper and lower*
- *Blade tip gap*
- *Ground Effect*

Quantities Recorded

- *Thrust*
- *Motor RPM*
- *Voltage*
- *Current*

Table 5.1 Test matrix.

Test	Inlet	Diffuser	Notes
Speed: 1200, 1800, 2400, 3600, 4800, 6000 RPM Collective: 0, 10, 20, 25, 30, 35° (both rotors)			
Differential collective	Large (1" lip radius)	Medium ($\sigma = 1.37$)	Vary collective independently.
Inlet	Small (0.125" lip radius) Medium (0.5" lip radius) Medium (0.5" lip w/ 1" flange) Large (1" lip radius)	Medium ($\sigma = 1.37$)	
Diffuser	Large (1" lip radius)	Small ($\sigma = 1.0$) Medium ($\sigma = 1.37$) Large ($\sigma = 1.65$)	
Upstream rotor	Large (1" lip radius)	Medium ($\sigma = 1.37$)	
Downstream rotor	Large (1" lip radius)	Medium ($\sigma = 1.37$)	Compare power for second rotor with 0.5 mm and 1 mm tip gap.
Downstream rotor (large tip gap)	Large (1" lip radius)	Medium ($\sigma = 1.37$)	
Speed: 1800, 3600 RPM Collective: 35° both single and dual rotor			
Wake survey	Large (1" lip radius)	Small ($\sigma = 1.0$) Medium ($\sigma = 1.37$) Large ($\sigma = 1.65$)	Pitot probe survey of wake flow.
Speed: 6000 RPM Collective: 35° single rotor			
Ground effect	Large (1" lip radius)	Medium ($\sigma = 1.37$)	3 foot square surface moved axial to duct.

5.2 Calibration

5.2.1 Motor Calibration

The IMC DC motor constants and ratings were available at the time of testing. However, because the motor is quite old, several calibration runs were performed to find the calibrated motor constants. No-load and loaded tests were performed. Unloaded tests entailed running the motor at speeds covering the motor speed envelope and especially the higher speeds that would be used for PUAUV testing. The motor shaft was unconstrained during this test.

The generator constant, or speed constant, K_V is simply the slope of the curve of voltage and speed. Thus K_V is the average quotient of voltage divided by speed for the motor.

$$K_V = \frac{\dot{f}_{RPM}}{\dot{V}} = 100.9 \frac{RPM}{V} \quad (5-1)$$

The torque constant K_τ is found by equating the mechanical power output by the motor to the input electrical power. This becomes $K_\tau = 1/K_V$, when K_V is defined in terms of $f(rad/sec)/V$ and K_τ is in units of Nm/A . Because we have defined the speed constant in terms of RPM, a conversion factor must be introduced. Thus

$$K_\tau = \frac{9.549}{K_V} = 0.0946 \frac{Nm}{A} \quad (5-2)$$

In the no-load case we know that the output torque is zero. Thus, all current entering the motor must be dissipated by the motor. Using K_τ , voltage and current, we can find the effective torque being consumed by the motor.

$$\tau_{out} + \tau_{lost} = I \cdot K_\tau (= \tau_{lost} \text{ when } \tau_{out} = 0) \quad (5-3)$$

The lost torque, τ_{lost} , is composed of a state term (called the no-load current) and a viscous term that changes as a function of RPM. These two sources reduce the effective output torque of the motor.

To widen the torque and current envelope, loaded tests were performed as well. A Prony brake, as illustrated in Figure 5.1 was used. The tension in the line T , measured by a scale (where $T = T_2 - T_1$), multiplied by the radius of the pulley r_p , yields the torque absorbed, τ_{out} , from Equation (5-3). A heavier weight applies more frictional force to the pulley, causing the torque and line tension to increase.

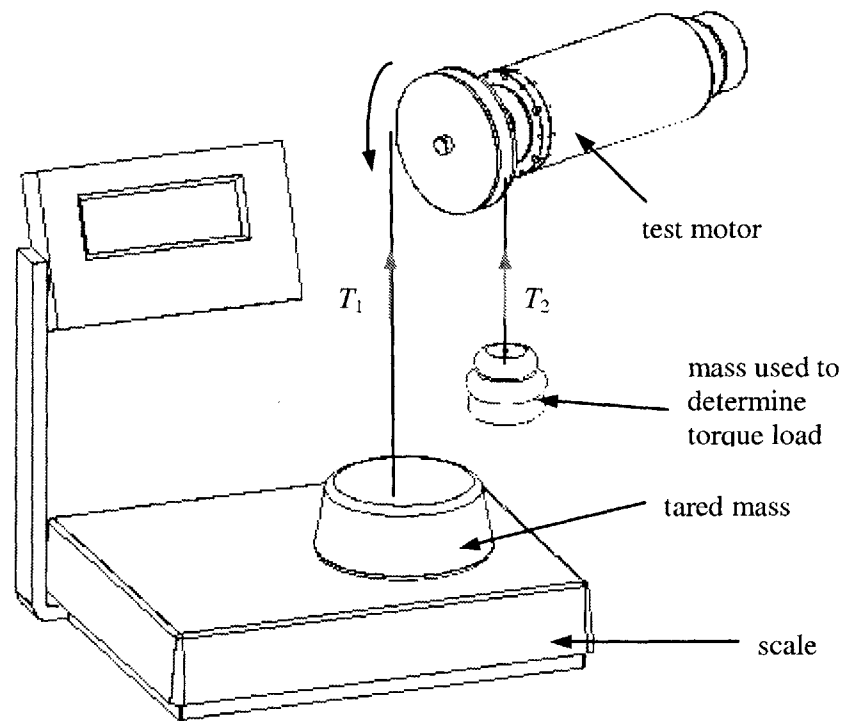


Figure 5.1 Motor test stand and Prony brake.

The slope of the torque vs. speed curve is the viscous torque constant K_d ,

$$K_d = \frac{\tau_{lost}}{f_{RPM}} = 9.06 \cdot 10^{-6} \frac{Nm}{RPM} \quad (5-4)$$

while the zero speed intercept of the curve of τ_{lost} vs. f_{RPM} is the static friction, τ_{static} .

Reversing Equation (5-3), one can find the no-load current required to overcome static friction within the motor.

$$i_{NL} = \frac{\tau_{static}}{K_T} = 0.498A \quad (5-5)$$

To obtain the armature resistance, R_a , requires that stall tests be performed. The output shaft is held fixed while the voltage is increased. The load causes greater current to be drawn and power is lost in the form of heat dissipation. The armature resistance is thus the quotient of voltage over current

$$R_a = \frac{V}{I} = 0.580\Omega . \quad (5-6)$$

Ultimately, the torque and power of interest is that delivered to the rotors. Thus, the above tests were also run with the driveline installed to determine the losses of the driveline. The test procedure is the same as for the motor alone. The armature resistance, and speed and torque constants are unaffected by the drivetrain loads external to the motor, though the loads manifest themselves through these constants in the form of losses. The viscous torque constant, $K_{d_{total}} = K_{d_{motor}} + K_{d_{driveline}}$ now accounts for the torque lost to the driveline components in addition to the motor losses, as a function of speed. The no-load current, i_{NL} similarly accounts for the current induced by static friction from the motor and driveline gears and bearings, where $i_{NL_{total}} = i_{NL_{motor}} + i_{NL_{driveline}}$.

Table 5.2 Motor and driveline data.

	Motor (listed)	Motor (measured)	Motor and Driveline (measured)
Speed Constant, K_V	97.1 RPM/V	100.9 RPM/V	100.9 RPM/V
Torque Constant, K_T	0.0988 Nm/A	0.0946 Nm/A	0.0946 Nm/A
Armature Resistance, R_a	0.4 Ω	0.580 Ω	0.580 Ω
No-load Current, i_{NL}	0.429 A	0.498 A	0.546 A
Viscous Damp. Coeff., K_d	1.91E-5 Nm/RPM	9.06E-6 Nm/RPM	1.22E-5 Nm/RPM

The calibrated rotor + driveline constants do not explicitly account for dependence of torque on gear losses. Although the bearings within the driveline, like the bearings and bushings in the motor are generally independent of torque, the gear losses of the driveline are not. Tests that yield the no-load current and viscous losses only consider speed, and not torque. As the rotor blades are moved to higher angles of attack, the torque they absorb from the motor increases, causing the gear losses within the driveline to increase. Unfortunately, the driveline output shaft is not amenable to Prony brake torque testing. Without values for τ_{out} , it is impossible to experimentally determine τ_{lost} for the full motor + driveline apparatus. An analytic model may account for the losses but cannot be validated by data. It should be noted that static and viscous friction losses due to the motor and driveline at no load are small in comparison to electrical losses within the motor. Whether this is also the case at higher driveline torque cannot be confirmed.

5.2.2 Servo Calibration

Servos provide a rotary output that translates to linear motion of the pushrod and swash plate, which is then transferred back to rotational position of the blade grip. Blade position calibration was performed using the computer data acquisition and servo driving software covered in Section 4.3.1 and 4.3.2. This was performed with a servo sweep in both directions to account for linkage slop and backlash. The calibration yielded a nearly

linear set of correlated points between 0 and 35° blade angle, with a slight hysteresis (see Figure 5.2).

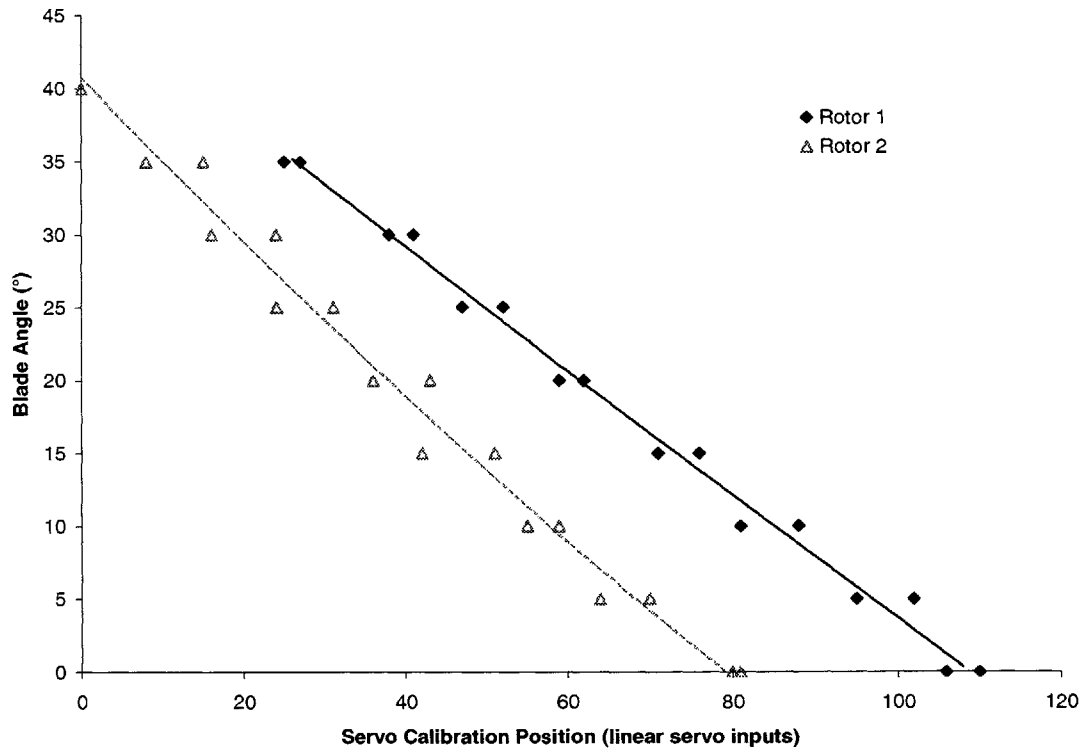


Figure 5.2 Servo calibration curves.

Backlash is less than $\pm 2^\circ$ for the first rotor and no more than $\pm 3^\circ$ for the second rotor. The longer and more complex linkage required for the second rotor provides a small amount of extra flex, as well as more friction.

5.2.3 Differential Collective

The benefits of coaxial propulsion are wasted if the load is not properly shared between the two rotors. Although the servo calibration procedure ensured that the blade angles were known and could be equalized, this would not guarantee that the equal blade angle position would provide equal angle of attack or disk loading.

Three differential collective tests were performed at two speeds each. In each test a collective angle was chosen, and each rotor was positioned an equal and opposite angle from that point. In the first test, the center point was set as 20° and the increment was 4° with a range of ±10°. In the second test the center point was set at 30°. The final test was centered at 25° and covered a range of ±5° in 2° increments.

Table 5.3 Differential collective calibration test.

Test 1		Test 2		Test 3	
<i>Collective 1</i>	<i>Collective 2</i>	<i>Collective 1</i>	<i>Collective 2</i>	<i>Collective 1</i>	<i>Collective 2</i>
10°	30°	20°	40°	20°	30°
14°	26°	24°	36°	22°	28°
18°	22°	28°	32°	24°	26°
22°	18°	32°	28°	26°	24°
26°	14°	36°	24°	28°	22°
30°	10°	40°	20°	30°	20°

Results were mixed. The 25±5° results for both test speeds show a flat behavior that indicates that thrust is unaffected by rotors that are at unequal collective angles. The four other test runs indicate that the efficiency is diminished when the collective angles are widely separated. Performance is greatest when the difference between the first and second rotor is approximately 3°, or the first rotor blade angle is 3° greater than the second (see Figure 5.3).

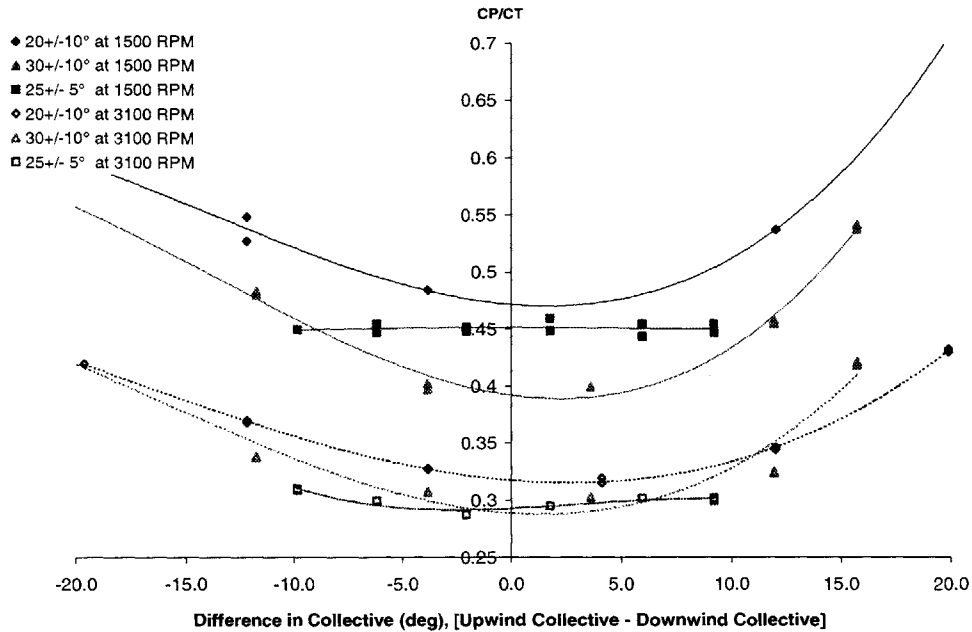


Figure 5.3 Differential Collective calibration test results.

Due to a backlash of $\pm 2\text{-}3^\circ$ in each collective mechanism, this difference may be attributed simply to play in the pushrod linkage. The drag-induced swirl in the wake of the first rotor also tends to decrease the inflow angle of the second rotor, reducing the blade angle $1\text{-}2^\circ$ for a given angle of attack.

Although the differential collective calibration test indicates a slight performance benefit with offset collective angles, the offset is small and the performance impact is negligible. For this reason and to simplify test procedures, further testing was accomplished with equal commanded collective settings for the two rotors.

5.3 Experimental Results

5.3.1 Inlet Size

Once calibrations were completed, inlet tests were performed. With a medium diffuser attached to the rear flange of the duct inner section, three inlets were sequentially tested. The small inlet has a constant lip radius of 3.2mm (0.125 inches), the medium inlet has a lip radius of 12.7mm (0.5 inches), and the large inlet has an inlet lip radius of curvature of 1 inch (see Section 4.2.1). All three inlets have the same throat area.

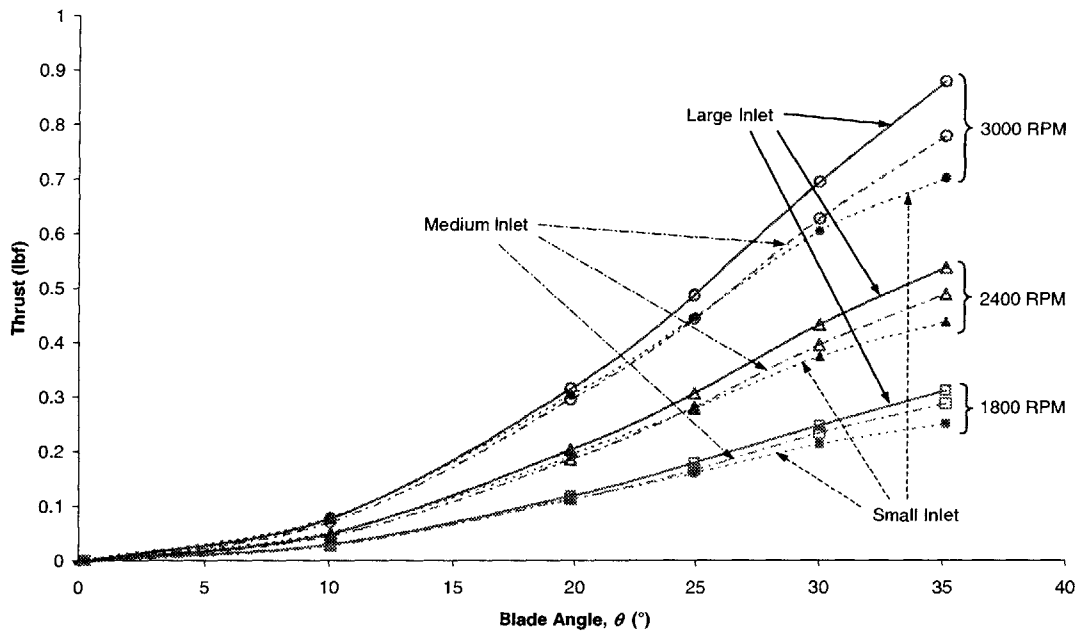


Figure 5.4 Thrust as a function of blade angle for three inlet sizes (medium diffuser, $\sigma_{duct} = 1.37$)

The thrust plot (Figure 5.4) shows an increase in thrust with increased blade angle and speed. The greatest thrust is obtained with the large inlet, with the medium and small inlets providing approximately 10 and 15 percent less thrust, respectively. The high thrust performance obtained by the large inlet is likely due in part to the gradual inlet

radius of curvature, which reduces losses due to separation, and the rather large size of the inlet surface area, which increases suction thrust on the inlet.

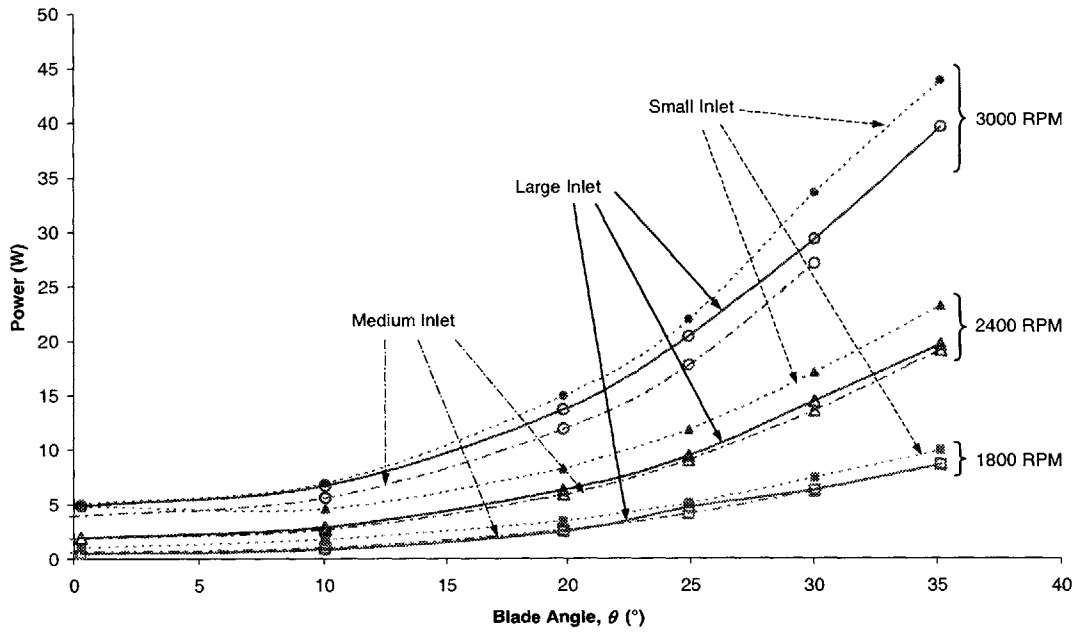


Figure 5.5 Power as a function of blade angle for three inlet sizes (medium diffuser, $\sigma_{duct} = 1.37$)

The curve of power consumed as a function of blade angle shows a slightly different trend from the thrust plot. In Figure 5.5, the least power is consumed when the medium inlet is used, slightly offsetting the performance gain shown in the thrust plot. The small inlet again appears to provide the worst performance. A better overall comparison of performance is provided by a comparison of power over thrust, or power coefficient divided by thrust coefficient.

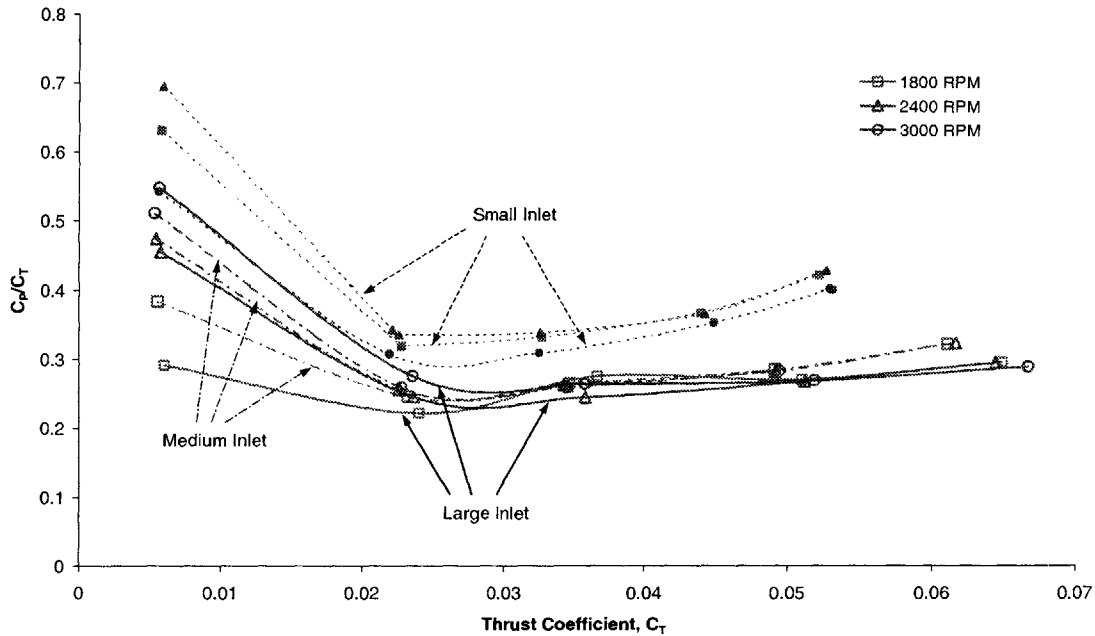


Figure 5.6 Power coefficient divided by thrust coefficient as a function of thrust coefficient for three inlet sizes (medium diffuser, $\sigma_{duct} = 1.37$).

Figure 5.6 clearly illustrates the poor efficiency of the small radius inlet. The large inlet shows slightly better performance than the medium inlet, though the effect of speed on C_p/C_T is greater than the effect of inlet size. Section 5.4.1 provides further analysis of the inlet performance and compares it with numerical model predictions.

5.3.2 Diffuser Angle

Diffuser tests were all performed with the large, 25.4-mm (1-inch) radius inlet. Three diffusers were compared, with physical diffusion ratios, σ_{duct} of 1.0, 1.37 and 1.65. It should be reiterated that these area ratios define the physical dimension ratio of the duct diffuser exit area to rotor disk area, and not the ratio of wake flow area to rotor disk area.

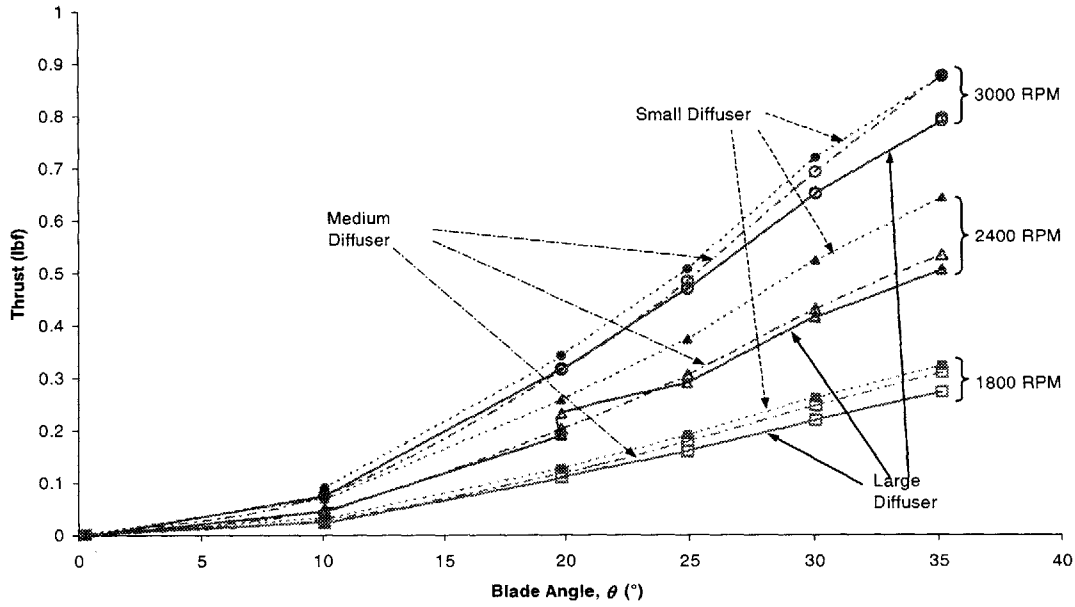


Figure 5.7 Thrust as a function of blade angle for three diffusers (large inlet, $r_i = 25.4\text{mm}$).

The greatest thrust for a given blade angle and rotational speed occurs with the small diffuser, while the least thrust is obtained when the large diffuser ($\sigma_{duct} = 1.65$) is used.

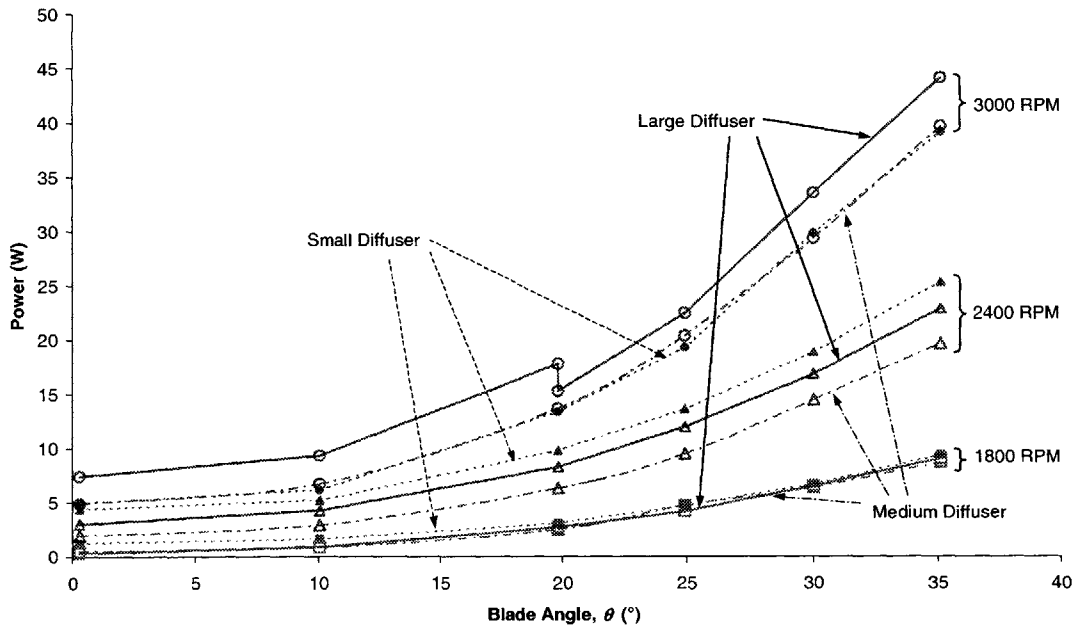


Figure 5.8 Power as a function of blade angle for three diffusers (large inlet, $r_i = 25.4\text{mm}$)

Power consumed at a given blade angle and speed does not follow a clear pattern. At 1800 RPM the diffusion parameter does not appear to drastically affect power consumption, while at 2400 RPM the small diffuser draws the greatest power and the medium diffuser draws the least. At 3000 RPM the large diffuser uses the most power, while the medium and small diffuser both draw about 10 percent less.

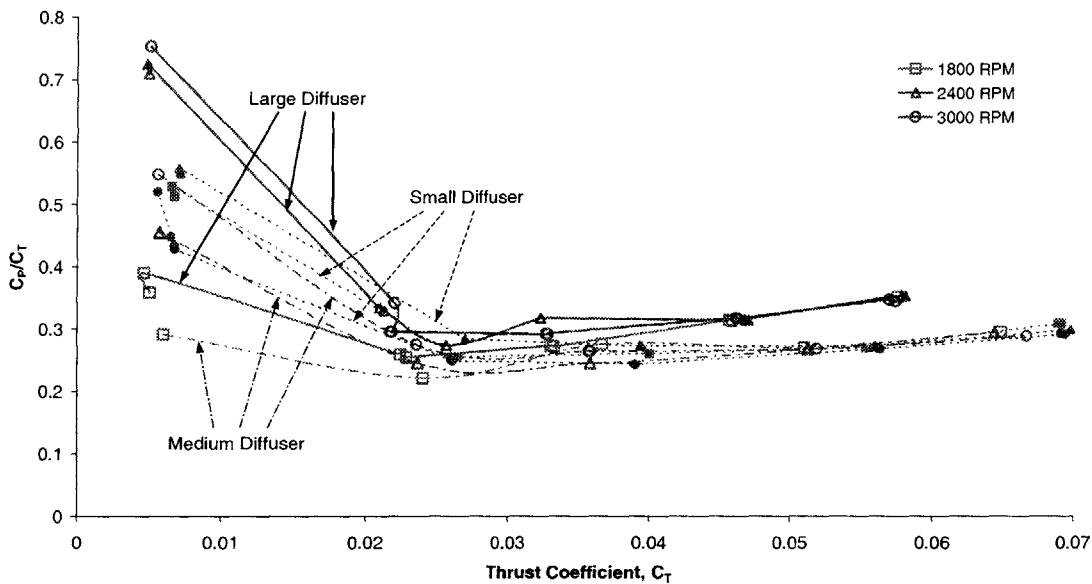


Figure 5.9 Power coefficient divided by thrust coefficient as a function of thrust coefficient for three diffusers (large inlet, $r_i = 25.4\text{mm}$)

When comparing power to thrust in the form of C_p/C_T vs. C_T in Figure 5.9 it is clear that the large diffuser performs poorly at high speed and C_T . However, it yields decent efficiency at low C_T at 1800 RPM. A possible explanation for the performance behavior of different diffuser geometries is that high blade tip induced velocities cause a low-pressure region at the periphery of the induced flow to form. The low pressure draws air outward and along the surface of the diffuser, reducing the wake flow at the core and creating a high-velocity annular wake. This effect is most significant at high speed and high thrust coefficient. The large diffuser may also experience separation as the great

backpressure due to the large area ratio becomes too great. The small and medium diffusers are less affected by separation and a high velocity ring wake losses due to their smaller diffusion angle.

At low speeds and low blade angles the centrifugal flow is benign and the velocity profile is evenly distributed, leading to improved efficiency. The benefit of diffusion is of course greatest with the divergent diffusers, especially the medium diffuser where separation is less likely to occur. The benefit is lost with the small diffuser due to its small exit area and high wake velocity, per Equation (3-76). The wake survey presented in Section 5.3.6 sheds further light on the exit flow behavior.

5.3.3 Number of Rotors

Most VTOL vehicles use either a tail-mounted rotor or stators mounted inside the induced flow field in order to counteract the torque produced by the main thrust-producing rotor. Anti-torque rotors rob power while stators within the flow reduce the efficiency and thrust capabilities of the system. The use of a second contrarotating thrust-producing rotor counteracts the torque of the first, negating any need for auxiliary anti-torque devices. However, the weight and complexity of additional rotors play against the use of a second rotor. Thrust performance is lost due to higher induced power (see Section 3.1.3). Additionally, multiple rotors tend to require narrower chord blades to maintain a given solidity, decreasing Reynolds number and increasing the attendant skin friction drag. A comprehensive trade-off analysis must be used to weigh the merits of either system. For reasons outlined in Section 2.3.2, the PUAUV was designed to be driven by two rotors.

Tests were carried out on three rotor configurations: The upstream rotor only, the downstream rotor only, and both rotors turning in opposite direction to one another.

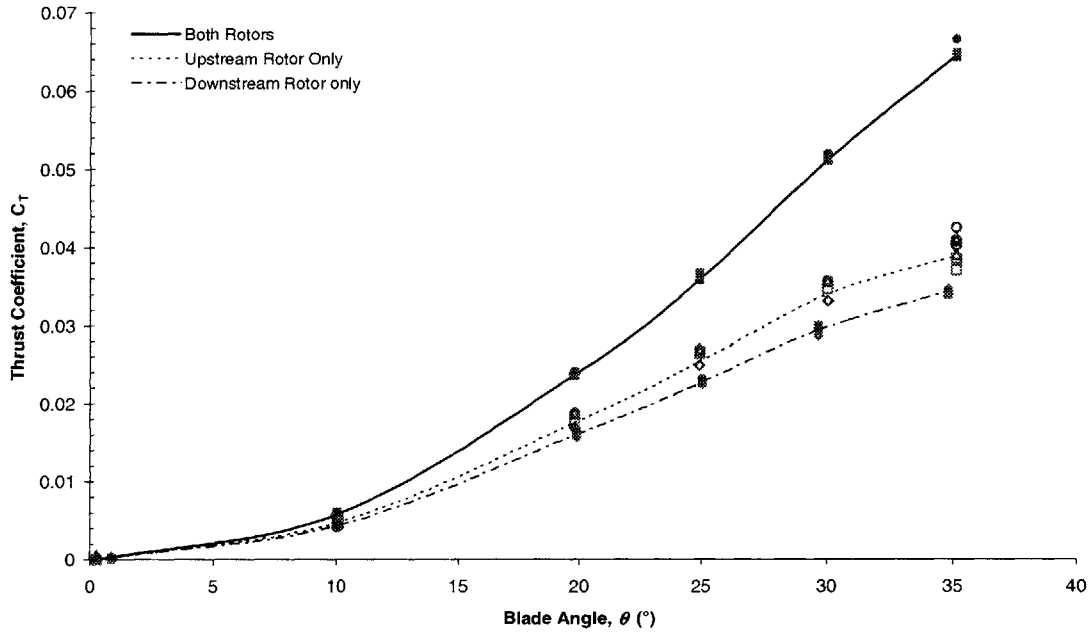


Figure 5.10 Thrust coefficient as a function of blade angle for each individual rotor and both rotors (large inlet, medium diffuser).

The points shown in Figure 5.10 represent multiple tests at various speeds. The three lines represent the average values over the tested speeds. It is clear from the plots that the thrust production of both rotors running together is less than the sum of each individually. The upstream rotor, when tested individually, provides approximately 62 percent of the thrust of both running together, while the downstream rotor provides approximately 57 percent, for a given blade angle.

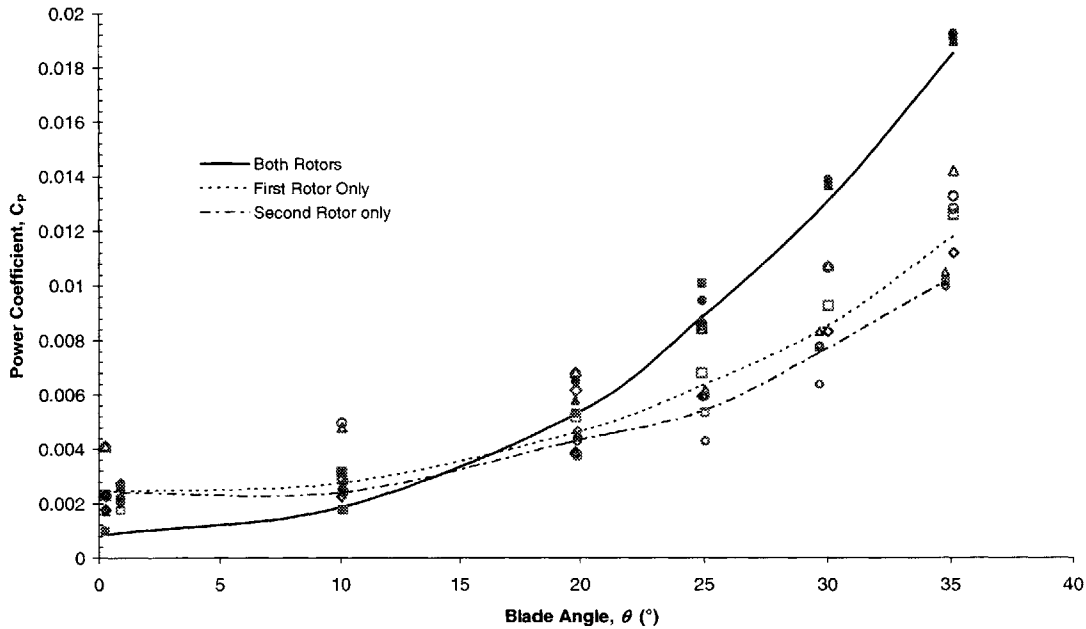


Figure 5.11 Power coefficient as a function of blade angle for each individual rotor and both rotors (large inlet, medium diffuser).

The power coefficient test points show a larger spread than the thrust coefficient results. Oddly, at small blade angles both upstream and downstream rotors consume more power individually than when combined. Asymmetric gear loads on the secondary input gear may cause gear and bearing losses that are reduced when both rotors are running and the torque loads balance the forces acting at the transmission core. A future study of gear train losses should elucidate this peculiarity.

5.3.4 Blade Tip clearance

Though the numerical model constructed for this report does not account for blade tip clearance losses, it is interesting to note the performance difference illustrated below in Figure 5.12 due to a 0.5mm change in tip clearance. The baseline test vehicle maintains

an average tip clearance of 0.5 mm, which is approximately 0.225 percent of the duct diameter.

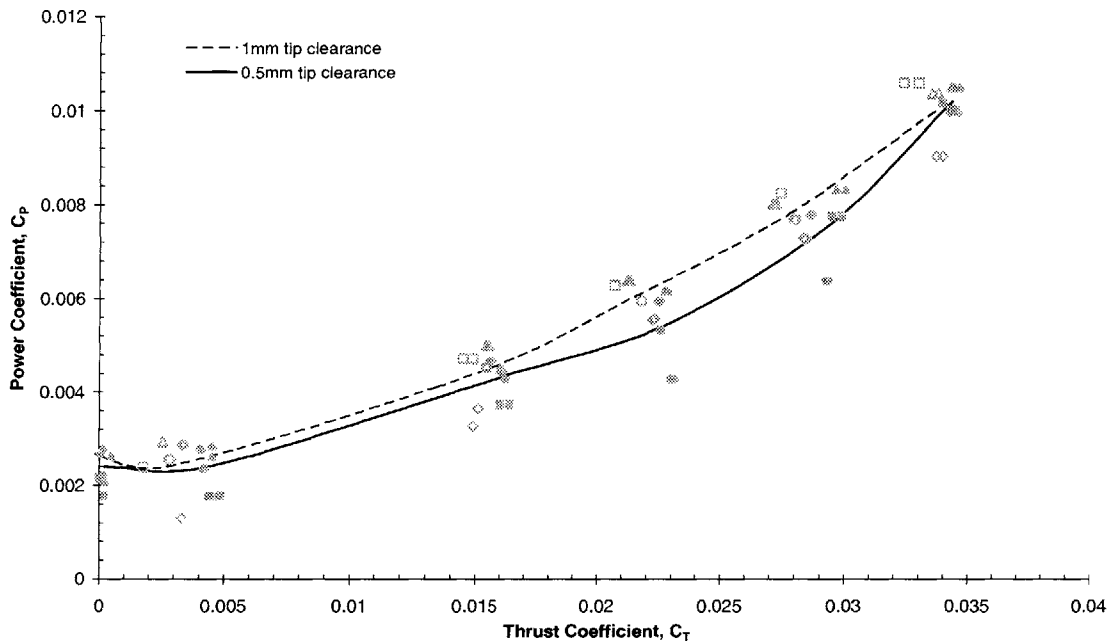


Figure 5.12 Power coefficient as a function of thrust coefficient for a 0.5 and 1 mm blade tip gap (large inlet, medium diffuser).

A comparative test with a 1-mm tip clearance (0.45 percent of D_{duct}) shows a small reduction in performance. Scatter in power coefficient, C_p and thrust coefficient, C_T corresponding to the range of speeds tested indicate that speed has a greater impact on performance than the blade tip gap. This indicates that for a small vehicle like the PUAUV, a small tip gap has a minor effect on hover performance.

5.3.5 Ground Effect

A ground effect test was performed to determine the effect on thrust as a 1-meter square plate was centered in the wake of the PUAUV test vehicle. A large inlet and medium diffuser were used and the single downstream rotor was run at 35 degrees pitch at 6000

RPM. The 'ground' plate was brought from 1.8 meters to 15 cm, thrust and power were noted.

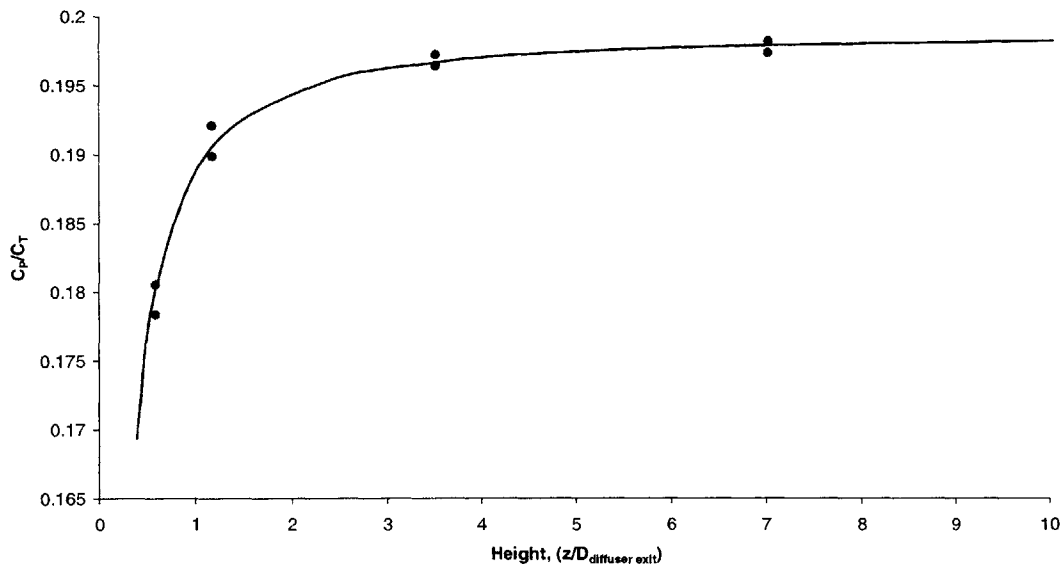


Figure 5.13 C_p/C_T as a function of height.

The power was observed to remain constant over the test run. Thrust increased exponentially as the surface was brought close to the diffuser exit face. A ten percent increase in thrust was measured between the 'out-of-ground effect' case at a distance of 2 m and the 'in-ground effect' case at 15 cm.

5.3.6 Wake Survey

Load cell experimental test results of duct diffusers showed poor correlation with expected behavior. The effect of duct diffusion was counter to model predictions as well as previous experimental results. Thrust efficiency gains were not being seen. A wake survey was therefore performed to gain insight into the reasons behind these shortcomings, and to examine if the physical diffusion was being translated into flow diffusion.

Using the pitot probe and measurement apparatus outlined in Section 4.3.1, a velocity profile was measured in three locations: 15 mm behind the downstream rotor, at the diffuser exit face, and 305 mm (12 inches) behind the diffuser in the wake. The large inlet was attached for these tests, and data were collected with the upstream rotor.

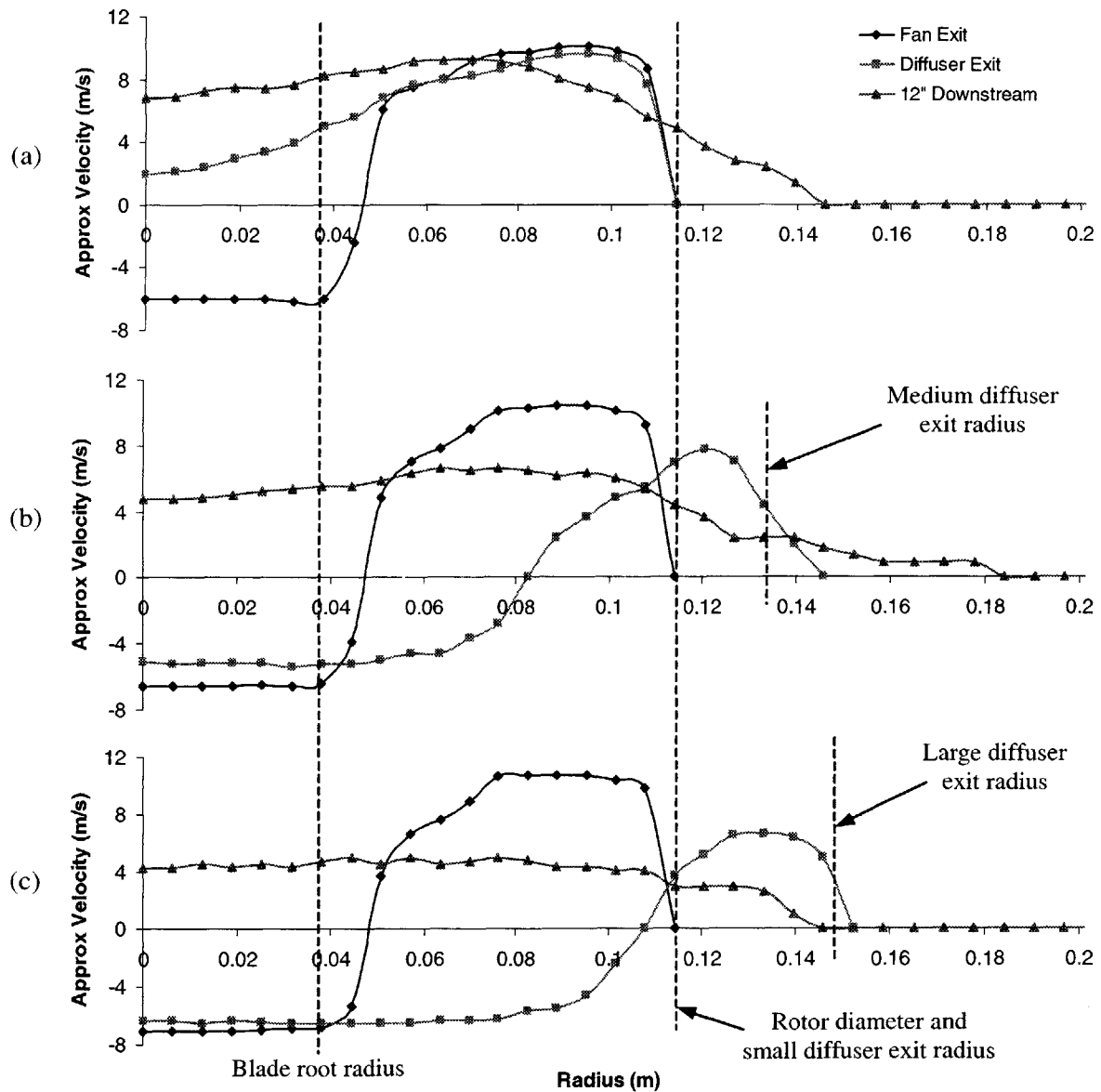


Figure 5.14 Wake flow for (a) small diffuser ($\sigma_{duct} = 1.0$), (b) medium diffuser ($\sigma_{duct} = 1.37$), and (c) large diffuser ($\sigma_{duct} = 1.65$) with single rotor at 3000 RPM.

Although the pitot probe could not be trusted to yield correct reverse velocity magnitudes, it is clear from the uncalibrated data that a strong reverse flow regime at the root exists. Yarn tuft tests confirm this. It appears that the wake flow tends toward the outer edge of the diffuser. Also unexpected is the very low velocity in the wake, especially for the large diffuser, where the far wake has contracted from the diffuser exit area.

Once wake results made it evident that a strong reverse flow region existed in the core of the duct, an 8-cm diameter, 25-cm long cone was placed behind the second (downstream) rotor. The result of this test with only a single rotor is compared to the results without the cone and two rotors in Figure 5.15.

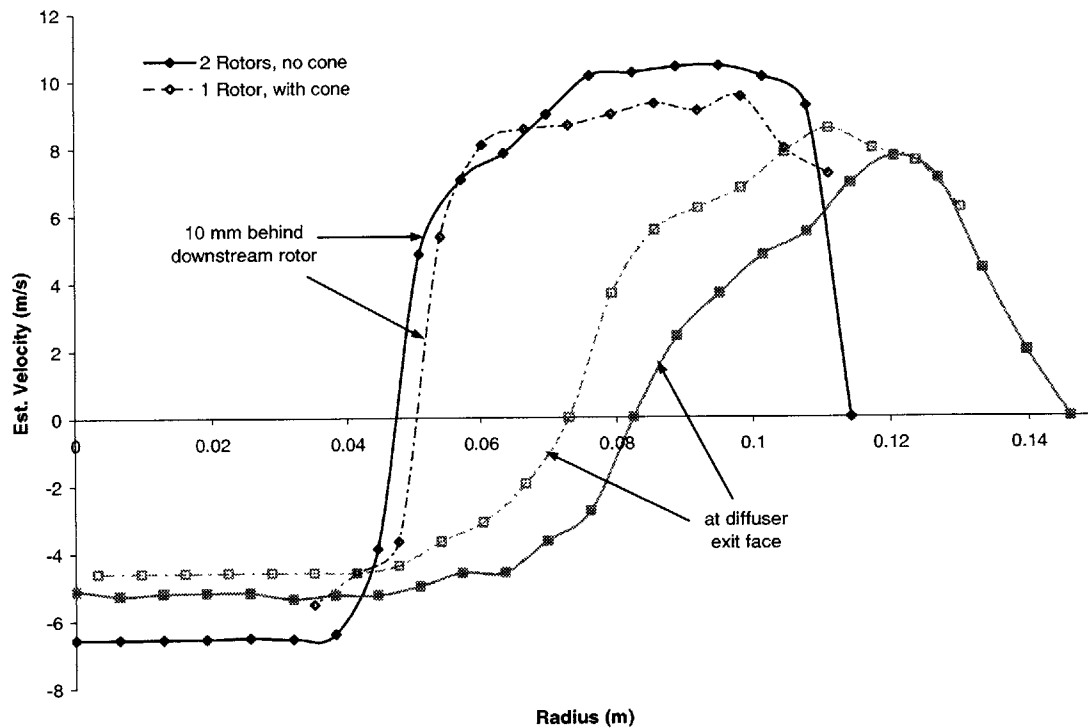


Figure 5.15 Wake survey comparison of single rotor with cone-shaped fairing and dual rotor without a fairing.

In the higher thrust case of two rotors, denoted by a solid line in Figure 5.15, the induced velocity profile is very similar to the single rotor test case with a cone fairing attached. The fairing appears to bring the reverse flow transition point (where the flow direction changes) outward slightly, and the single rotor provides slightly less induced velocity. The wake at the diffuser face for the dual rotor test case is concentrated at the periphery. As noted in Section 5.3.2, this is likely due to a high centrifugal flow that is stronger at higher thrust conditions when the induced velocity is high.

Thrust tests were also performed for the duct with and without a cone fairing over a range of speeds. The rotor collective was fixed at 35° , while the first (inflow) rotor was removed.

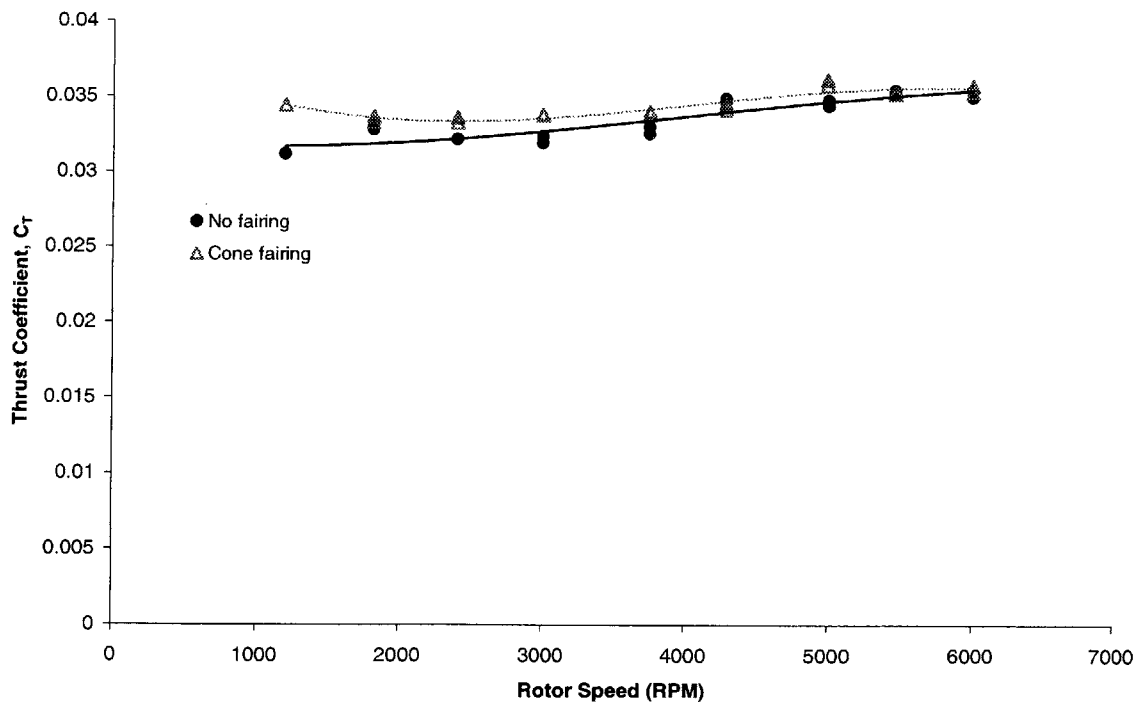


Figure 5.16 Thrust coefficient as a function of rotor RPM with and without a cone-shaped fairing (single rotor, 35° fixed).

The thrust coefficient is very slightly improved with the use of the fairing, especially at low speeds. This is probably due to restriction of the reverse flow, which hinders performance. Greatest thrust coefficient for both test conditions was attained at high RPM.

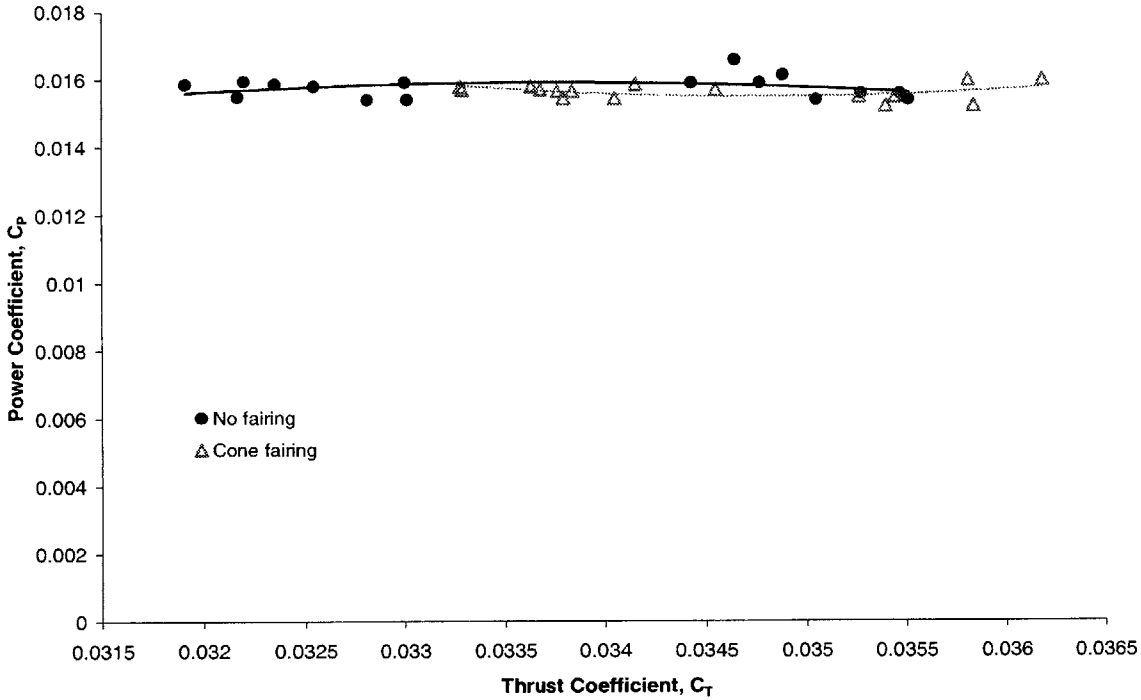


Figure 5.17 Power coefficient as a function of thrust coefficient with and without a cone-shaped fairing (single rotor, 35° fixed).

Power coefficient appears from Figure 5.17 to remain nearly constant over the speeds and thrust coefficients obtained in tests. The cone fairing again yields slightly better performance with a reduction in power compared to the unfaired case though performance is nearly identical in both configurations.

Swirl angle tests were also performed to determine the amount of wake swirl for a single rotor and a pair of contrarotating rotors. A yarn tuft was attached to the end of a metal

rod, which was then held 15 mm behind the downstream rotor at various radial positions. The angle of the tuft was then measured relative to a line drawn on the inner duct surface parallel to the duct axis. Measurements were taken at 20, 40, 60, 80 and 100 percent of the duct radius for two speeds each on the two rotor conditions. Measurements taken below 60 percent radius were disrupted by turbulent and sometimes reversed flow.

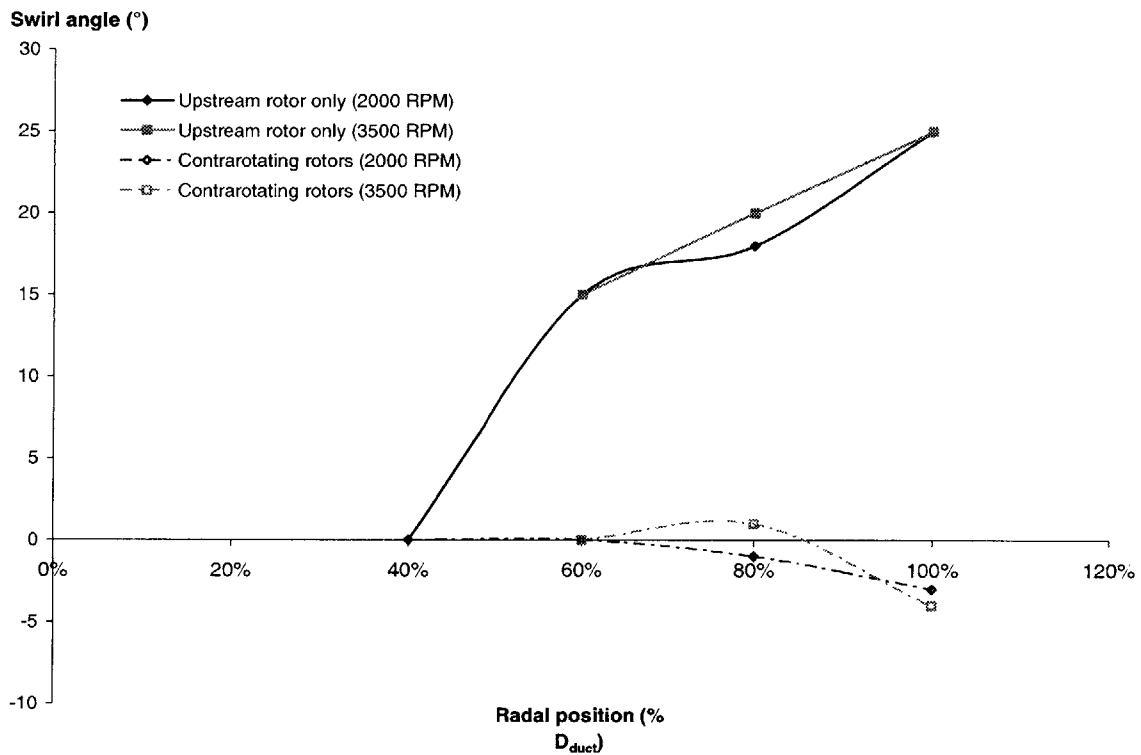


Figure 5.18 Swirl angle for single (upstream) and dual rotor condition.

For the dual contrarotating rotor case, the swirl angles were very small, as one would predict based on previous tests and numerical model predictions. This indicates that the second rotor absorbs most of the swirl of the first rotor and causes a very slight swirl in the opposite direction at the tip. The tuft position could not be measured at inner portions of the duct due to its erratic movement. The single rotor tests demonstrate that the blades produce large swirl angles, of up to 25 degrees at the tip. This swirl can be viewed as lost

energy, because it results in expended energy that does not lead to a thrust increase. The lack of swirl for the contrarotating configuration signifies that the induced swirl of the upstream rotor can be used to generate thrust.

5.4 Results Analysis and Model Comparison

In this section the results of experimental tests will be compared with the analytic and numerical models developed in Chapter 3. The effect of inlet curvature and exit diffuser area ratio will be discussed.

5.4.1 Inlet Size

All inlet tests were performed with a medium diffuser of diffuser exit ratio, $\sigma_{duct} = 1.37$. Four inlets were used, one with a ‘small’ 3.18 mm radius of curvature, one with a ‘large’ 25.4 mm radius of curvature, and two ‘medium’ inlets with a 12.7 mm inlet lip radius of curvature. The latter two are distinguished by the inclusion of a 25 mm flange attached to the periphery of one inlet, tangent to the surface to allow smooth airflow over the flange and curved inlet.

Tests were performed at a range of speeds, from 1200 RPM to 3600 RPM, and up to 6000 RPM in some cases. Due to the sheer volume of data, the following plots are presented for a single speed of 2400 RPM. The curves are indicative of the behavior for other speeds.

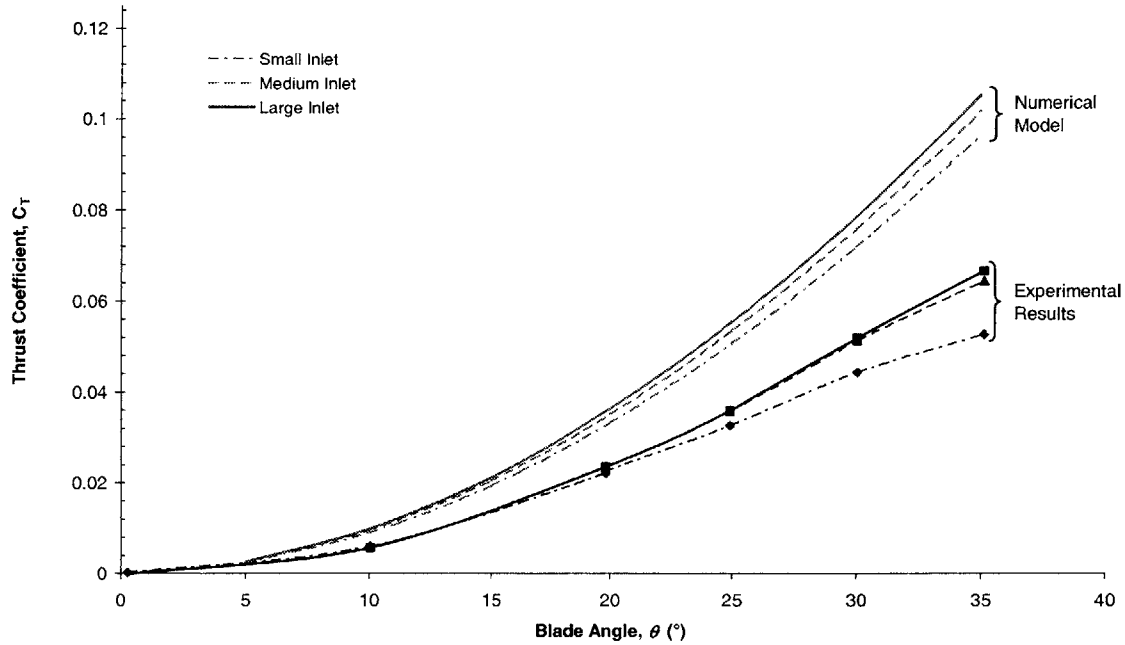


Figure 5.19 Thrust coefficient, C_T as a function of blade angle, θ for three inlet sizes (2400 RPM).

The numerical model does not account for inlet losses presented in Section 3.2.2, but does differentiate by size when calculating the inlet suction thrust. A larger radius of curvature presents a greater surface area, even if a flat flange area is not attached, as can be seen by the C_T spread of the numerical model output curves in Figure 5.19.

Experimental results appear to indicate that the larger radius of curvature of the 25.4-mm inlet provides a nearly insignificant performance benefit over the medium 12.7-mm inlet. The medium inlet shows a slight drop in thrust compared to the large inlet at higher blade angles, which may indicate the initiation of separation. Separation is likely the predominant cause of the drastic thrust loss for the small, 3.18-mm inlet, though suction lift is also limited due to the small surface area. The results at least serve to set a reasonable minimum inlet radius for unseparated thrust from the duct.

The wide spread between the experimental and model curves is due to diffuser effects that will be further covered in the next section.

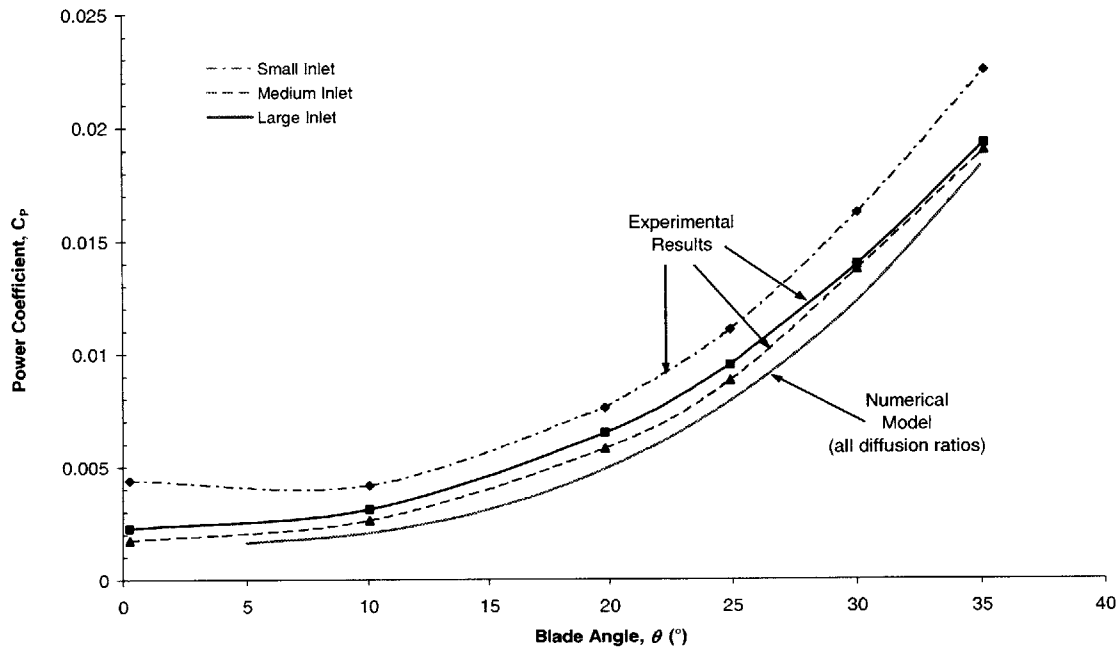


Figure 5.20 Power coefficient, C_p as a function of blade angle, θ for three inlet sizes (2400 RPM).

The numerical model shows an insignificant effect on performance with different inlet sizes. Vena contracta losses likely cause the high power for the small inlet. Experimental results show that the flow is separated over the sharp inlet, causing the rotors to experience disrupted inflow, requiring high power. The power required for the large inlet is slightly larger than for the medium inlet, perhaps indicating that the benefits of smoother flow transition have been offset by the overall increase in inlet drag area.

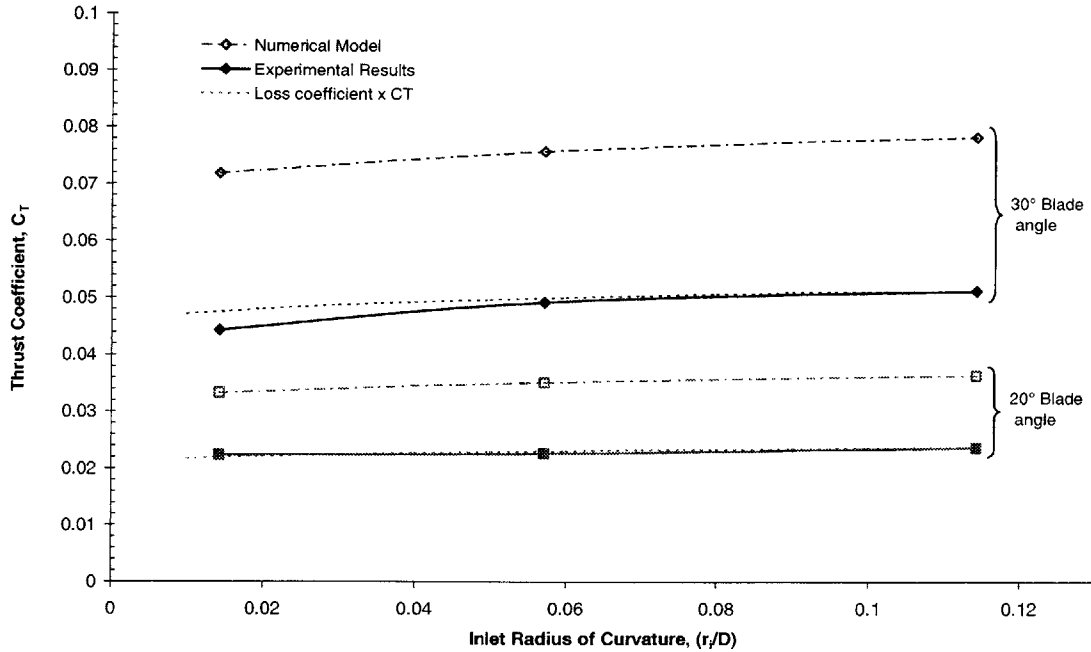


Figure 5.21 Thrust coefficient, C_T as a function of inlet size, r_i (2400 RPM).

Figure 5.21 illustrates the effect of lip radius of curvature on thrust coefficient. The numerical model label signifies the results of the Matlab model outlined in Section 3.3 and Figure 3.9, which does not account for inlet or diffuser losses. The change in thrust coefficient as a function of inlet radius is solely a function of the inlet suction thrust. Interestingly, the behavior of the numerical model plot as a function of inlet radius is very similar to the experimental results, although the model results are offset by a factor likely caused by incorrectly modeled diffuser effects.

The dotted curve presents the loss coefficient of Equation (3-92).

$$\frac{T_L}{T} = \frac{K_L}{4} \quad (3-92)$$

Because this loss is simply a percentage of the optimal curvature thrust coefficient, the loss model was normalized to the 25.4-mm experimental thrust coefficient point. Note

that the 20° blade pitch angle experimental data follow the numerical prediction nearly exactly, though the higher 30° experimental data do not agree exactly for the small inlet.

The best performance indicator is the ratio of power to thrust, as presented by a C_P/C_T vs. C_T curve. Because the experimental results for diffusion ratio are much less than what the numerical model predicts, the C_P/C_T curves for model and experimental results also show a wide spread. The behavior between them is still valid, as there appears to be no coupling between the diffusion ratio that causes this large variation, and the inlet-induced performance behavior.

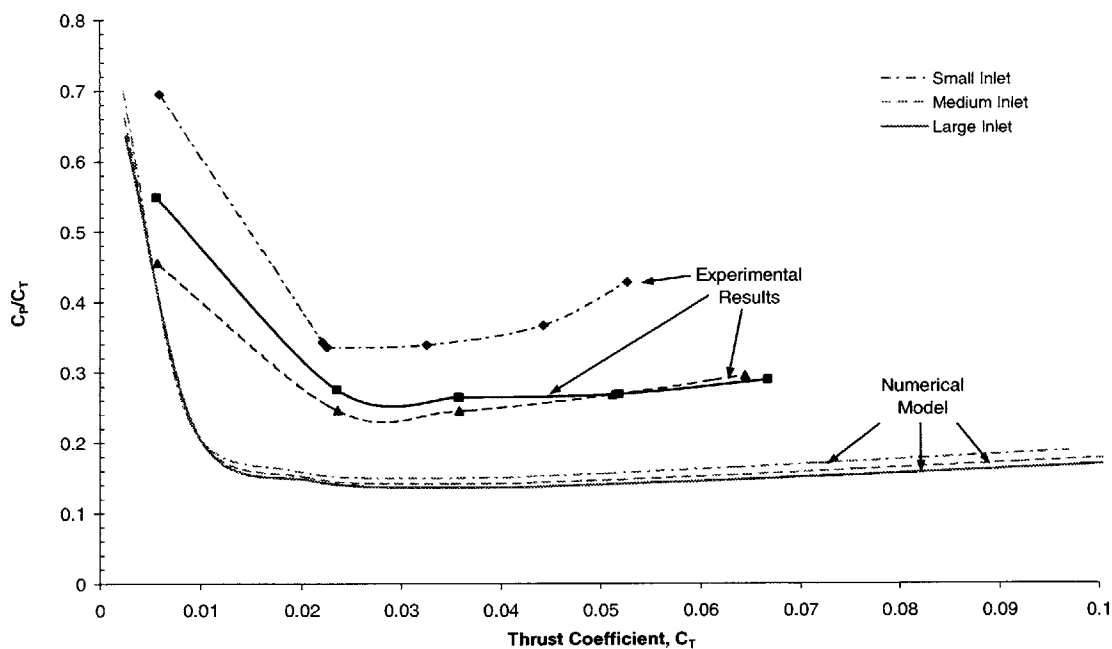


Figure 5.22 C_P/C_T as a function of thrust coefficient, C_T for three inlet sizes (2400 RPM).

Clearly, the small inlet provides the poorest performance, as indicated by a high C_P/C_T curve. The numerical model under predicts this, due to its lack of an inlet loss effects model. Interestingly, the slight power advantage of the medium inlet over the large inlet leads to a better efficiency overall. As mentioned previously, the smoother flow

transition is probably not significant enough to compensate for the slight increase in drag area. Optimal efficiency occurs at lower thrust coefficients, although significant benefits would only occur at very lightly loaded conditions. Thrust requirements and available power will dictate the importance of thrust or efficiency in the flight vehicle.

To validate the inlet suction thrust model derived in Section 3.2.1, a separate inlet test was performed to measure the thrust with and without a flange. The radius of curvature of both test articles was identical, with the surface area as the sole difference between the two test pieces. The tests were performed over a range of blade angles and speeds. The 1800-RPM point is shown as it represents the general behavior for other speeds.

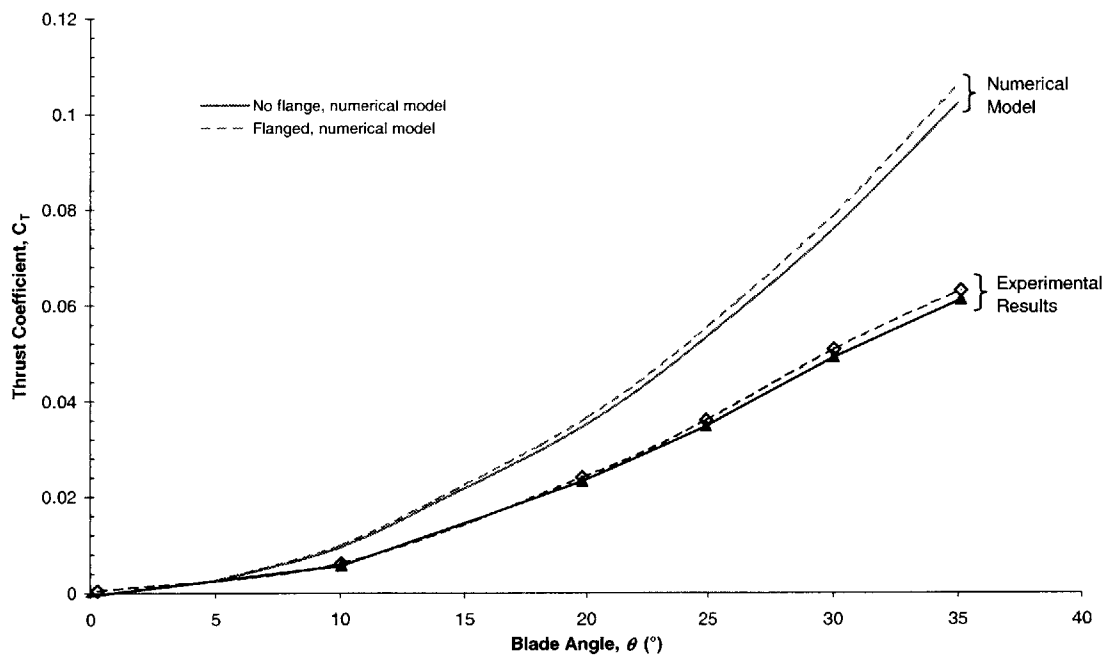


Figure 5.23 Thrust coefficient, C_T as a function of blade angle, θ for flanged and unflanged medium inlets (25 mm flange, 1800 RPM).

Although the numerical model again predicts a higher thrust coefficient than the experimental results, the difference between flanged and unflanged thrust coefficient is nearly identical to the experimental data obtained. The numerical model and

experimental results both show approximately 4 percent greater thrust coefficient with a 25-mm flange when a medium inlet radius of curvature is used at 1800 RPM.

5.4.2 Diffusion Ratio

All diffuser test data were taken with a large, 25.4-mm (1-inch) radius inlet. Three diffusers were tested. The small diffuser had a physical diffusion ratio, σ_{duct} of 1.0, indicating zero physical divergence. The medium diffuser comprised a 1.37 duct diffusion ratio while the large diffuser had a σ_{duct} of 1.65. As with the inlet test data, overall behavior was generally the same over different speeds, so data from the 2400-RPM tests will be presented.

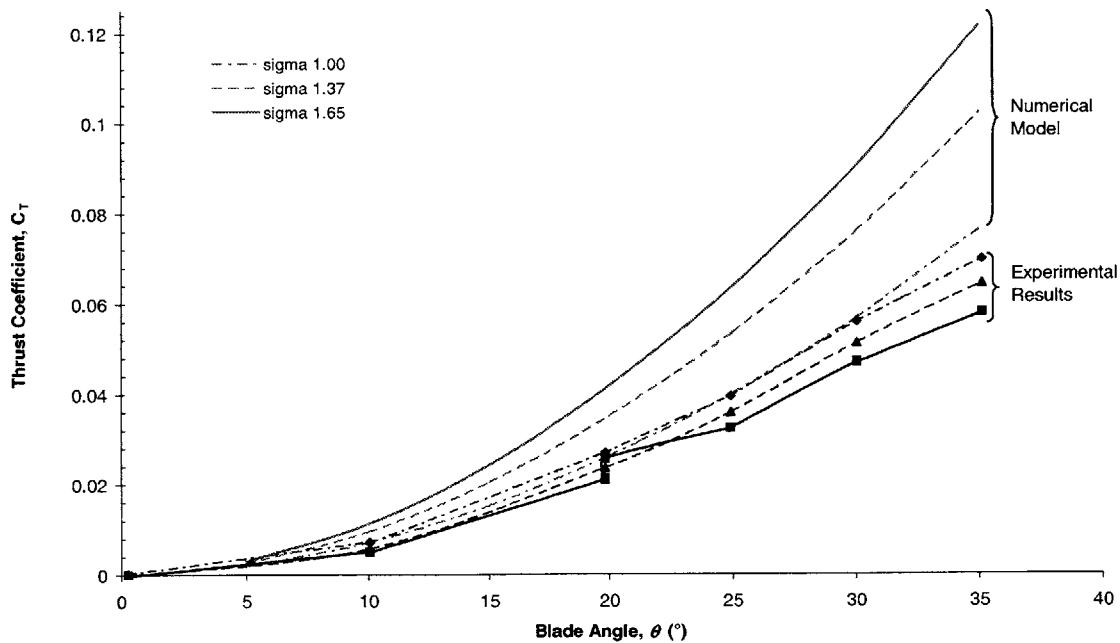


Figure 5.24 Thrust coefficient, C_T as a function of blade angle, θ for three diffuser ratios (2400 RPM).

The numerical model predicts that the thrust coefficient will rise as diffusion is increased, however experimental results show an opposite trend. For the constant diameter diffuser

with a diffusion ratio of 1.0, the model and experimental results agree well, except for the high blade angles where the portions of the blades are likely stalled. The medium diffuser should yield approximately 34 percent more thrust than the small, yet in testing the medium diffuser showed a 10-15 percent **reduction** in thrust. The trend for the large diffuser continues, with an expected thrust increase of nearly 60 percent over the small, non-divergent diffuser, yet test results indicating an approximate 20-percent **loss** in thrust. These surprising trends are best illustrated by a plot of thrust coefficient as a function of physical duct diffusion for two collective settings.

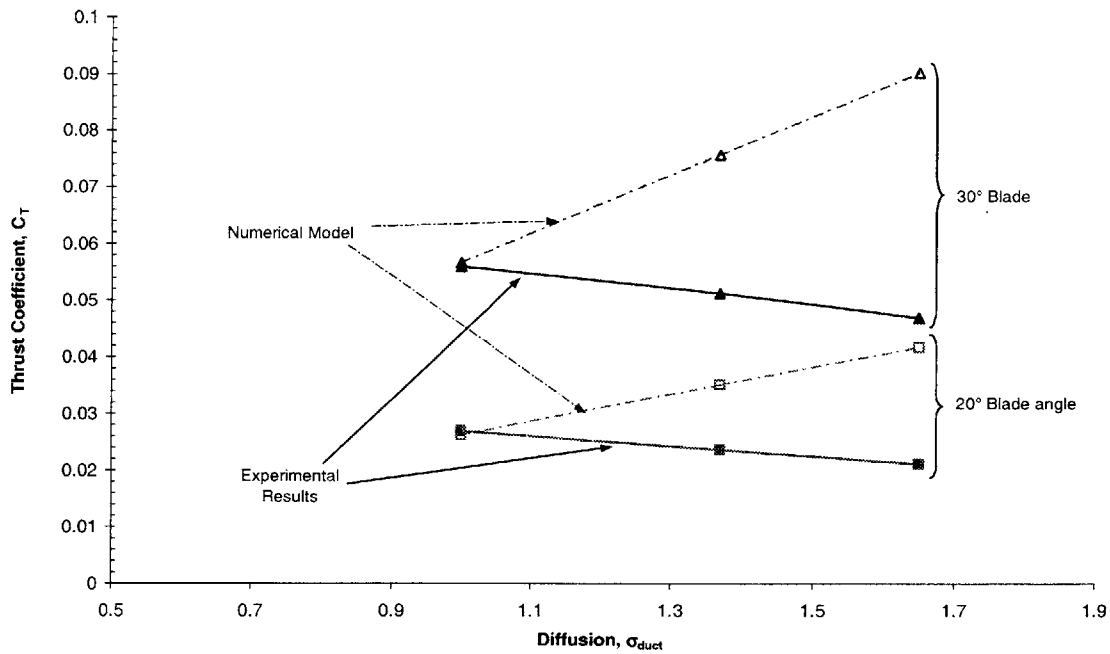


Figure 5.25 Thrust coefficient, C_T as a function of diffusion ratio (2400 RPM).

Note that at $\sigma_{duct} = 1.0$ the model and experimental results coincide, but as diffusion is increased the model and test results diverge, indicating that the physical mechanism for providing flow diffusion is not producing its intended effect on the induced wake.

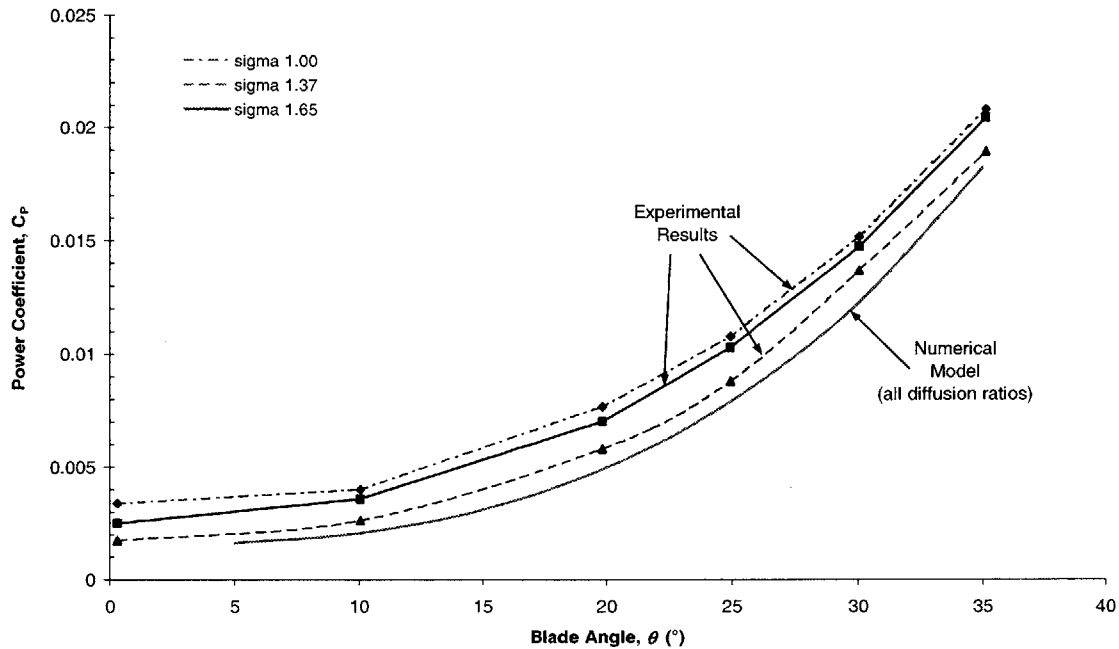


Figure 5.26 Power coefficient, C_P as a function of blade angle, θ for three diffuser ratios (2400 RPM).

The numerical model predicts a negligible change in power as diffusion ratio is increased. Figure 5.26 shows the power coefficient as a function of blade angle. Tested power coefficient is greatest for the small diffuser and smallest for the medium diffuser.

In theory, optimal performance should be obtained with a large diffuser. In reality the diffusion angle that one can obtain before separation and other losses occurs is much less than a simplistic model may predict. In Figure 5.26, the ratio of power coefficient to thrust coefficient, C_P/C_T is plotted as a function of thrust coefficient. Because losses are not considered the optimal performance is expected to be obtained with the large diffuser of diffusion ratio, $\sigma_{duct} = 1.65$.

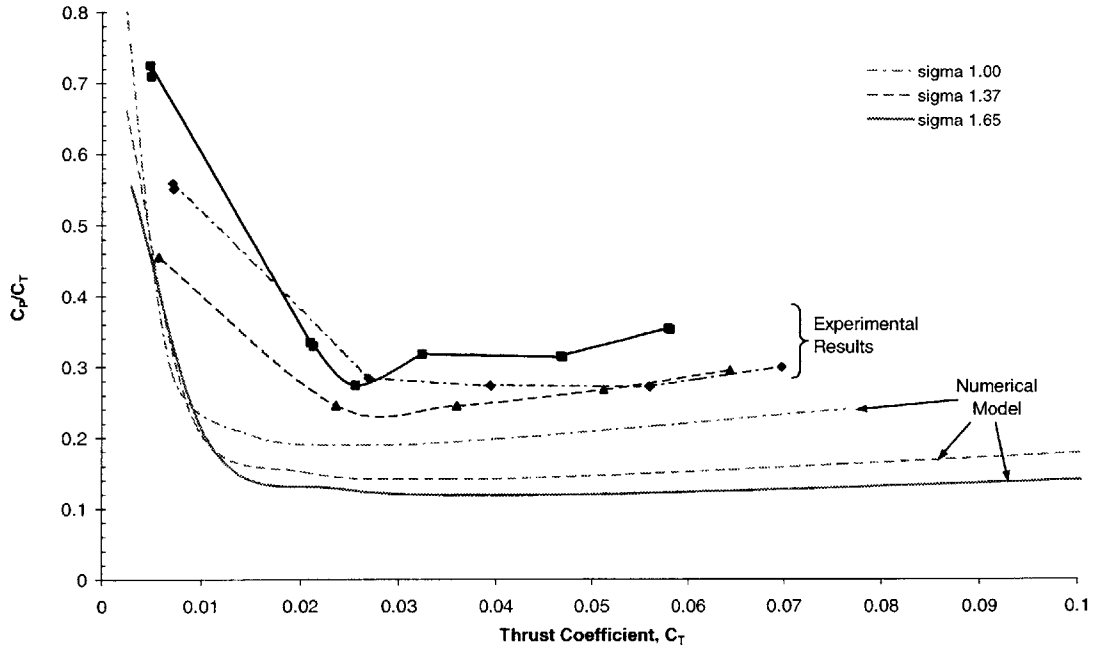


Figure 5.27 C_P/C_T as a function of thrust coefficient, C_T for three diffuser ratios (2400 RPM).

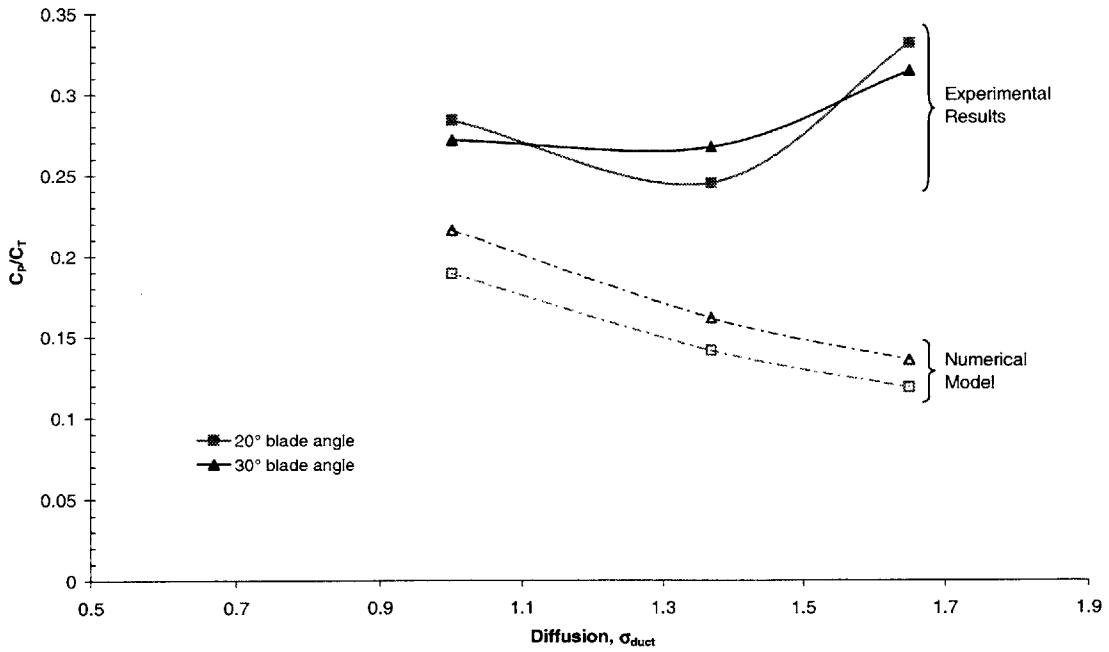


Figure 5.28 C_P/C_T as a function of diffusion ratio at 2400 RPM.

Experimental results depicted in Figure 5.28 show that when power and thrust are both considered, the efficiency of the large diffuser is worst. This plot is representative of the

general behavior, though some speed and blade angle combinations indicate maximum efficiency occurs with the small diffuser. Best efficiency is usually obtained at medium thrust coefficient with the medium diffuser fitted. Clearly, the actual test article does not follow the predicted performance. The reason for the inadequacy of the model to describe the performance of a divergent diffuser is mostly in the wake flow. The model is based on the assumption of smooth, uniaxial flow, with no reverse regions or viscous shear layers.

The wake survey plots graphically illustrate the experimental thrust and power results. Actual wake diffusion as shown by the wake surveys does not correspond to the physical diffusion of the duct exit diffusers. Ideally, the wake surveys should show a broad, uniform induced wake that increases in area as the diffusion is increased. The wake surveys of Section 5.3.6, however, show that the low-pressure, reverse flow inner core expands as the diffusion increases, and that the wake consists of a reverse flow region surrounded by a high velocity ring before dissipating into a narrow wake.

It is likely that the combination of reverse flow and non-ideal rotor blades effectively cancel the benefits of duct diffusion. Since the numerical model was developed assuming ideal flow, it is not surprising that it was unable to predict the performance of this very complex flow environment.

[THIS PAGE INTENTIONALLY LEFT BLANK]

Chapter 6: Conclusion

Experimental results of this study indicate an unexpected turbulent reverse flow region within the near wake, which induces a high velocity wake ring to form. The resulting wake flow is not well distributed and fails to diverge as expected into a broad low velocity, high pressure wake field. Thrust and power data confirm that this wake saps power and thrust, diminishing the expected beneficial diffuser effect.

Many useful results have been produced through this project, including a flexible test article with the ability to reconfigure the number and size of the rotor blades, the inlet size and geometry and exit diffuser geometry. The electric power supply is sufficient to drive a broad range of aerodynamic combinations, which will be useful in future ducted rotor research. The ability to accurately and efficiently collect thrust, speed and power data will also be invaluable.

The numerical model developed for the project, although unable to properly model the very complex aerodynamic behavior of the diffuser wake flow, has been validated as a reasonable method of prediction for all other aspects of the PUAUV. Future analysis and testing of the wake may allow the incorporation of analysis methods into the model to account for the convoluted airflow.

Future testing was to incorporate Vario 35.5 mm chord ($\sigma_{rotor} = 0.41$) tail rotor blades to experimentally evaluate the effect of solidity on performance. However, with a better understanding of the wake problems and using the results of findings presented herein, a redesign of the rotor blades to optimally twisted and cambered blades that account for low Reynolds number skin friction effects will be more useful. The incorporation of a center fairing should also help to mitigate some of the wake losses witnessed during testing.

Also considered for future work is the development of an improved drive train loss model that will account for load-dependent gear friction losses. An automated voltage and current measuring system would also expedite data collection, though it is not necessary.

The PUAUV program has been an educational venture. Much useful hardware and knowledge has been produced, opening the way for future ducted rotor propulsion and lift producing vehicle development within the Charles Stark Draper Laboratory.

References

- [1] Abbink, F. J., "Introduction to the KIVI Symposium on Unmanned Aerial Vehicles (UAVs)", June 7, 2001, [online presentation] URL: http://www.kivios.nl/dt/arch_uavintro.pdf [cited 20 May, 2002].
- [2] Anderson, J. D., Jr., "Fundamentals of Aerodynamics", New York: McGraw-Hill, Inc., 1991.
- [3] Black, D. M., Wainauski, H.S., and Rohrbach, C., "Shrouded Propellers – A Comprehensive Performance Study", AIAA 5th Annual Meeting and Technical Display, Philadelphia, PA, October 1968.
- [4] Gupta, N., "Design and Manufacturing of a VTOL Micro Aerial Vehicle", *Masters Degree Thesis in Mechanical Engineering, MIT*, Cambridge, MA, May 2001.
- [5] Hunter, K., "DARPA Says MAV Acquisition Schedule Driven By Technology", 25-Aug 1999, Inforwar online article URL: http://www.inforwar.com/mil_c4i/99/mil_c4i_082599d_j.shtml [cited 20 May, 2002].
- [6] Johnson, W., "Helicopter Theory", New York: Dover Publications, Inc., 1980.
- [7] Krüger, W., "On Wind Tunnel Tests and Computations Concerning the Problem of Shrouded Propellers", NACA TM 1202, 1949.
- [8] Kücheman, D., Weber, J., "Aerodynamics of Propulsion", New York: McGraw-Hill Book Company, Inc., 1953.
- [9] Lazareff, M., "Aerodynamics of Shrouded Propellers", *The Aerodynamics of V/STOL Aircraft*, Neuilly-Sur Sein, France: Advisory Group for Aerospace Research & Development, May, 1968.
- [10] Leishman, J., G., "Principles of Helicopter Aerodynamics", Cambridge: Cambridge University Press, 2000.
- [11] Lopez, R., "X-50 Dragonfly, Poised for Takeoff", *Aerospace America*, April 2002, pp. 30-34.

- [12] McKee, M. W., “VTOL UAVs Come of Age: US Navy Begins Development of VTUAV”, [American Helicopter Society web page], URL: <http://www.vtol.org/uavpaper/NavyUAV.htm> [cited 15 May, 2002].
- [13] Munson, B. R., et al., “Fundamentals of Fluid Mechanics”, New York: John Wiley & Sons, Inc., 1998.
- [14] Munson, K., “Jane’s Unmanned Aerial Vehicles and Targets, Issue Thirteen”, United Kingdom: Jane’s Information Group, 1999.
- [15] Office of the Secretary of Defense, “Unmanned Aerial Vehicles Roadmap, 2000-2025”, [online presentation] URL: http://www.acq.osd.mil/acqweb/usd/uav_roadmap.pdf [cited 20 May, 2002].
- [16] Stanford, S., Kornbluh, R., Low, T., DeLaurier, J, Loewen, D., Zdunich, P., “Flapping Wing Flight Using Artificial Muscles”, URL: <http://bees.jpl.nasa.gov/BEES2000/BEES-MAV.pdf> [cited 20 May, 2002].
- [17] Taylor, R. T., “Experimental Investigation of the Effects of Some Shroud Design Variables on the Static Thrust Characteristics of a Small-Scale Shrouded Propeller Submerged in a Wing”, NACA TN 3126, 1958.

Appendix A: Motor Specifications

Table A-1: Inertial Motors Specifications.

Ratings/Limits		Motor Constants		Dimensions	
Voltage (V_R/V_{max})	60/80 VDC	Torque constant (K_T)	14 oz·in/A	Diameter	3.00 in
Current (I_R/I_S)	5.7/15.8 A	Back EMF Constant (K_B)	10.3 V/ kRPM	Case length	8.55 in
Torque (T_R/T_S)	59/215 oz·in	Armature Resist. (R_A)	0.4 Ω	Shaft protrusion	2.40 in
Speed (S_R/S_{max})	5580/7730 RPM	Viscous Damp Torque (T_d)	2.7 oz·in/ kRPM	Shaft Diameter	0.4995 in
Max Cont. Dissipation	175 W	Static Friction Torque	6 oz·in	Weight	6.8 lbs
Note: Subscript R denotes rated parameter, S denotes stall limit parameter				Note: Shaft has (2) ground flats 1.60 in long, 90° apart	